MRI-COMPATIBLE PNEUMATIC ACTUATION CONTROL ALGORITHM EVALUATION AND TEST SYSTEM DEVELOPMENT

by

Yi Wang

A Thesis

Submitted to the Faculty

of the

WORCESTER POLYTECHNIC INSTITUTE

in partial fulfillment of the requirements for the

Degree of Master of Science

in

Mechanical Engineering

by

September 2010

APPROVED:

Prof. Gregory S. Fischer, Major Advisor

Prof. John M. Sullivan, Committee Member

Prof. James Van de Ven, Committee Member

Prof. Cosme Furlong-Vasquez, Graduate Committee Representative

Abstract

This thesis presents the development of a magnetic resonance imaging (MRI) compatible pneumatic actuation test system regulated by piezoelectric valve for image guided robotic intervention. After comparing pneumatic, hydraulic and piezoelectric MRI-compatible actuation technologies, I present a piezoelectric valve regulated pneumatic actuation system consisted of PC, custom servo board driver, piezoelectric valves, sensors and pneumatic cylinder. This system was proposed to investigate the control schemes of a modular actuator, which provides fully MRI-compatible actuation; the initial goal is to control our MRI-compatible prostate biopsy robot, but the controller and system architecture are suited to a wide range of image guided surgical application. I present the mathematical modeling of the pressure regulating valve with time delay and the pneumatic cylinder. Three different sliding mode control (SMC) schemes are proposed to compare the system performance. Simulation results are presented to validate the control algorithm. Practical tests with parameters determined from simulation show that the system performance attained the goal. A novel MRI-compatible locking device for the pneumatic actuator was developed to

provide safe lock function as the pneumatic actuator fully stopped.

Acknowledgments

I would like to express my gratitude to my advisor, Dr. Gregory Fischer, for all the guidance and support during my graduate study in Worcester Polytechnic Institute. In academic, he introduced me to the world of medical robotics and more importantly, enlightened me of numerous essential features that one should possess in order to dive deeper into the ocean of research. In study, he articulated the fundamental knowledge of robot kinematics and control in an intuitive way with abundant examples. In life, he has been a great person to train my listening and oral skills. As an international student, I would like to show my appreciation to him for opening this academic and culture door for me.

I am honored to have Dr. John Sullivan and Dr. James Van de Ven serving on my thesis committee as committee members and Dr. Cosme Furlong as committee representative. I am also grateful to Dr. Yiming Rong, who offered me invaluable advices when I felt confused. I am grateful to Dr. Christopher Sotak for teaching me fundamentals of MRI and allow me to use his facility for MRI-compatibility test.

Since I am the first student member of AIM lab, I felt that I was growing with

the advancement of AIM lab and AIM lab was like a prosperous family. I would like to thank all of the Automation and Interventional Medicine (AIM) laboratory members, especially Hao Su, Weijian Shang, Kevin Harrington, Gregory Cole and Yuanfang Gui. They offered me numerous help both in academic and in life. I would like to expressly thank Neil Whitehouse for teaching me to use lathe, drill and milling machine and offering advices in machining. I want to thank Barbara Furhman and Barbara Edilberti for their generous helps in administration.

I would like to thank Si Chen and Jun Yang for helping me select vehicle. I appreciate Siyuan Lv for offering tips about driving. I thank Peng Ni for his generous help when I first came here. I thank Chenguang Yang for offering me numerous help in life. I thank Haiyang Yang for helping me setting up phone and internet. I thank Dawei Zhang for giving me lifts before I owned a car, without whom my life could be a lot harder back then. I thank Shalin Ye for lending me his textbooks and helping me prepare exams. I thank Jian Zhao for offering me a ride during summer break. I thank Jing Zhang and Mengyun Wei for introducing a great city to me. And of course, I thank all my classmates back in China for supporting me, without whom I would probably not even be here.

Finally, I would like to express my greatest gratefulness to my parents. Their selfless love, which travels a distance of half the world, is exactly what have always been kept me moving forward.

Dedication

This thesis is dedicated to my grandparents and my parents, Jinguo Wang and Qingxia Wang.

Contents

List of Tables

List of Figures

Chapter 1

INTRODUCTION

1.1 Background on Image-guided Surgery

Image-guided surgeries are medical procedures in which medical images are provided by computer-based systems to assist the physician to precisely visualize and target the surgical area [1]. In 1908, Horsley and Clarke reported a frame with external markers which enabled them to assign a Cartesian space coordinate system to a monkey's head for neurological surgery [2]. The concept of the frame, later known as the Horsley-Clarke stereotactic frame, is still in use for neurological surgery, such as deep brain stimulation (DBS). The principles of image-guided surgery was mainly used for neurosurgery as the skull can provide rigid frame during most of the 20th century.

With the invention of CT, MRI and PC, this field has greatly expanded, such

Figure 1.1: The prototype robot in the bore of a 3T MRI scanner with the cannula targeting a model skull

as image-guided neurosurgery, orthopedics, cardiac interventions, thoracoabdominal interventions and prostate interventions. The implantation of deep brain stimulator has become increasingly popular for movement-disorder surgery [3]. Cole, Wang and Fischer [4–6] developed a robotic system for MRI-guided DBS electrode placement and tested MRI-compatibility of the system. Figure 1.1 shows the prototype robot in the bore of a 3T MRI scanner. Paul *et al* [7] developed a robot system for hip replacement guided by CT imaging. Rickers *et al* [8] employed real-time MRI to guide the placement of an atrial septal defect closure device. Xu *et al* proposed a robot system to assist lung biopsy using CT fluoroscopy images [9]. Fischer *et al* proposed a MRI-compatible robot system for transperineal prostate needle insertion using pneumatic actuation technique [10].

The typical work flow of image-guided surgery is shown as follows:

1. Acquiring pre-operative image (MRI, CT)
2. Tracking surgical device with a tracker (Z-frame, optical tracker)
3. Registering the patient anatomy to the pre-operative image and surgery device
4. Manipulating the tool to carry out the procedure with image guidance
5. Obtaining confirmation image when completed

Albeit numerous image-guided surgery system being developed for various surgical applications, most of them are still in the prototype stage, and a few clinical trials have been conducted so far. Safety and reliability are still of critical concern for image-guided system. Some of the image-guided surgery systems are shown in Fig. 1.2.

(a)

(b)

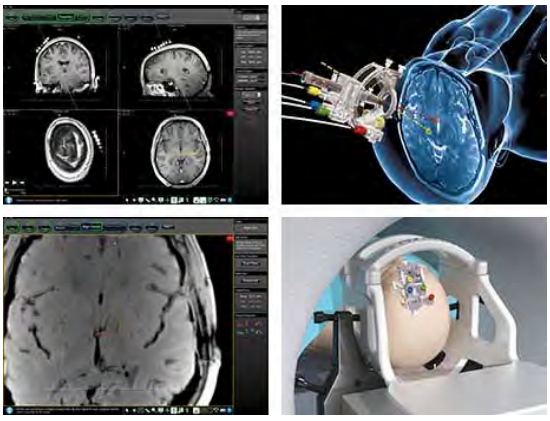

(c)

(d)

Figure 1.2: Examples of commercial available image-guided surgical systems: Radionics OmniSight™ EXcel, Medtronic LandmarX™ Element, SurgiVision ClearPoint™ and GE Instatrak™

1.2 Background on MRI-compatible Interventional Systems

MRI is an imaging modality that provides high resolution image of human tissue. Furthermore it offers excellent soft tissue contrast with capability to adjust the contrast to highlight certain type of tissue. Therefore it possesses a unique potential for monitoring therapy [11].

Such features of MRI addressed above provide a strong boost to image-guided surgery. Recent years have witnessed the flourishing of MRI-compatible robotics and its application in image-guided interventions and surgery. Elhawary *et al* [12] and Yu *et al* [13] presented reviews of the state of the art of MRI-compatible robotics.

A manipulator was firstly developed for needle insertion for MRI-guided neurosurgery by Musamune *et al* [14]. Briggs *et al* [15] proposed a MRI-compatible device for vision substitution by tactile stimulation. A MRI-compatible robotic system aiding minimal invasive surgery was developed by Chinzei *et al* [16]. Larson *et al* [17] introduced a MRI-compatible robot for biopsy and therapeutic interventions in the breast with real-time MRI guidance. A MRI-compatible 1 degree of freedom (DOF) smart hand interfaced rehabilitation device was developed by Khanicheh *et al* [18]. A 3 DOF MRI-compatible manipulator was presented by Tsekos *et al* to perform minimally invasive diagnostic and therapeutic abdominal interventions [19]. Fischer *et al* presented a MRI-compatible robot for prostate biopsy and brachyther-

apy with pneumatic actuators [20]. Due to the importance of force sensing in robotic applications [23], Su *et al* developed fiber optic sensors [21] for teleoperation in MRI [22, 24, 25]. Later, Su *et al* proposed a integrated MRI-compatible needle placement robot with fiber optic force sensing for prostate intervention [26]. Some of the MRI-compatible robotic systems are shown in Fig. 1.3.

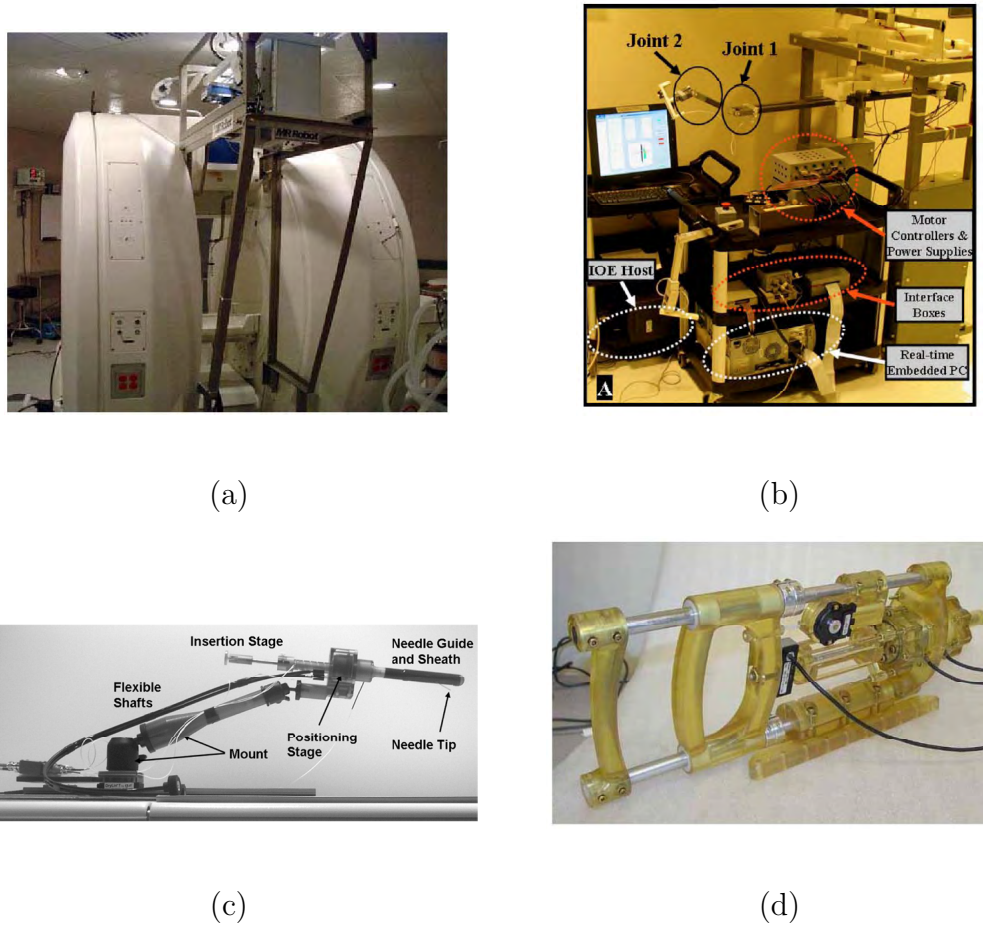

(a) (b)

(c) (d)

Figure 1.3: Examples of MRI-compatible robotic systems: Chinzei *et al* [16] in (a), Tsekos *et al* [19] in (b), Krieger *et al* [27] in (c), and Khanicheh *et al* [18] in (d)

1.3 Background on MRI-compatible Actuation Techniques

MRI provides high quality image for image-guided surgery. However, the high-field magnetic field limits the availability of technologies for interventions. There are a number of alternative actuation paradigms that are compatible with MRI environments ranging from the traditional methods including pneumatic actuation [28], hydraulic actuation [29] and ultrasonic piezoelectric actuation [30, 31] to non-conventional actuation including electro-rheological fluids (ERF) [32] and electro-strictive polymer [33].

Ultrasonic piezoelectric motor are now the most prevalent actuator choice by far for its good dynamic performance, ease of control, compact shape and low noise if properly shielded. Fischer [34] presented a comparison among two "off-the-self" piezoelectric motor, Shinsei motor and Nanomotion motor, and one customary pneumatic actuator. It is reported that the SNR loss is at 20% when moving in the scanner during imaging for Nanomotion motor.

In preliminary study for this thesis, Wang *et al* present the development of techniques to optimize the MRI-compatibility of the PiezoMotor actuator and controller such that the effects on image quality are negligible while maintain full functionality in [35]. The reported SNR loss is 3%, which is insignificant for most practical interventional applications. The configuration of the piezomotor test system is shown in

Fig. 1.4. Later on Wang *et al* presented some further work of developing an MRI compatible surgical robotic system, specifically targeting the neural intervention procedure for the treatment of Parkinsons Syndrome known as deep brain stimulation, or DBS in [5]. Specifically, the construction and testing of the MRI-compatible control computer and actuators, and the compatibility testing to validate the success of eliminating signal interference are demonstrated. The robotic system was tested on a Phillips Achieva 3Tesla MRI machine under T1, T2, fGRE and EPI imaging protocols, and has shown to be able to operate without producing any interference with scanner image quality that can be measured with statistical significance. The test configuration is shown in Fig. 1.5. As can be seen in Fig. 1.6, the motors and encoders provide almost no interference with the operation of the scanner, even while under full motion. The SNR for each of these imaging modalities under the Phillips 3T scanner is shown in Fig. 1.7. The boxplots show the variation in SNR for the 10 images taken in each configuration.

Despite of the merits mentioned above, the underlying friction driven working principle presents challenge in design and application for force feedback due to non-linearities, non-backdrivability and high wear. The high braking torque can be either an advantage or a detriment, with respect to a specific application [36]. Some of the MRI-compatible actuators are shown in Fig. 1.8.

Figure 1.4: The configuration of piezomotor test system

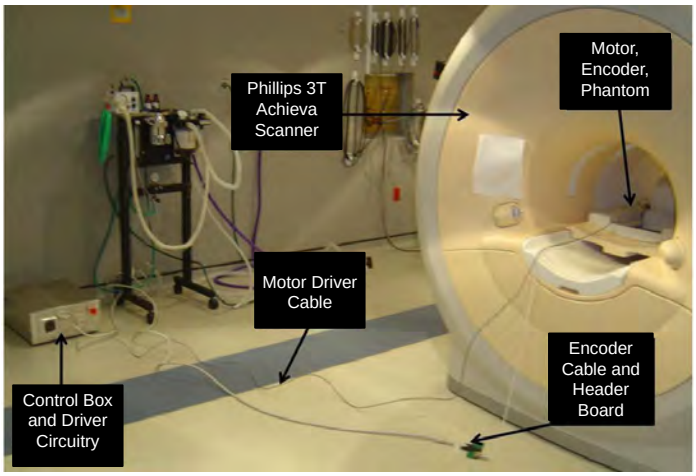

Figure 1.5: Configuration of the robot controller with sensors and actuators active in the scanner during tests

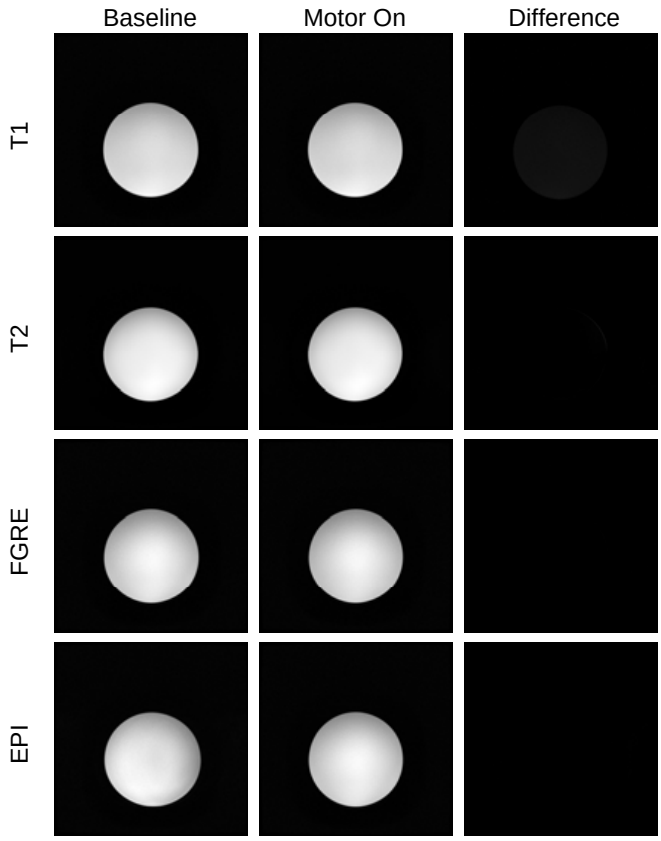

Figure 1.6: Representative results showing the difference of baseline and motor running conditions

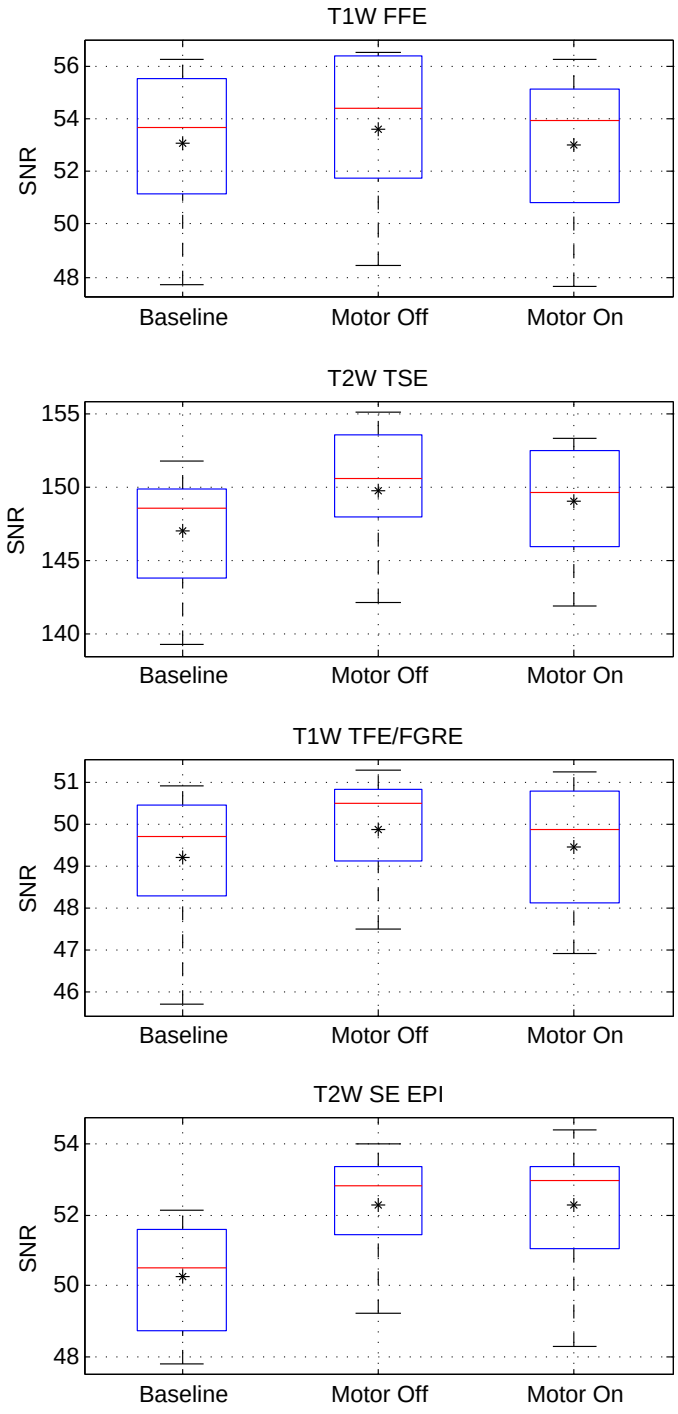

Figure 1.7: Results of MRI-compatibility analysis showing the SNR calculated

(a)

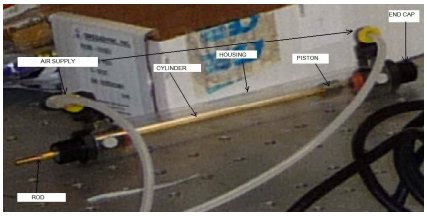

(b)

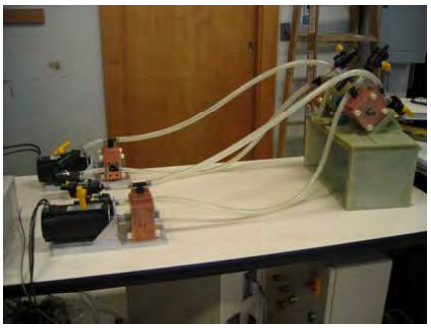

(c)

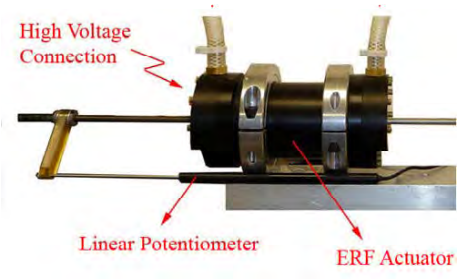

(d)

Figure 1.8: Examples of MRI-compatible actuators: (a) PiezoMotor PiezoLEGS^{TM}, (b) pneumatic cylinder [10], (c) hydraulic actuator [37] and (d) ERF actuator

1.4 Literature Review

1.4.1 Overview

Pneumatic actuation is a promising technique for MRI-guided interventions. The merit lies in solving the intrinsic compatibility issue by taking advantage of entire nonmagnetic parts and dielectric materials. Pneumatic actuator offers a low-cost alternative to piezoelectric actuating technology. And pneumatics is a preferred actuation method over hydraulics with regard to its cleanliness, ease of connectivity and ability to be operated at higher speeds.

Recently, Stoianovici *et al* [38] presented a new type of pneumatic motor encoded by optical sensors. Fischer *et al* proposed a MRI-compatible pneumatic robot for prostate intervention [20] and presented a comparative study which clearly indicated the advantage of pneumatic actuation under MRI environment [34]. Melzer *et al* presented a MRI-compatible robotic assistance system with 6 DOF, 5 of which are actuated by pneumatic cylinder [39]. Some of the MRI-compatible pneumatic actuators are shown in Fig. 1.9.

(a)

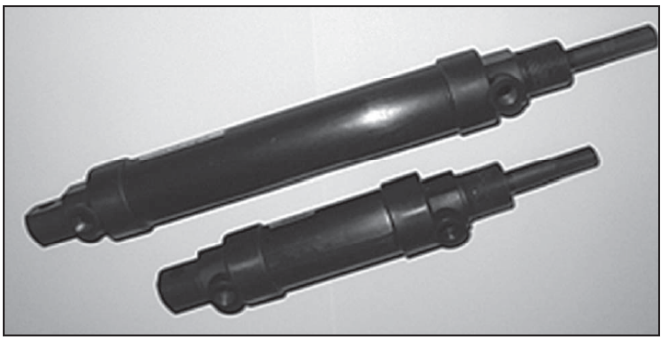

(b)

Figure 1.9: Examples of MRI-compatible pneumatic actuators: Stoianovici *et al* [38] in (a) and Melzer *et al* [39] in (b)

1.4.2 Pneumatic Actuator Control Techniques

According to the ideal gas law $pV = nRT$, the control input of pneumatic actuator, pressure p, is affected by V, which is referred as the compressibility of the gas, as well as the temperature T of the gas. Due to these factors, pneumatics possesses significant nonlinearity, which prevents linear control methods, such as PID, from providing accurate control of the pneumatic actuator. Several means have been developed for improving pneumatic cylinder control.

Two papers apply adaptive controllers to pneumatic applications. Bobrow and Jabbari use adaptive control for force and position control of a pneumatic axis [40]. McDonnell and Bobrow develop an adaptive controller for a pneumatic cylinder controlling the elbow joint of a robot [41].

Fuzzy control of pneumatics has not been broadly studied. Shih and Ma [42] use fuzzy control for position control of a pneumatic cylinder. A fuzzy controller and a neuro-fuzzy controller are two of six control schemes evaluated on a pneumatic axis [43].

Sliding mode control (SMC) has also gained the attention of researchers. Paul selects SMC for control of a pneumatic axis in [44]. Pu and Weston present a hybrid point-to-point controller for pneumatic actuators [45]. Messina and Giannoccaro use pulse width modulation (PWM) technique to control on-off valve of pneumatic cylinder [46]. Some of the position response of the pneumatic control algorithms are shown in Fig. 1.10.

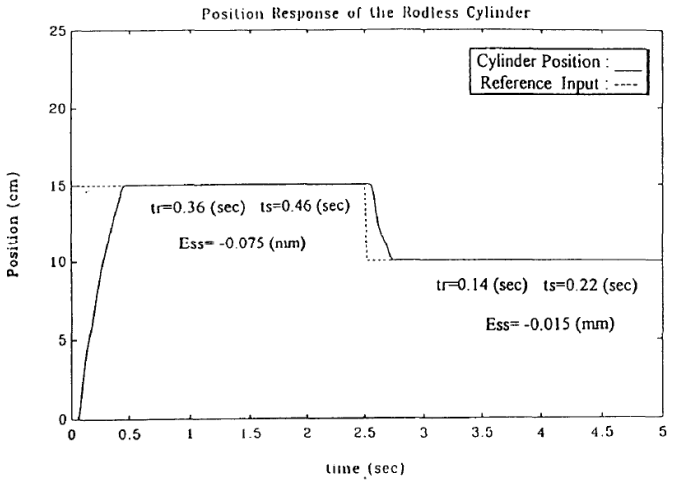

(a)

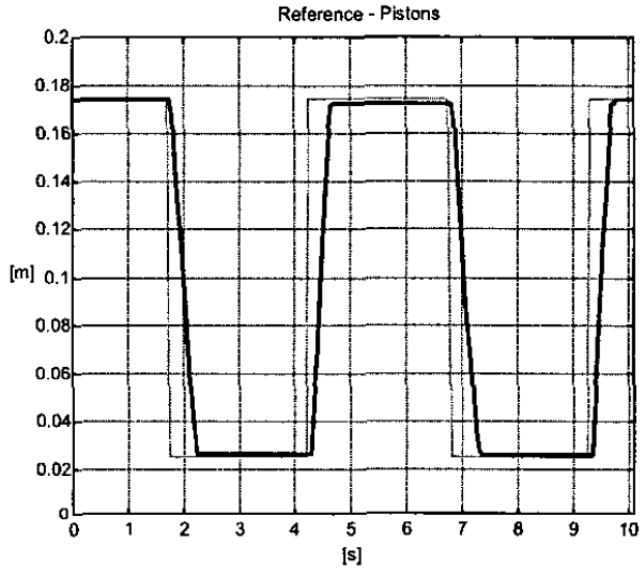

(b)

Figure 1.10: Examples of the position response of the pneumatic control algorithms: Shih *et al* [42] in (a) and Chillari *et al* [43] in (b)

1.4.3 Sliding Mode Control

The nonlinearity of pneumatics system presents significant challenges to accurate servo control. Also the difficulties in precise modeling and the uncertainties of various surgical applications call for robustness of control methodologies. Sliding mode control is an ideal option to meet these challenges. Sliding mode control is a nonlinear control method that drives the system state to a pre-defined sliding surface with switching control function.

Paul *et al* proposed a reduced order sliding mode controller (SMCr) for pneumatic actuators [47]. They used on-off solenoid valves and neglected stiction in the plant model. Acarman *et al* presented a SMCr with an observer for estimating position and chamber pressures [48]. A SMCr was presented by Korondi *et al* that switched between two modes, namely a steep sliding line that enables the states to approach the sliding surface rapidly, and a shallow sliding line as the trajectory approaches in the vicinity of the origin that ensures precise positioning [49]. Koshkouei *et al* proposed a higher order dynamic SMCr with improved system stability [50]. Nguyen *et al* mentioned a SMCr based on pulse width modulation (PWM) with low-cost solenoid valves. But the response has relatively large overshoot and the time response is not satisfactory [51]. Ning and Bone showed a thorough comparison of pneumatic system control techniques and development of SMC algorithms [52, 53] with a steady state error (SSE) of 0.01 mm.

Recently [54] proposed a global SMC scheme on a piezo-driven stage to compen-

sate for the unmodeled hysteresis. Gulati *et al* [55] presented the effectiveness of a Lyapunov-based pressure observer for pneumatically actuated systems.

Dead time is often seen in pneumatic valve. Camacho *et al* proposed a first-order-plus-dead-time (FOPDT) model with first order Taylor series expansion of exponential function to simulate the system in [56]. Some of the position response of the SMC algorithms are shown in Fig. 1.11.

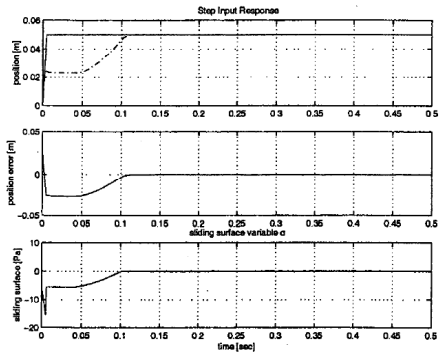

(a)

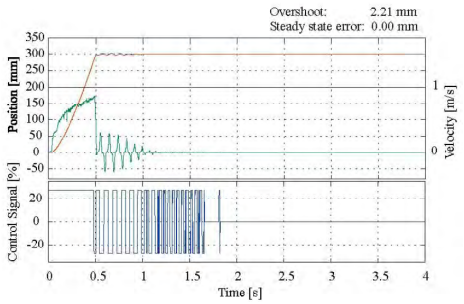

(b)

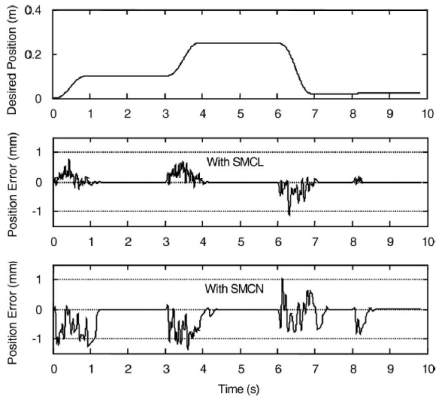

(c)

Figure 1.11: Examples of the position response of the SMC algorithms: Acarman *et al* [42] in (a), Korondi *et al* [49] in (b) and Bone *et al* [53] in (c)

1.5 Thesis Contributions

The purpose of this work is to present a pneumatic actuation test system to develop the controllers and systematically test the controllability and robustness of the MRI-compatible pneumatic actuator. Some of the papers presented in the literature review have came up with pneumatic test fixtures. However, to date, there is no system readily available to test under the conditions present and with the actuators available for MRI. The system consisted of novel piezoelectric pressure regulating valves, a custom programmable servo board driver, a voltage to current converter, two current-controlled piezoelectric pressure regulating valves, a MRI-compatible pneumatic cylinder and a MRI-compatible pneumatic lock. Three sliding mode control schemes were proposed to address the system nonlinearity with particular focus on time delay issue.

The key contribution of this work is the development of a pneumatic actuation test system which is capable of applying multiple type of load and recording sensor data and modeling of the system consisting of piezoelectric pressure regulating valves leading to a different system model which is simpler than many other systems in literature. Also this work present the development of a MRI-compatible pneumatic lock with simple, compact design to ensure safety after the actuator attained desired position which brings no additional friction to the pneumatic cylinder during the course of operation of the cylinder. This work demonstrates the simulation of tracking performance using three SMC schemes and robustness test based on the system model

with identified parameters. Furthermore, practical tests are performed with various loading conditions to compare with the simulation results.

1.6 Thesis Organization

The remainder of the thesis is organized as follows:

Chapter 2 provides the development of the pneumatic actuation test system. The goal of the system is introduced at first. Then the system architecture is presented with detail information on the mechanical and controller design, pneumatic cylinder, load components and air supply.

Chapter 3 presents the modeling of the pneumatic actuation test system. Background on some of the previous mathematic models are demonstrated. The complexity of the previous models is mainly induced by the indirect access to pressure of the cylinder chambers. Then a simpler model is introduced for the pneumatic actuation test system with the utilization of the piezoelectric pressure regulated valves. The modeling of the valves is presented with consideration of dead time.

Chapter 4 introduces the mathematical description of the three SMC control schemes. The tuning parameters of the three control schemes are presented as well. Also the Matlab simulation results of the three SMC control schemes employed on the pneumatic actuation test system are represented. Two types of tracking functions, step function and sine wave function, are proposed for evaluation. The results are compared in several aspects, such as tracking position accuracy, response time and so on. Various loading condition is applied to compare the robustness of each schemes.

Chapter 5 demonstrates the physical test of the pneumatic cylinder with identical parameters as presented in Matlab simulations. Comparision of the test results are

presented. The reason of the difference is discussed and possible explanation is proposed. The effect of each control parameter is discussed and a conclusion of control algorithm evaluation is presented.

Chapter 6 presents the development of the MRI-compatible pneumatic cylinder lock. The mechanical design and material selection is presented . Elementary test shows that the lock attains the design goal.

Chapter 7 summarizes the contribution of the work, and comes to a conclusion with suggestion of future work.

Chapter 2

DEVELOPMENT OF PNEUMATIC ACTUATION TEST SYSTEM

2.1 Motivation and Goals

Since the MRI-compatible pneumatic cylinder developed by Fischer [10] are designed to be utilized in multiple procedures, comprehensive tests are to be performed on the pneumatic cylinder to determine its controllability and robustness. To date, there has been no test system designated to fulfil such need. Hence the motivation of the pneumatic actuation test system is to provide a platform of performing test on MRI-compatible pneumatic cylinder with various load configurations as well as

control schemes.

The system should be designed such that algorithms on the control circuit can control the pneumatic cylinder position via pressure regulating valves and control schemes can be altered for comparison. Furthermore, sensors should be recording position, pressure of the pneumatic cylinder chambers and output force and transmit the sensor data to a computer for storage and analysis. The load of the pneumatic cylinder should include various weights, damper with adjustable damping ratio and constant force spring serving as gravity simulator.

2.2 Pneumatic Actuation Test System Architecture

Figure 2.1 shows the schematic diagram of the pneumatic actuator that would be integrated for robotic MRI-guided interventions. Navigation software running on a PC in the console room communicates with an embedded Linux PC and the control servo board in a shielded enclosure in the scanner room via a fiber optic cable runs through the patch panel.

The servo board sets control voltage of the valve based on position data as well as pressure data. The control electronics have been specially designed to operate in the scanner room without affecting MR image quality as demonstrated in [20,34], so as to limit the length of the pneumatic transmission lines which would bring considerable delay to system performance.

The schematic of pneumatic actuation test system is shown in Fig. 2.2. The system consists of a PC, a control servo board, a voltage to current convert board, two piezoelectric pressure regulating valves (Hoerbiger, model PRE-I), two pressure sensors (Omega, model PX309-100G5V), a force sensor (Futek, model LSB200), a transmissive optical encoder (US digital, model EM1-0-500), a MRI-compatible pneumatic cylinder and a linear guide (Igus, model Drylin T). The system configuration is shown in Fig. 2.3.

The PC, which is not shown in Fig. 2.3, sends tracking function commands to the

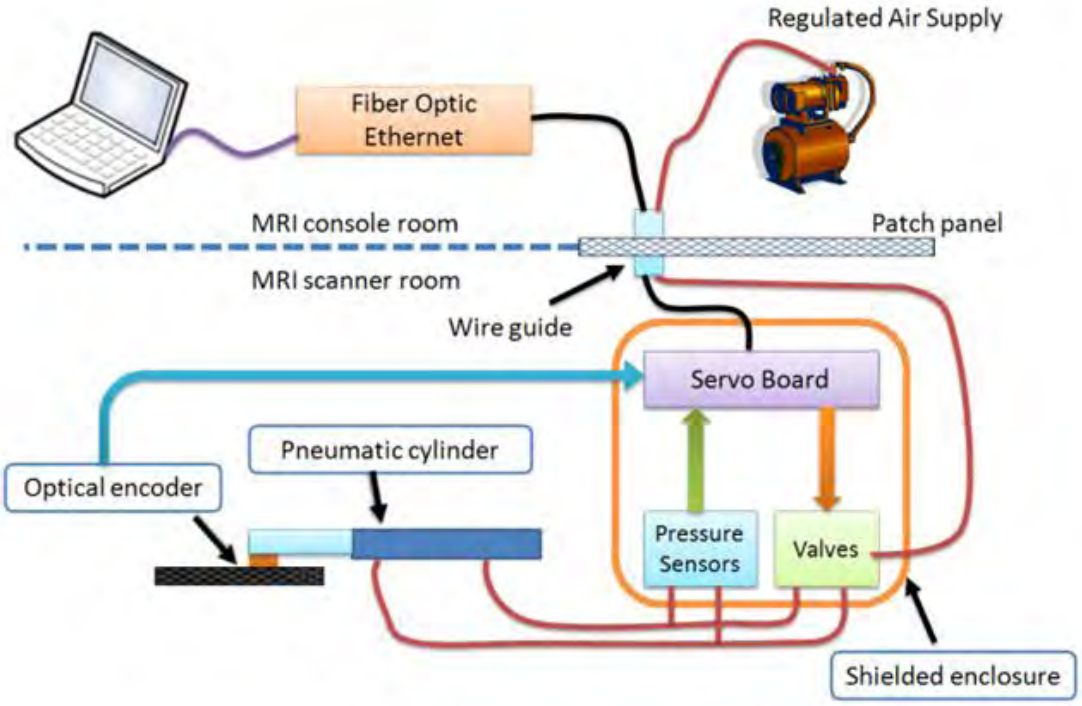

Figure 2.1: The schematic of the system for MRI guided intervention

control servo board. The control loop running in the servo board computes the control signal with respect to the tracking function and the servo board outputs the control signal ranging from 0-10V. The highly linear voltage to current board converts the voltage signal to the corresponding current signal ranging from 0-20 mA. The control current drives the piezoelectric valve, regulating the output air to the corresponding pressure. The pressure difference of the two cylinder chambers actuates the brass rod, driving the connected carriage to move along the rail. The optical encoder attached to the carriage records the position data and sends them to the control

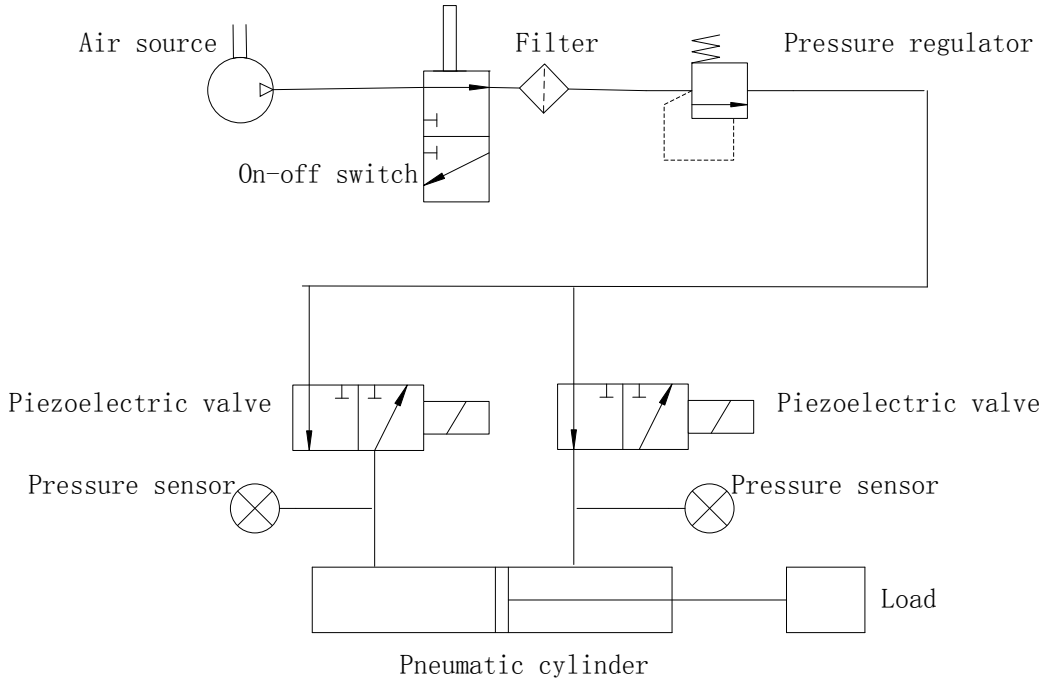

Figure 2.2: The schematic of the pneumatic actuation test system

servo board. Pressure sensors record the pressure data near the chamber inlets and send them to control servo board. Placing between the rod and the carriage, load cell records actuation force and send them to control servo board. The control loop in servo board updates the control signal according to the sensor data and the tracking function. Data packages consisting of position, pressure and force can be sent to the PC in synchronous or asynchronous mode.

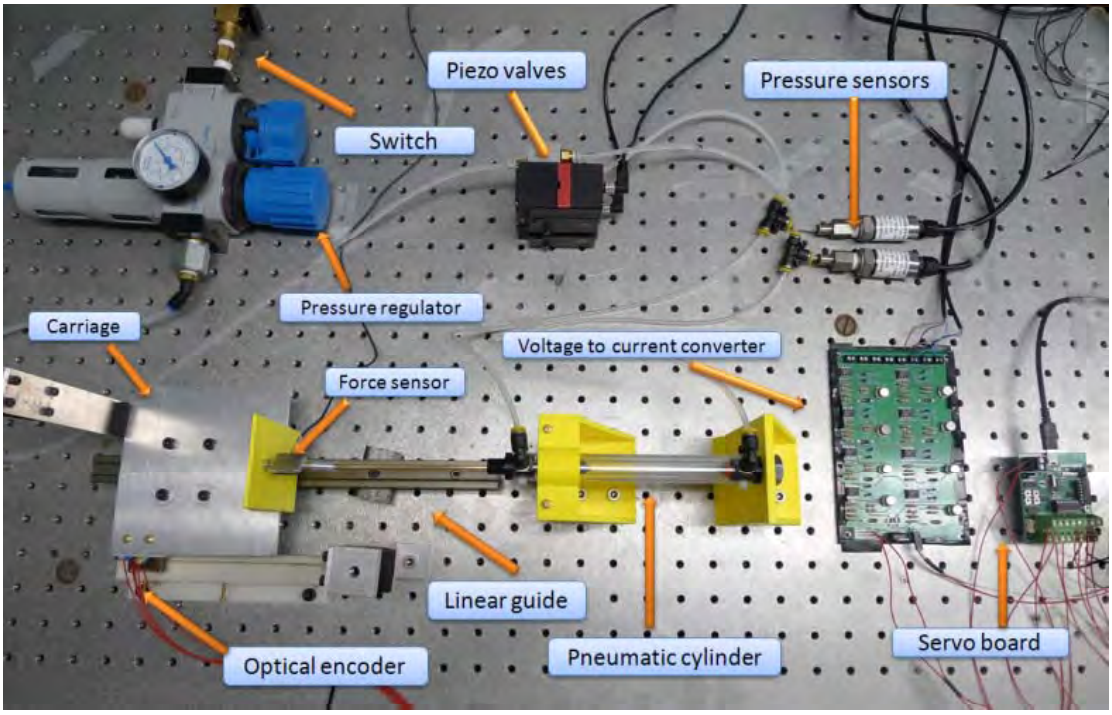

Figure 2.3: The configuration of the pneumatic actuation test system

2.3 Mechanical Design

2.3.1 Mechanism Design

The pneumatic actuation test system is a 1 DOF actuation system, mounted on the optical breadboard. For the purpose of conducting control test, several main design issues should be taken into consideration. In order to achieve high tracking accuracy, friction induced by misalignment should be reduced to the minimum. The mechanism should be designed such that the three types of load components can be easily installed and uninstalled, while reducing the bending effect that increases friction. The mechanism should be kept simple while satisfying the requirements above.

Additionally, a few extra design requirements adopted are:

1. System rigidity should be increased such that shaking and bending effect induced by the back and forth movements can be minimized.

2. Safety stops with cushion should be installed near both ends of the rail to avoid the graphite piston hitting rubber seals on both ends of the pneumatic cylinder.

3. Certain space should be reserved for effortless hand access to assembly and adjustment.

4. The position of the linear strip encoder should be adjustable. The clearance between the optical encoder LED reader and linear strip should be tuned to meet the requirement. Too far or too close will bring encoder count loss.

5. The cost of the material and fabrication should be reduced while satisfying the rigidity requirement.

6. The system should be designed such that it can be mounted on the optical breadboard so as to ensure accuracy.

7. The system should be designed with capacity to be operated under low speed due to some possible applications such as brachytherapy, in which the needle insertion speed is between 1 mm/sec to 50 mm/sec as shown in [57].

To achieve 1 DOF movement, the pneumatic cylinder is connected to a adjustable carriage with weights on a "T" shape linear guide. As the damper and the constant force spring need to be connected to the loads, the pneumatic cylinder, the damper, the spring and the carriage should be placed in the same plane so as to minimize the fiction induced by bending torque and misalignment. We have two choices of plane, horizontal plane or vertical plane. The vertical clearance between the carriage and the linear guide is smaller than the horizontal clearance, hence allowing less displacement in the corresponding direction when actuated with offset distance. For the purpose of minimizing friction induced by misalignment, the vertical plane configuration is preferred.

The pneumatic cylinder is fixed to a vertical holder with a screw. However, it is observed that the pneumatic cylinder can hardly be aligned with the linear guide without additional holder for positioning. Thus a stand with a semi hole, serving as a positioner, is placed by the rod cap to increase the alignment accuracy and rigidity.

The travel range of the damper is shorter than that of the pneumatic cylinder. Thus the damper is installed on the stand, allowing both of the pneumatic cylinder and the damper to work within the travel range confined by the two safety stops without adding new components.

To cut the cost of the material and fabrication, rapid prototyping machine is employed to fabricate the stand for the cylinder, the stand for the linear guide, the cylinder holder, the safety stops, the linear strip holder, the panel connecting the load cell and the carriage and the plate for weights. Supporting braces are added to the stands, the holder and the panel to ensure the required rigidity.

Due to various sizes of different weights, a universal clamp is too complicated to be adopted. In order to maintain the simplicity of the mechanism, a replaceable plate is fixed on the carriage such that the weight can be glued on the plate. The merit lies in that the weight can be knocked off the plate once on longer in use and the used plate can be easily replaced with a new one for low cost.

The linear strip holder is fixed alongside the linear guide. The linear strip is placed in thin straight groove, the width of which is larger than that of the linear strip. With a thin piece of plastic plate placing in front or behind the linear strip, the position of the linear strip can be adjusted such that the clearance requirement between the linear strip and the optical encoder LED can be attained. Three perpendicular screw holes are drilled with respect to the linear strip plane, allowing brass screws to fasten the linear strip. Also a thin piece of sponge is placed between the screw end and the

linear strip so as provide cushion, avoiding deformation of the plastic linear strip.

Figure 2.4 shows the Solidworks 3D model of the mechanical structure of the pneumatic actuator test system.

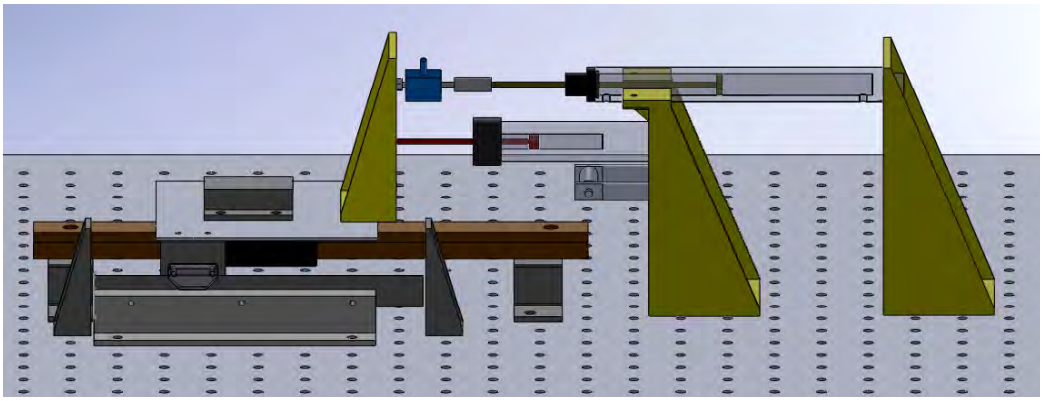

Figure 2.4: The mechanical structure of the pneumatic actuator test system. Noted that weights can be glued on the replaceable carriage, constant force spring can be mounted on the arm below the damper and the damper is attached to the load.

2.3.2 System Components Selection

The pneumatic actuation test system components are listed in Tab. 2.1.

Component	Description
Optical table surface	1/4-20 Taped Holes 1” Grid 2” Height
Linear guide	300 mm of rail, 1 shuttle, standard shuttle design
Position sensor	LIN Transmissive Linear Strip 500 CPI Index 0.5 Inch
Spring	Stainless Steel Constant-Force Spring
Pressure sensor	Pressure Sensor 0 - 10 V DC Output Stainless Steel
Force sensor	10 lb , JR S-Beam Load Cell , Standard
Damper	Bore: .627” Two-Way Stroke: 3.0 in 0-0.88 N/(mm/s)
Valve	3-way proportional pressure valve, Current controlled
Pneumatic Cylinder	Bore: .366 OUTSIDE DIAMETER .462 10lbs 100psi

Table 2.1: The pneumatic actuation test system components

2.3.2.1 MRI-compatible Pneumatic Cylinder

The MRI-compatible Pneumatic Cylinder is developed by Fischer [20]. The pneumatic cylinder with 9.3 mm bore and 114 mm stroke is made of glass bore, graphite piston and brass shaft in a plastic housing. Figure 2.5 shows the custom MRI-

compatible pneumatic cylinder with a rod lock. The upper pressure limit of the pneumatic cylinder is 689 kPa (100 psi) and the diameter of the bore is 9.3 mm. Thus the maximum actuation force of the pneumatic cylinder is 46.8 N.

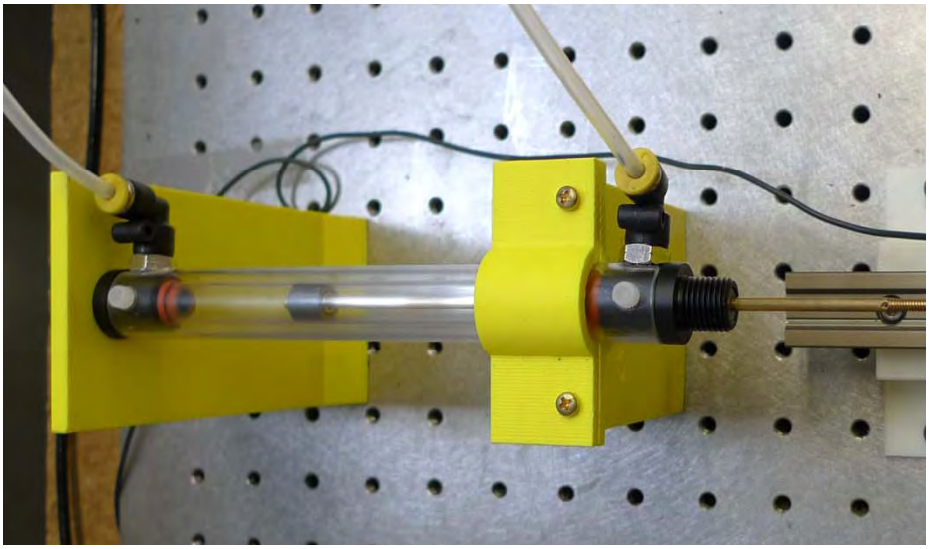

Figure 2.5: The custom MRI-compatible pneumatic cylinder with a rod lock [58]

2.3.2.2 Piezoelectric Pressure Regulated Valve

As mentioned above, pressure regulated valve is preferred for directly controlling output air pressure and hence simplifying the system modeling. The control algorithm selected is SMC, which features fast switching control signal, known as chattering. Such chattering effect demands fast response of the control valve. The response time of the piezoelectric valve is below 20 ms with dead time of 30 ms.

The damping ratio of the valve is tunable, which simplifies the valve modeling

when the valve is tuned to over-damped. Also inherent safety of limiting pressure to a pre-determined value and MRI compatibility with proper shielding make the piezoelectric valve our first choice in valve selection. Figure 2.6 shows two piezoelectric valves with a multiple base plate. The piezoelectric valve can regulate pressure up to 100 psi with control input ranging from 4 mA to 20 mA.

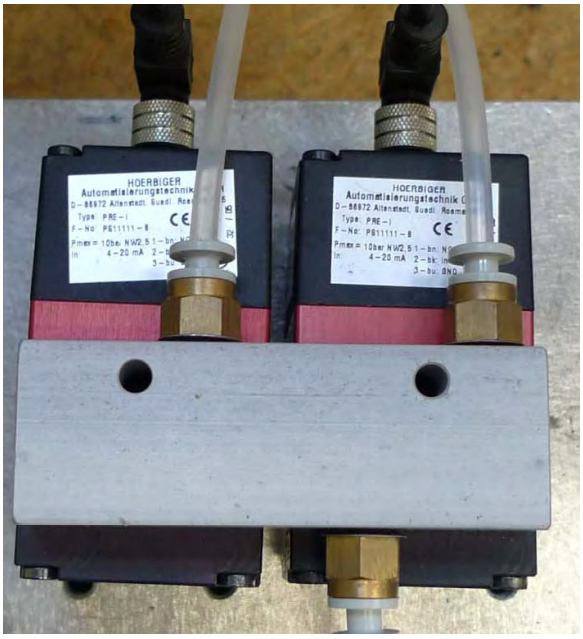

Figure 2.6: Two piezoelectric valves with a multiple base plate

2.3.2.3 Load Cell

A force sensor is required to measure the actuation force. Since the actuation is a push-pull procedure, bi-direction measurement is an essential feature of the sensor. Compactness, light weight and high accuracy make the load cell preferable. The load

cell is capable of measuring up to 10 lb and the magnitude of output is 10 V. The load cell is shown in Fig. 2.7.

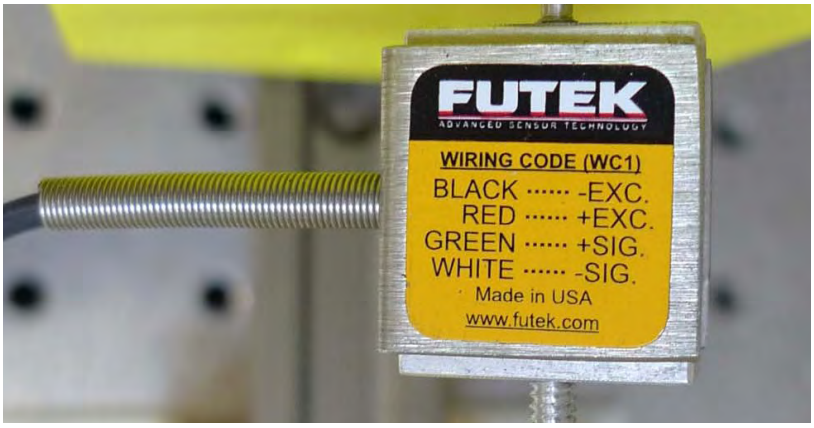

Figure 2.7: The load cell connected to the amplifier

2.3.2.4 Optical Encoder

The linear optical encoder provides a resolution of 2000 counts per inch (0.0127 mm precision) with quadrature mode, which is sufficient for high accuracy measurement of the carriage position. With proper choice of fasteners and shielding techniques, the encoder is also proved MRI-compatible [5]. The optical encoder with linear strip fixed on the optical breadboard is shown in Fig. 2.8.

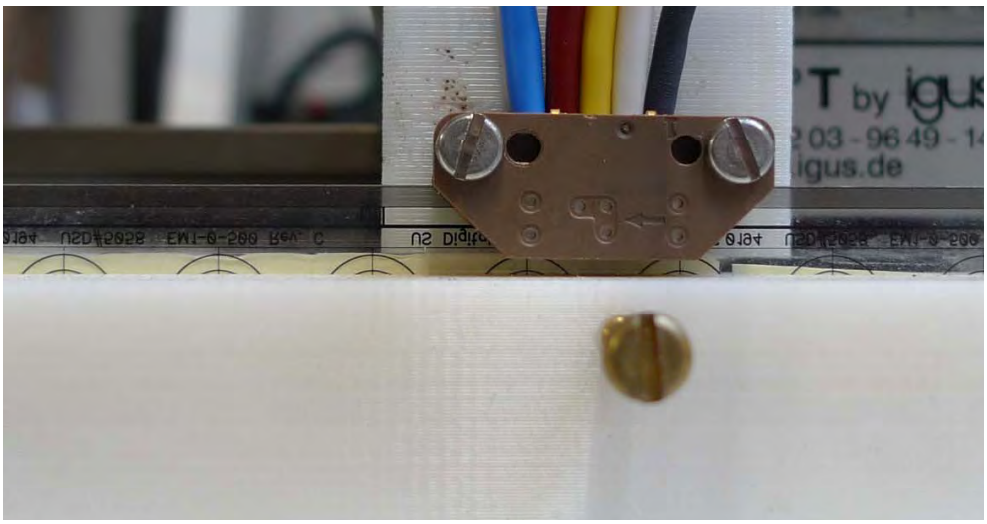

Figure 2.8: The optical encoder with linear strip

2.3.2.5 Load Components

Three kinds of load components are utilized in the system. Weights are employed as load components to test the robustness of the control algorithms. The pneumatic cylinder may overshoot when tracking a step function and hence a tunable damper is used to ensure an over-damped system. This, however, comes with the expense of sacrificing response time. A constant force spring can be integrated to the system, serving as the simulation of gravity. The damper and the weights are shown in Fig. 2.9.

2.3.2.6 Air Supply

As mentioned above, the upper pressure limit of the pneumatic cylinder is 100 psi and the actuator requires clean and smooth air flow. Since the lab already has compressed air supply, air filtering is required and the control over the input pressure of piezoelectric valve would bring convenience to the test. Aside from the requirements above, a small air tank is needed to smoothen air flow. Figure 2.10 shows the air supply with on-off switch and pressure regulator.

2.4 Controller Design

2.4.1 Hardware Design

2.4.1.1 Voltage to Current Convert Board

The analog output of the control servo board is 0-10 V. However, the input of the piezoelectric valve is 0-20 mA. A linear voltage to current convert circuit is required to convert the voltage to the corresponding current. Voltage-to-current Transmitter IC AM422 is selected due to that it features adjustable gain and offset, protection against reverse polarity and input voltage limitation.

For future application concern, the circuit board should support up to 8 channels of output. The circuit schematic drawing is shown in Fig. 2.11. The power input of the board is wired to the 5 V power supply and the control inputs are wired to

the analog output port 1 and 2 of the control servo board. The configuration of the board is shown in Fig. 2.12.

2.4.1.2 Modular Control Servo Board

The purpose of modular control servo board is to construct a stand-alone system in PIC 32 that is capable of performing real-time control loops with an interface to PC program that provides set points input. It also provides on-board interfaces for quadrature optical encoder and voltage sensors. The board is developed by Kevin Harrington. The configuration of the modular control servo board is shown in Fig. 2.13.

2.4.2 Software Design

The software of the system is composed of two parts, the program that runs on the control servo board and the program that runs on the PC. The configuration of the communication of the programs is shown in Fig. 2.14.

The program implemented in the control servo board is designed with reference to the Bowler Communication library developed by Kevin Harrington. The software platform includes: C programming language in Eclipse integrated development environment (IDE), Bowler Communication interface and Matlab.

The control program receives position tracking function from PC through remote procedure call (RPC) package. Then pressure and position data are transmitted to

the control servo board. Control output data are calculated based upon the sensor data in real time. The time interval between each loop is fixed at 1 ms. The sensor data can be sent to the PC via synchronous or asynchronous mode. A threshold of position change is implemented to determine if the position has been reached. Once the change is less than the threshold, the controller can trigger the lock device to fix the rod of the pneumatic cylinder in current position so as to avoid any extra movement induced by external disturbance. The data collected in PC are analyzed in Matlab.

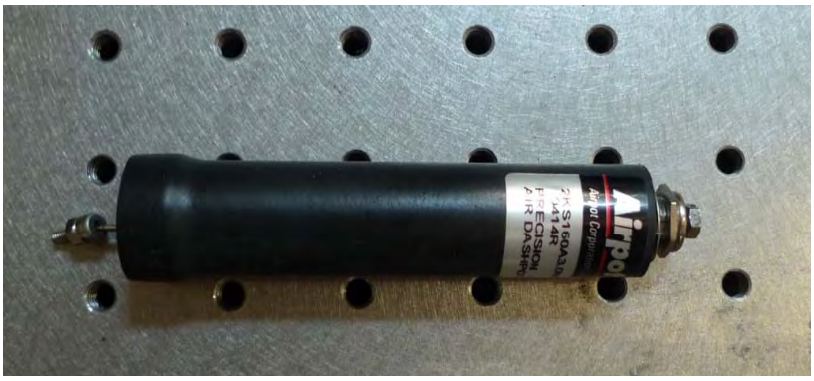

(a)

(b)

Figure 2.9: The damper and the weights

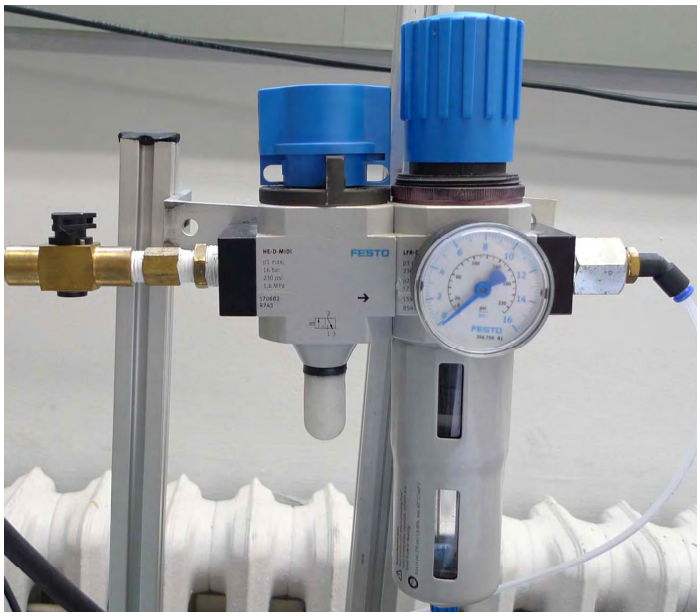

Figure 2.10: The air supply with on-off switch and pressure regulator

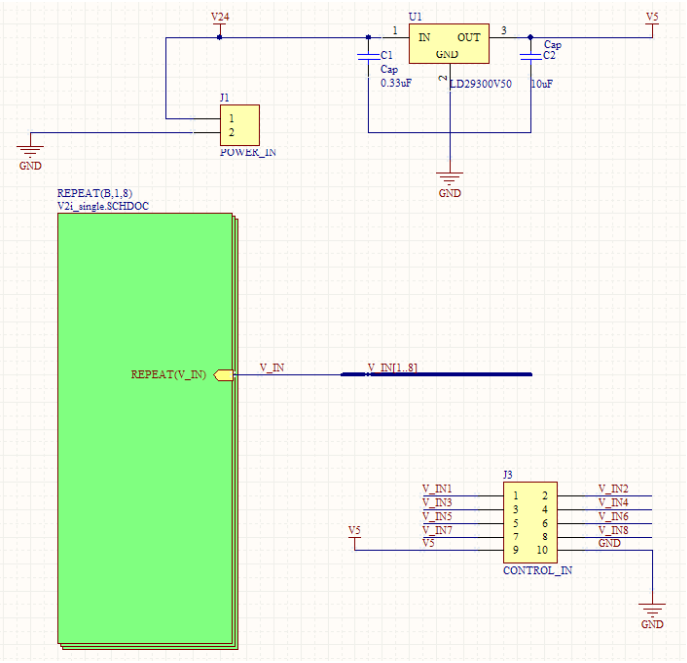

(a)

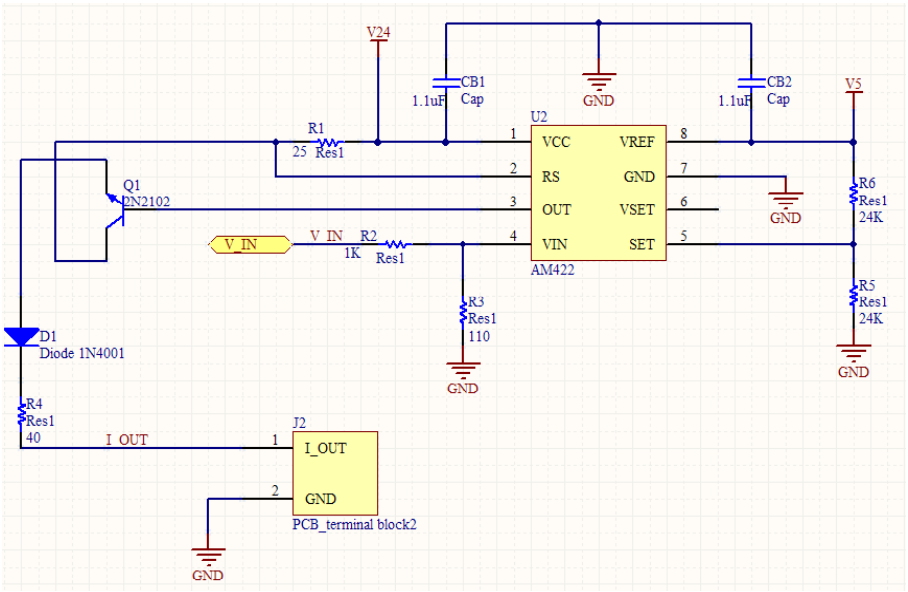

(b)

Figure 2.11: The schematic drawing of the voltage to current convert circuit

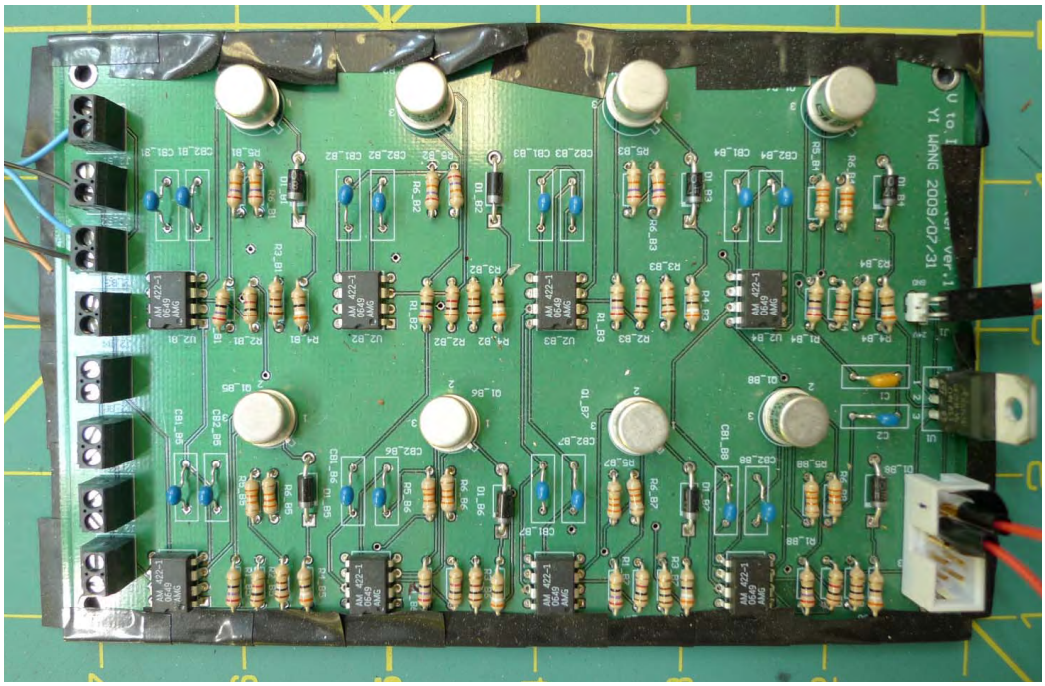

Figure 2.12: The configuration of the voltage to current convert board

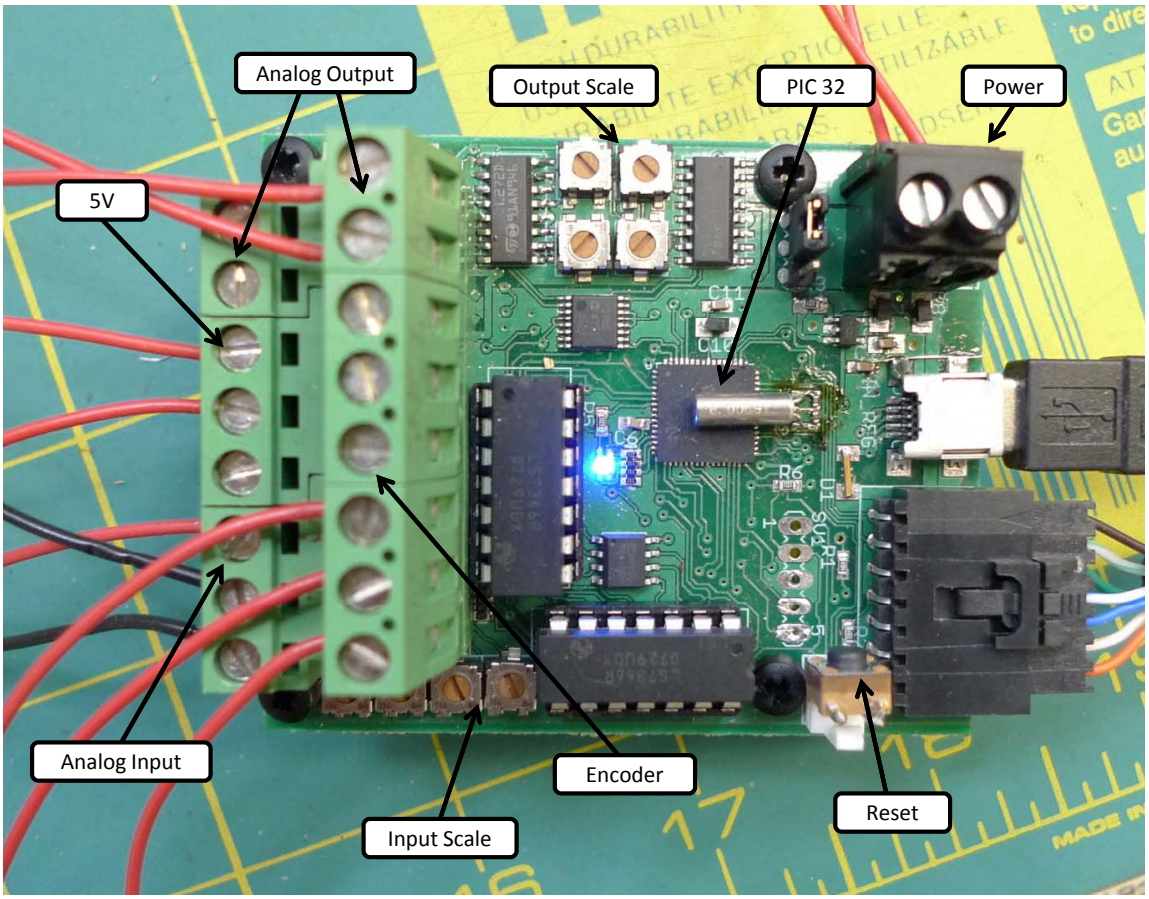

Figure 2.13: The configuration of the modular control servo board

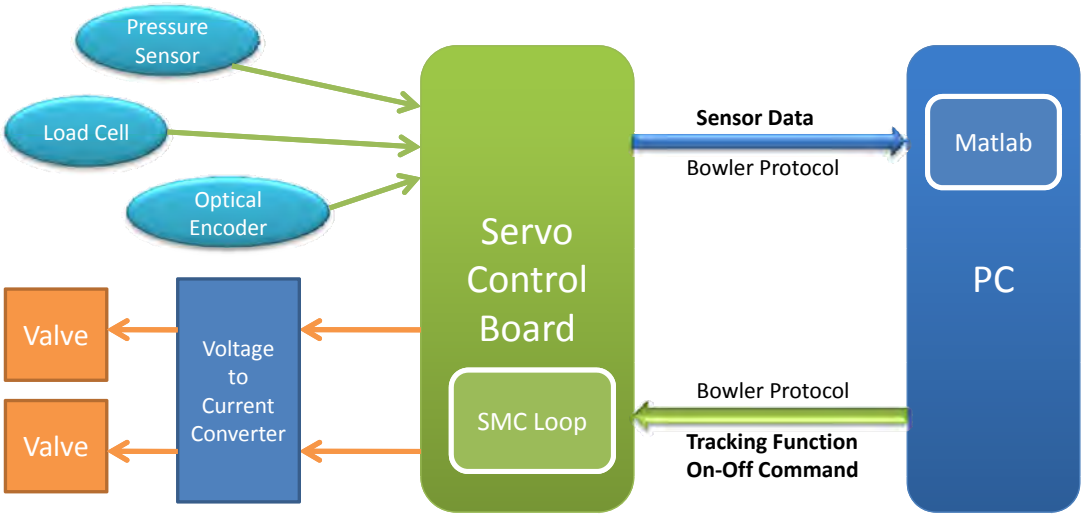

Figure 2.14: The configuration of the system block diagram

Chapter 3

PNEUMATIC ACTUATION TEST SYSTEM MODELING

Traditionally, a pneumatic actuator is controlled by flow regulated valves, which gives no direct access to the pressures of the two pneumatic cylinder chambers. Thus compressibility and viscosity of air must be considered when establishing pneumatic cylinder model, cylinder-valve connecting tube model and valve model. Wang *et al* proposed an analysis of the pneumatic cylinder actuator systems based on the standard orifice theory [59]. Richer and Hurmuzlu [60] introduced a mathematical model consisting of dual action pneumatic actuators controlled by proportional spool valves. Tressler *et al* modeled a pneumatic system with approach utilizing thermodynamic principles of energy and mass conservation [61]. A model of a non-autonomous dynamic equation with consideration of the valve dynamics was proposed by Tsai *et*

al [62].

In this system, however, such complexity in modeling was significantly reduced by replacing the conventional flow-rate regulated valve with pressure regulated piezo valve. With help of pressure regulated piezoelectric valve, we now have direct access to controlling pressure of output air flow, indicating that the pressure variable can be treated as a known one in pneumatic cylinder modeling. Also the linear relationship between control signal and output air pressure, high sensitivity and low hysteresis simplifies the valve modeling.

3.1 Pneumatic Cylinder Modeling

The schematic of the pneumatic cylinder used in the test fixture is shown in Fig. 3.1 by Fischer [58].

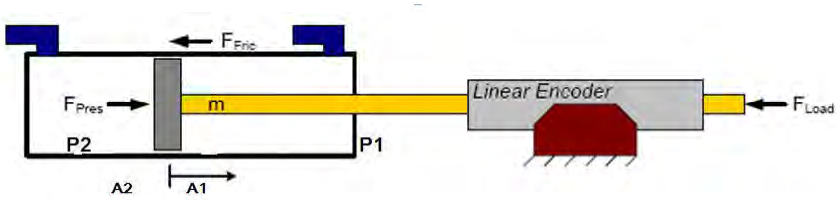

Figure 3.1: Schematic of the MRI-compatible pneumatic cylinder model. Noted that m is the mass of all moving components

Begin modeling with description

$$F_{pres} - F_{ext} = m\ddot{x} \tag{3.1}$$

where F_{pres} is the force generated by pressure difference of the two chambers, F_{ext} is the total external force, m is the moving mass of the whole system, including piston, brass rod, adaptor, load cell, carriage and encoder, and x is the position of the cylinder.

We also know that

$$F_{pres} = P_1 A_1 - P_2 A_2 \tag{3.2}$$

$$F_{ext} = F_{load} + F_{fric} \tag{3.3}$$

$$F_{fric} = \mu_v \dot{x} + \mu_c sign(\dot{x}) \tag{3.4}$$

where P_1 and P_2 are pressure of the two chambers, A_1 and A_2 are the piston area of the two chambers, F_{ext} is the external load, F_{fric} is the total friction, μ_v is the coefficient of viscous friction, μ_c is the coulomb friction, which is composed of the friction of the cylinder and the friction of the carriage.

Substitute Eq. (3.2), (3.3), (3.4) into (3.1), we get

$$\ddot{x} = \frac{1}{m}[P_1 A_1 - P_2 A_2 - F_{load} - \mu_v \dot{x} - \mu_c sign(\dot{x})] \tag{3.5}$$

and that

$$A_1 = \frac{\pi}{4} d_1^2 \tag{3.6}$$

$$A_2 = \frac{\pi}{4}(d_1^2 - d_2^2) \tag{3.7}$$

where d_1 and d_2 are the diameter of the chamber and the diameter of the brass rod respectively.

Assume no external load is applied to the cylinder. Thus we can derive

$$\ddot{x} + \frac{1}{m}\mu_v \dot{x} + \frac{1}{m}\mu_c sign(\dot{x}) = \frac{1}{m}u \tag{3.8}$$

where u is the control input and obviously $u = F_{pres}$. If we let the control input $u = kx$, where k is the effective spring constant of the pneumatic cylinder holding it at the set point $t = 0$, the pneumatic cylinder is a second order system.

3.2 Piezoelectric Valve Modeling

The step responses of the piezoelectric valves are shown in Fig. 3.2 (a) and (b). Noted that the piston is placed at the end of the cylinder so that it cannot move when the testing chamber is pressurized. As we can see, the valve exhibits a dead time in step response. The FOPDT model is

$$\frac{C(s)}{R(s)} = \frac{Ke^{-t_0 s}}{\tau s + 1} \tag{3.9}$$

where t_0 is the dead time, K and τ are first order system parameters. In order to simplify this model, we use a first-order expansion to approximate the exponential term

$$e^{-t_0 s} \cong \frac{1}{t_0 s + 1} \tag{3.10}$$

Substituting Eq. (3.10) into Eq. (3.9), we have

$$\frac{C(s)}{R(s)} \cong \frac{K}{(\tau s + 1)(t_0 s + 1)} \tag{3.11}$$

Write Eq. (3.11) in differential equation form

$$t_0 \tau \frac{d^2 C(t)}{dt^2} + (t_0 + \tau)\frac{dC(t)}{dt} + C(t) = KR(t) \tag{3.12}$$

The pneumatic cylinder is driven by the pressure difference of the two chambers. In practice, setting an identical pressure in both chambers in steady state and offsetting each one precisely is hard to achieve. Therefore, we seek to actuate one valve at a time and keep the other one shut. Since the tubes connecting the valve and the

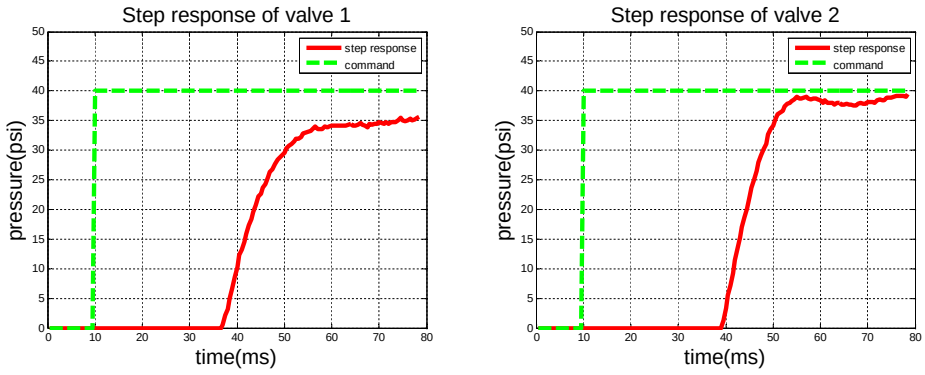

(a) (b)

Figure 3.2: Step responses of the piezoelectric pressure regulator valves in which the pressure sensors are placed near inlets of the cylinder

pneumatic cylinder are sufficiently long, pressure variance of the chamber of which the control valve is shut down can be neglected. Figure 3.3 shows the pressure of the chamber of which the control valve is shut down and the other control valve fully opens. Noted that chamber 2 response shows a decreasing pressure for that the volume of that chamber was enlarged during the actuation process. For our model, $C(t)$ is the pressure of chamber, namely $P_1(t)$ or $P_2(t)$. $R(t)$ is the control signal from servo board, $U_{volt1}(t)$ or $U_{volt2}(t)$.

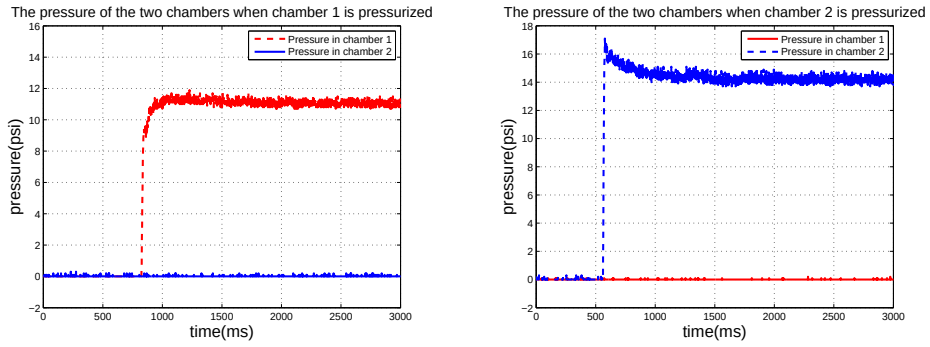

(a) (b)

Figure 3.3: Pressure of the chamber being shut down while the other one fully open

Chapter 4

DESIGN OF CONTROL ALGORITHMS AND SIMULATION

4.1 Sliding Mode Control Fundamentals

Let X be denoted as the position of the pneumatic cylinder. According to Eq. (3.8), the state of the system is $\vec{X} = (x, \dot{x})^T$. Our goal is to ensure that the state $\vec{X}$ follows the desired state $\vec{X}_d$. The error, $\vec{E}$, is defined as

$$\vec{E} = \vec{X}_d - \vec{X} = (e, \dot{e})^T \tag{4.1}$$

For the pneumatic cylinder plant, a suitable sliding surface function is

$$S = \lambda E + \dot{E} \tag{4.2}$$

where λ represents the slope of the line $S = 0$ in the plane $(e, \dot{e})$. The solution of $S = \lambda E + \dot{E} = 0$ is

$$e(t) = e(0)\exp(-\lambda t) \tag{4.3}$$

In order to ensure $e(t)$ converges to zero, we need to satisfy

$$\lambda > 0 \tag{4.4}$$

If the states converge to the sliding surface, we derive that $\dot{S} = 0$. In order to make sure that the states always approach the sliding surface, the following condition must be met

$$S \bullet \dot{S} < 0 \tag{4.5}$$

We know that the selection of $\dot{S}$ is not unique. Since $\dot{S}$ is the speed that sliding surface function converges to zero, we can achieve fast system response with small steady state error (SSE) with carefully chosen $\dot{S}$ function. In the following three subsections, three $\dot{S}$ functions are presented and in the following section.

4.2 Sliding Mode Control Scheme 1

Usually, the pneumatic cylinder control input u is implemented with two elements

$$u = u_{eq} + u_s \tag{4.6}$$

where u_{eq} is the equivalent control signal to keep the state on sliding surface once reached and u_s is the switch function that compensate the state when leaving the sliding surface.

To derive u_{eq} , substitute Eq. (3.8) and Eq. (4.1) into Eq. (4.2), take derivative of both sides and set left side equals to zero, we get

$$u_{eq} = m(\ddot{x}_d + \lambda_1 \dot{x}_d) + \dot{x}(\mu_v - \lambda_1 m) + \mu_c sign(\dot{x}) \tag{4.7}$$

The simplest form of the switching control u_s is a proportional switch function

$$u_s = k_1 sign(s) \tag{4.8}$$

where for $s > 0$, $sign(s) = 0$, for $s < 0$, $sign(s) = -1$ and for $s = 0$, $sign(s) = 0$.

However the switching function may bring chattering effect due to the discontinuity nature of $sign(s)$. To reduce chattering, it is replaced by a saturation function

$$u_s = k_1 sat(s/d_1) \tag{4.9}$$

where $k_1 > 0$ and for $|s| < d_1$, $u_s = k_1(s/d_1)$ and for $|s| \geq d_1$, the function becomes $u_s = k_1 sign(s/d_1)$.

The total control signal is determined by

$$u = m(\ddot{x}_d + \lambda_1 \dot{x}_d) + \dot{x}(\mu_v - \lambda_1 m) + \mu_c sign(\dot{x}) + u_s + k_1 sat(s/d_1) \tag{4.10}$$

The control parameters d_1, k_1 and λ_1 will be manually tuned. The plot of switching function of Scheme 1 is shown in Fig. 4.1.

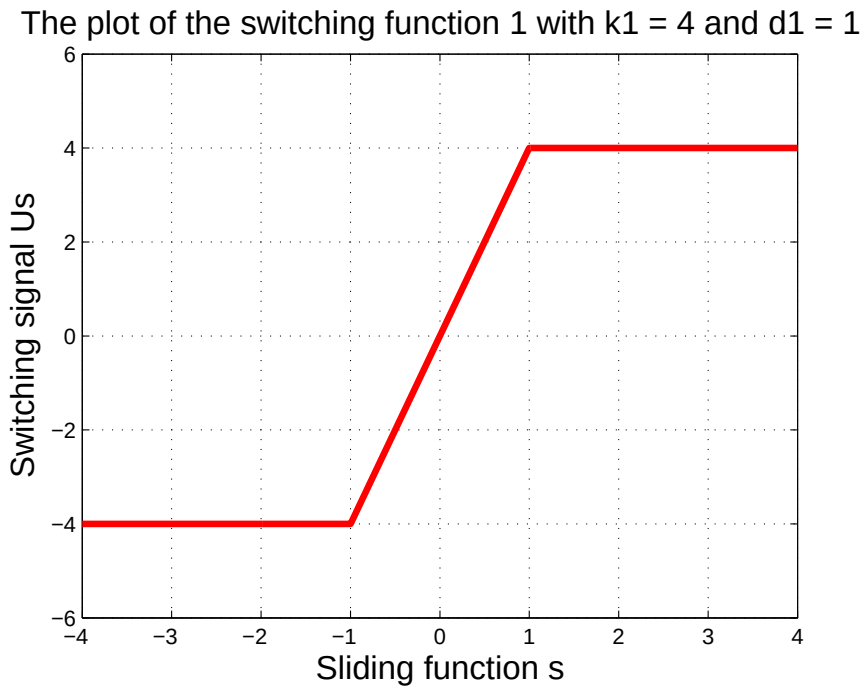

Figure 4.1: The switching function of Scheme 1 near switch band

4.3 Sliding Mode Control Scheme 2

Choose the $\dot{S}$ function to be

$$\dot{S} = -k_2|s|^a sat(\frac{s}{d_2}) \tag{4.11}$$

where $k_2 > 0$ and $a > 0$.

We know that

$$\dot{S} = \lambda_2\dot{E} + \ddot{E} = \lambda_2(\dot{x}_d - \dot{x}) + (\ddot{x}_d - \ddot{x}) \tag{4.12}$$

We know from Eq. (3.8) that

$$\ddot{x} = -\frac{\mu_v\dot{x}}{m} - \frac{1}{m}\mu_c sign(\dot{x}) + \frac{u}{m} \tag{4.13}$$

Substitute Eq. (4.13), Eq. (4.11) into Eq. (4.12), we can get a function of control signal

$$u = m[\ddot{x}_d + \lambda_2\dot{x}_d - \lambda_2\dot{x} + k_2|s|^a sat(\frac{s}{d_2})] + \mu_v\dot{x} + \mu_c sign(\dot{x}) \tag{4.14}$$

where the control parameters a, d_2 , k_2 and λ_2 will be manually tuned. The plot of switching function of Scheme 2 is shown in Fig. 4.2.

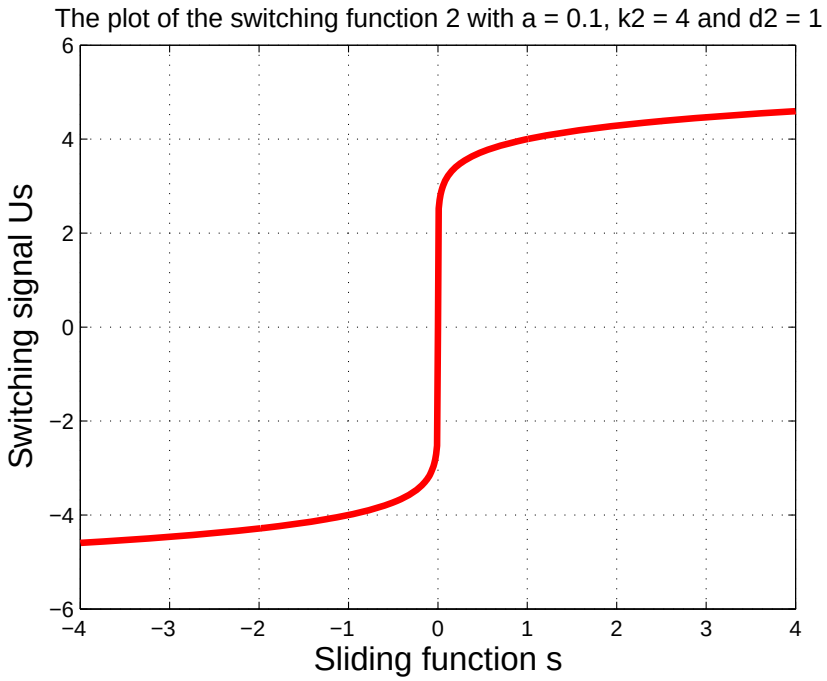

Figure 4.2: The switching function of Scheme 2 near switch band

4.4 Sliding Mode Control Scheme 3

Assume we choose $\dot{S}$ function to be

$$\dot{s} = -k_3 s \tag{4.15}$$

where $k_3 > 0$.

The solution is

$$s = s(0)e^{-k_3 t} \tag{4.16}$$

indicating that the sliding surface function will exponentially converge to the sliding surface.

This control scheme offers a quick response when far from the sliding surface. Once the system is in the vicinity of the sliding surface, converging speed decreases to a small amount such that desired response is not attained.

In order to improve the system performance, we can add a switching ramp function. Then $\dot{S}$ function is

$$\dot{s} = -k_3 s - \zeta sat(\frac{s}{d_3}) \tag{4.17}$$

where $\zeta > 0$ [63].

Similarly, substitute Eq. (4.13) and Eq. (4.17) into Eq. (4.12), we can derive the control signal

$$u = m[\ddot{x}_d + \lambda_3 \dot{x}_d - \lambda_3 \dot{x} + k_3 s + \zeta sat(\frac{s}{d_3})] + \mu_v \dot{x} + \mu_c sign(\dot{x}) \tag{4.18}$$

where the control parameters ζ , d_3 , k_3 and λ_3 will be manually tuned. The plot of switching function of Scheme 3 is shown in Fig. 4.3.

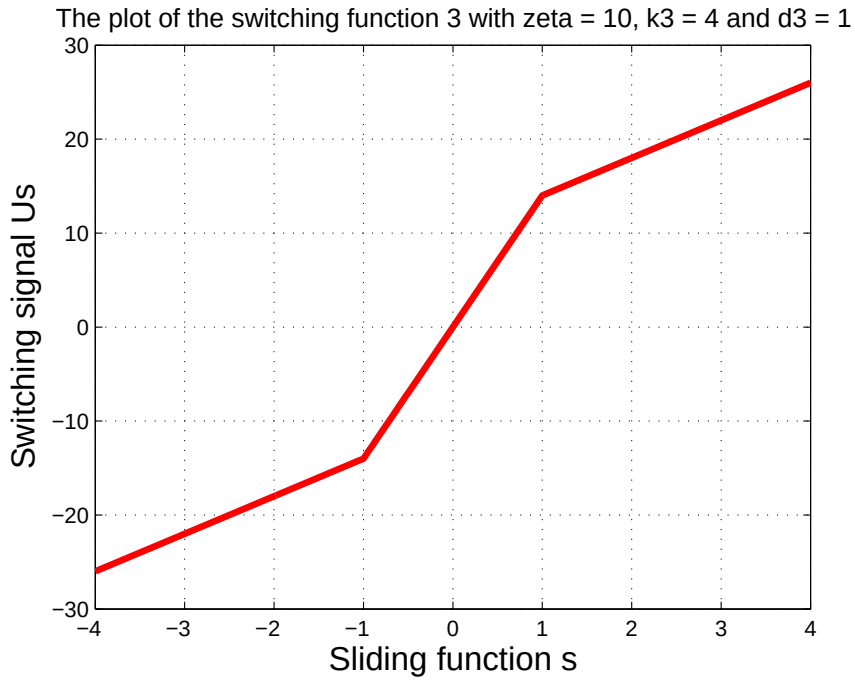

Figure 4.3: The switching function of Scheme 3 near switch band

4.5 Parameters Identification

Several parameters are to be determined prior to the Matlab simulation, which are the load mass, coulomb friction μ_c, and coefficient of viscous friction μ_v.

The load mass is measured with a scale. The load is defined as the components in the system being actuated when pressurized, which is composed of the carriage, the encoder, the carriage aluminium plate, the plate for weights, the weight, the the panel connecting the load cell, the load cell, the adaptor between the load cell and the rod, the brass rod, the graphite cylinder, the rod of the damper, and all the screws connecting each other. The measured load mass is 0.268 kg. The coulomb friction is measured with the load cell and optical encoder. The load cell records the actuation force once the cylinder starts to move very slowly due to manual push. The reading of the moment minus the reading of the relaxed state is the coulomb friction force of the system. The coulomb friction μ_c is 0.8 N. The viscous friction coefficient μ_v is measured according to $\ddot{x} + \frac{1}{m}\mu_v\dot{x} + \frac{1}{m}\mu_c sign(\dot{x}) = \frac{1}{m}u$. With prior knowledge of the load mass m and the coulomb friction μ_c, μ_v can be calculated with a series of tests. One chamber of the pneumatic actuator is pressurized and the other one is maintained in room pressure. Several actuation pressures are chosen based on the actuation speed range of the application, which are 15 psi, 20 psi, 25 psi, 30 psi, 35 psi. For each pressure, the mean of the viscous friction coefficient μ_v is computed. The computed viscous friction coefficient μ_v with respect to each pressure is shown in Fig. 4.4. The average of computed viscous friction coefficient μ_v is 22.8 Ns/m.

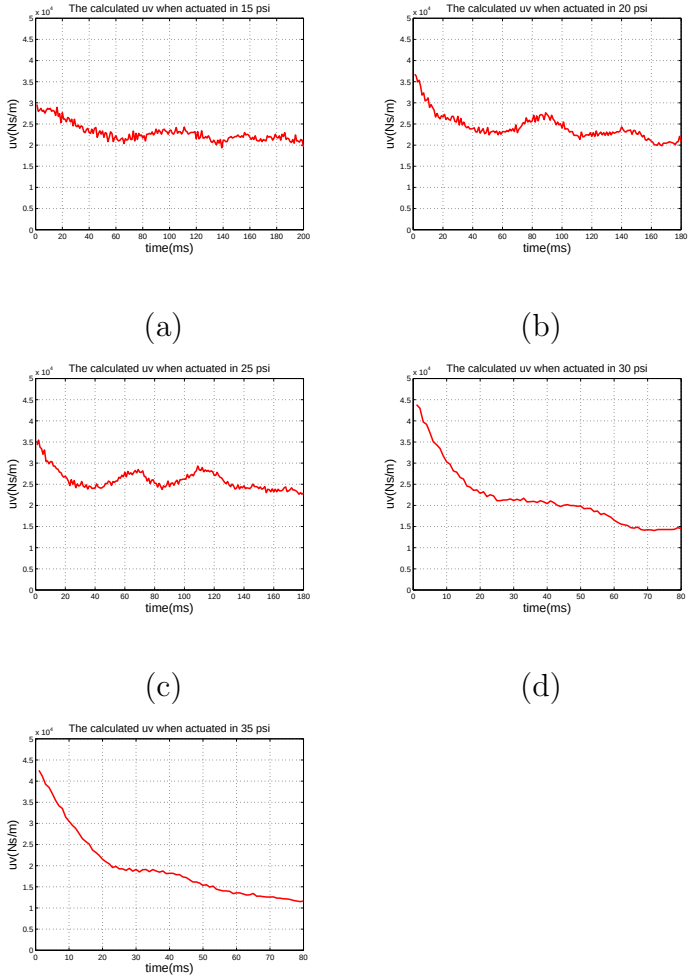

Figure 4.4: The computed viscous friction coefficient μ_v: 22.9 Ns/m in (a), 24.2 Ns/m in (b), 25.9 Ns/m in (c), 21.6 Ns/m in (d), 19.5 Ns/m in (e)

4.6 Simulation Results

4.6.1 Selection of Tracking Function and Parameters

The simulation of the system model was implemented in Matlab. The system initial state and reference input was defined before the simulation. Two types inputs were selected as reference for tracking: Sine wave function $x = 25.4\sin(0.1\pi t)$ mm with initial position error of 29.21 mm (1.15")for that it could be used in brachytherapy with the average speed of 5.08 mm/sec; Step function $x = 6.35(t)$ mm (0.25"), $x = 38.1(t)$ mm (1.5") and $x = 69.85(t)$ mm (2.75"). For convenience, the step functions listed below are written in inch unit unless specifically noted otherwise.

In order to evaluate the system response to a set position, step function is utilized to evaluate the time when the position tracking error is less than 0.1 mm. The accuracy requirement of 0.1 mm is chosen for that the maximum resolution of MRI is 0.1 mm. Due to safety concerns, it is desired that the performance is overdamped. $x = 0.25(t)$ is selected to test the performance of small movement. Mid-range performance is tested via $x = 1.5(t)$. And $x = 2.75(t)$ travels almost the full-range of the cylinder and hence is selected.

The sine wave with frequency of 0.05 Hz is selected since the speed of motion is appropriate for use in many robotic interventions. For example, the needle actuated

m	0.268kg	m_{w1}	0.05kg	m_{w2}	0.2kg
m_{w3}	0.5kg	m_{w4}	1kg	μ_v	22.8Ns/m
μ_c	0.8N	t_{sample}	0.001s	μ_{v2}	30.8Ns/m
λ_1	12	k_1	32	d_1	0.02
λ_2	16	k_2	108	d_2	0.01
λ_3	12	k_3	110	d_3	0.01
a	0.1	ζ	88		

Table 4.1: The identified parameters of the system and the manually tuned control scheme parameters of SMCr

by the pneumatic cylinder moves from one slot location to another in a sine wave pattern in brachytherapy.

Table 4.1 shows the identified parameters of the system and the manually tuned control scheme parameters for SMCr. m is the mass of all the moving components without loads. m_{w1}, m_{w2}, m_{w3} and m_{w1} are masses of weights employed in the tests. t_{sample} is the sampling time. μ_{v2} is the total damping ratio of the system with the damper attached.

4.6.2 Step Function Simulation Results

4.6.2.1 Results With No Load Attached

The simulated position tracking and sliding surface results for step function $x = 0.25(t)$ are shown in Fig. 4.5. The simulated position tracking and sliding surface results for step function $x = 1.5(t)$ are shown in Fig. 4.6. The simulated position tracking and sliding surface results for step function $x = 2.75(t)$ are shown in Fig. 4.7. The time when cylinder achieves 0.1 mm position tracking error is defined as the rise time.

All three algorithms attained the desired accuracy 0.1 mm for the three step functions. The rise time is 0.34 s, 0.27 s and 0.34 s respectively regarding step function $x = 0.25(t)$, is 0.48 s, 0.37 s, 0.49 s with respect to step function $x = 1.5(t)$ and is 0.53 s, 0.41 s, 0.54 s for step function $x = 2.75(t)$. The performance of Scheme 2 is better than Scheme 1 and Scheme 3 with respect to the rise time. Therefore, Scheme 2 is the most suitable control algorithm.

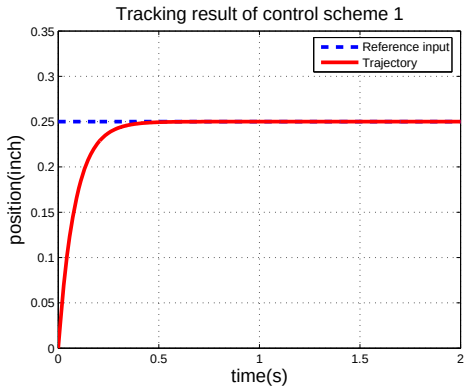

(a)Position tracking with rise time 0.34s

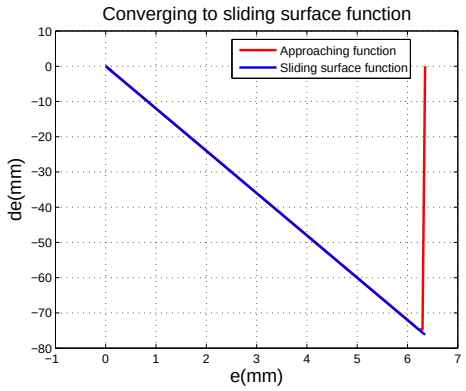

(b)Approaching function $\dot{S}_1$

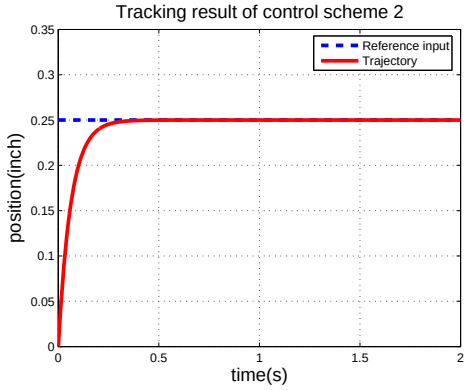

(c)Position tracking with rise time 0.27s

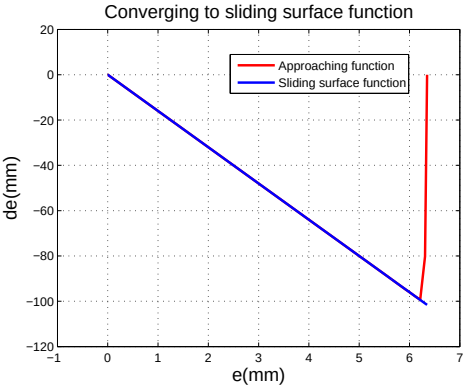

(d)Approaching function $\dot{S}_2$

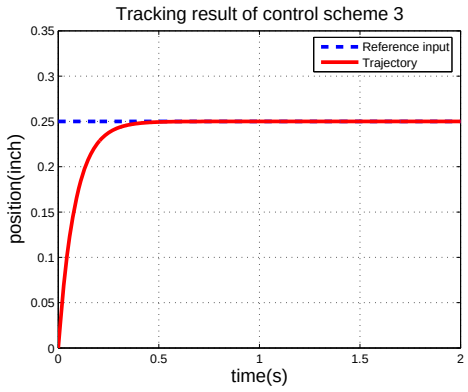

(e)Position tracking with rise time 0.34s

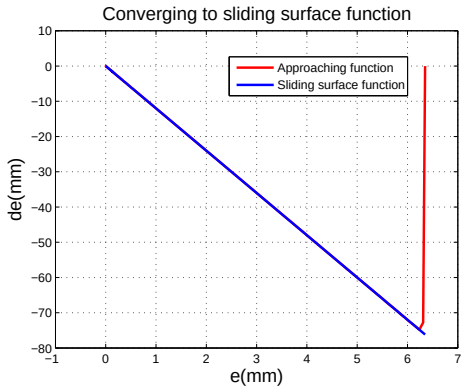

(f)Approaching function $\dot{S}_3$

Figure 4.5: Matlab simulation of position tracking plot and sliding surface plot comparing 3 SMC schemes for step function $x = 0.25(t)$

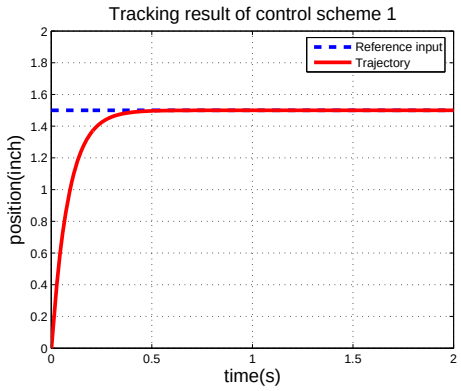

(a)Position tracking with rise time 0.48s

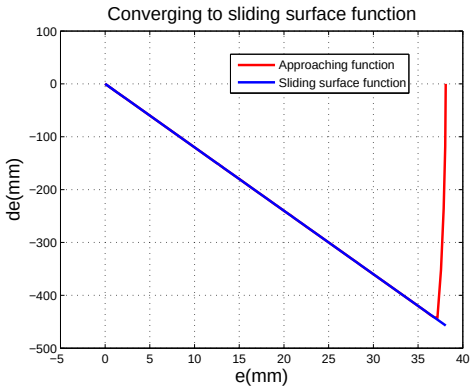

(b)Approaching function $\dot{S}_1$

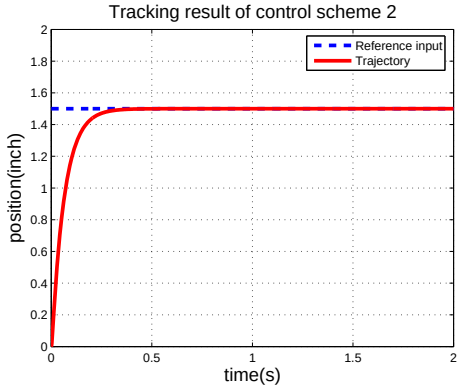

(c)Position tracking with rise time 0.37s

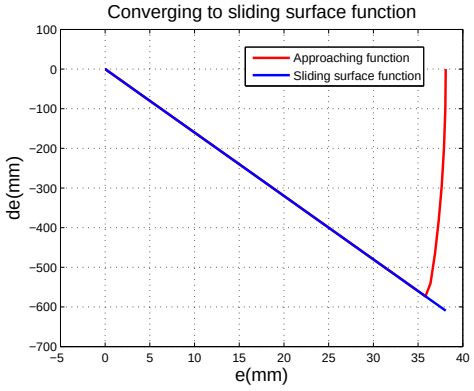

(d)Approaching function $\dot{S}_2$

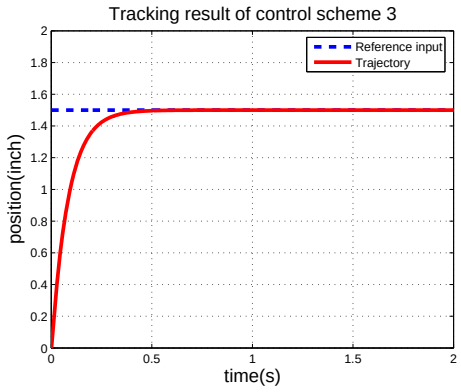

(e)Position tracking with rise time 0.49s

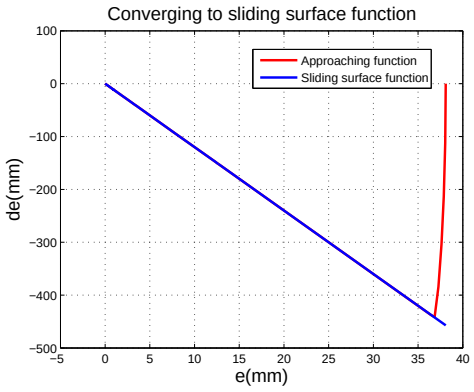

(f)Approaching function $\dot{S}_3$

Figure 4.6: Matlab simulation of position tracking plot and sliding surface plot comparing 3 SMC schemes for step function $x = 1.5(t)$

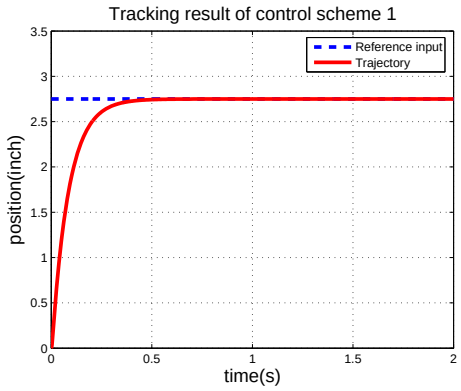

(a)Position tracking with rise time 0.53s

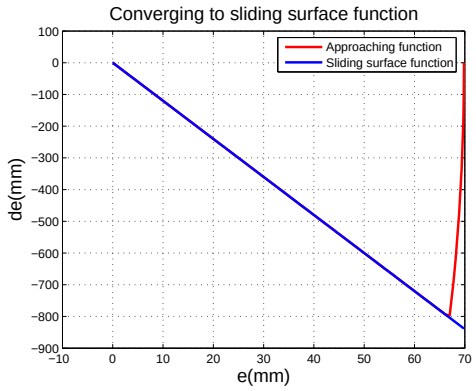

(b)Approaching function $\dot{S}_1$

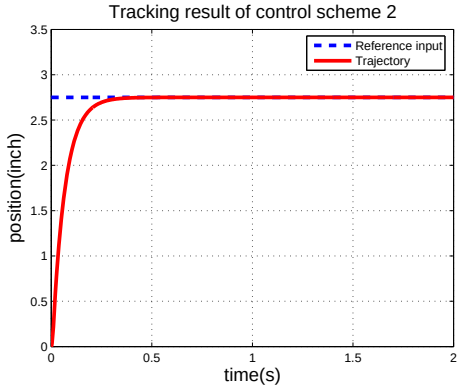

(c)Position tracking with rise time 0.41s

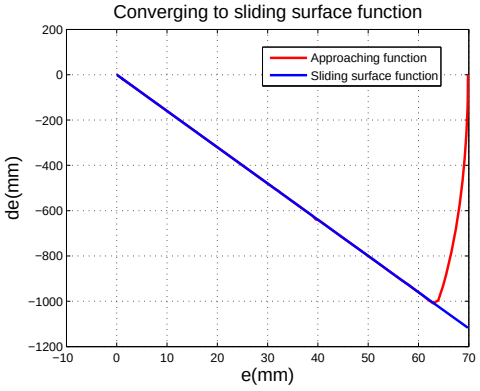

(d)Approaching function $\dot{S}_2$

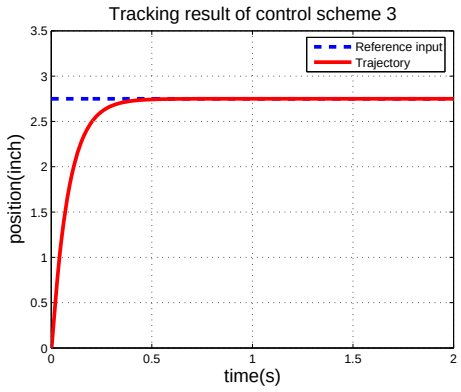

(e)Position tracking with rise time 0.54s

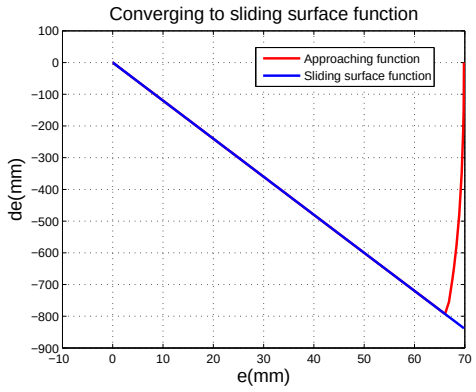

(f)Approaching function $\dot{S}_3$

Figure 4.7: Matlab simulation of position tracking plot and sliding surface plot comparing 3 SMC schemes for step function $x = 2.75(t)$

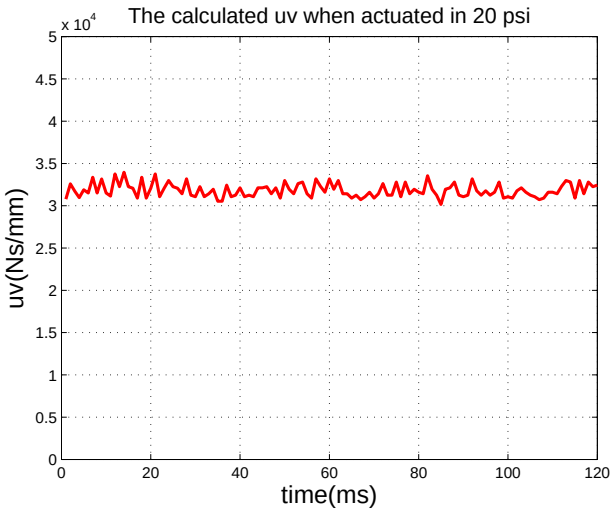

Figure 4.8: The computed μ_{v2} with the damper attached

4.6.2.2 Results With Damper Attached

In order to test the system performance under various viscous friction coefficient, a damper is attached in parallel with the pneumatic cylinder. The computed viscous friction coefficient μ_v of the system is shown in Fig. 4.8. The simulated position tracking results with a damper attached for step function $x = 0.25(t)$ are shown in Fig. 4.9 and results for step function $x = 1.5(t)$ are shown in Fig. 4.10. Figure 4.11 demonstrates the simulated position tracking results for step function $x = 2.75(t)$.

All three algorithms achieve the desired accuracy 0.1 mm with the damper connected. The rise time is 0.37 s, 0.28 s, 0.36 s for step function $x = 0.25(t)$ respectively, is 0.54 s, 0.38 s and 0.50 s with regards to step function $x = 1.5(t)$, is 0.56 s, 0.44 s, 0.55 s concerning step function $x = 2.75(t)$. Comparing with the results in which

no damper attached, we can observe that the rise times increase 0.03 s, 0.01 s, 0.02 s for $x = 0.25(t)$, 0.03 s, 0.01 s and 0.02s for $x = 1.5(t)$, 0.03 s, 0.03 s and 0.01 s for $x = 2.75(t)$. The performances of Scheme 2 and 3 are better than that of Scheme 1.

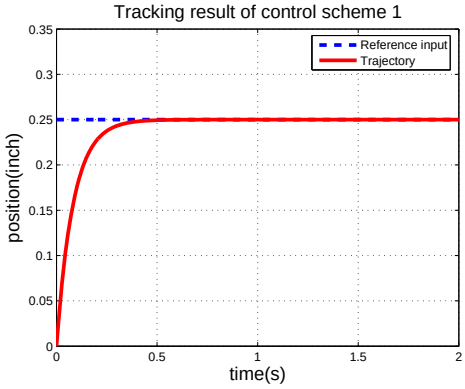

(a)Position tracking with rise time 0.37s

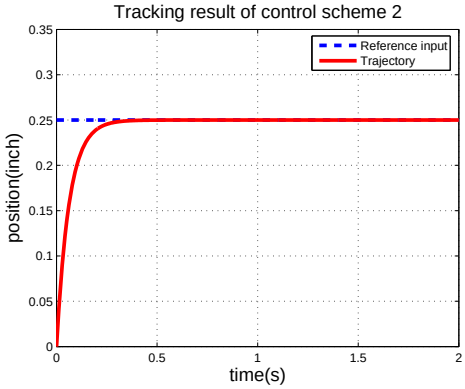

(b)Position tracking with rise time 0.28s

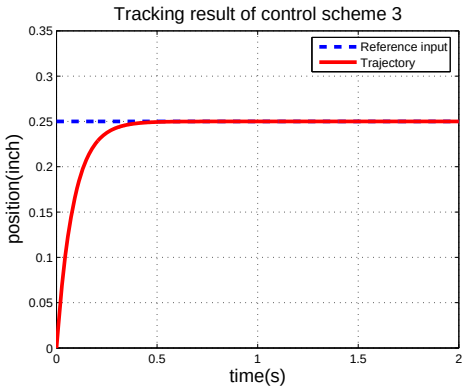

(c)Position tracking with rise time 0.36s

Figure 4.9: Position tracking plots with the damper attached for $x = 0.25(t)$

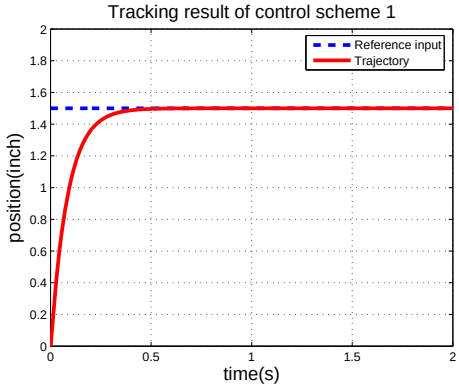

(a)Position tracking with rise time 0.51s

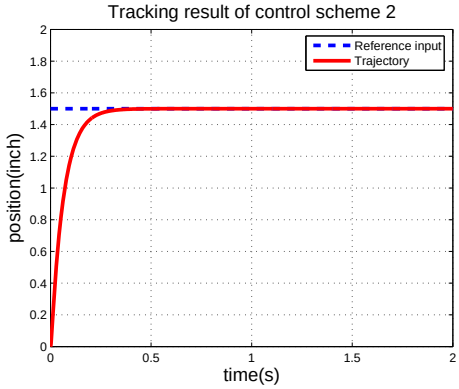

(b)Position tracking with rise time 0.38s

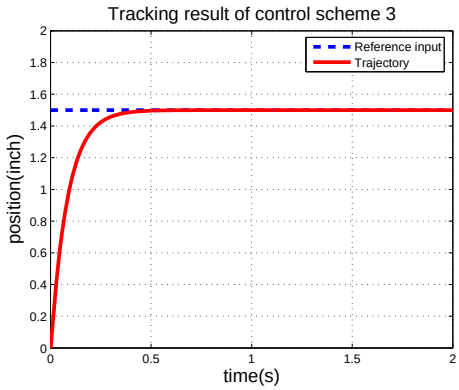

(c)Position tracking with rise time 0.51s

Figure 4.10: Position tracking plots with the damper attached for $x = 1.5(t)$

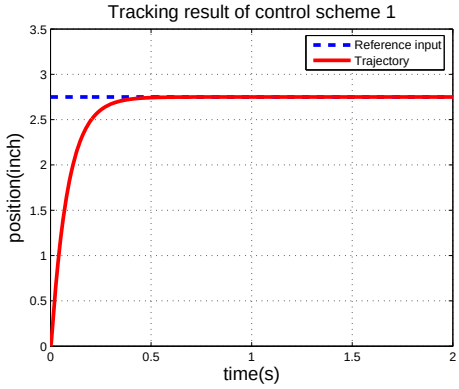

(a)Position tracking with rise time 0.56s

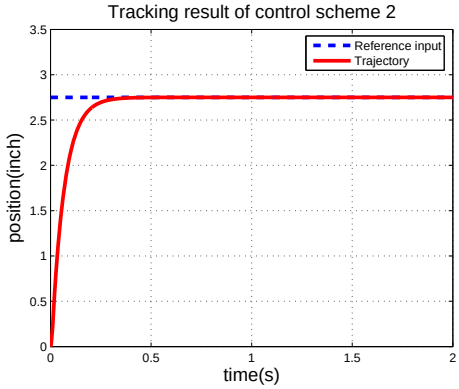

(b)Position tracking with rise time 0.44s

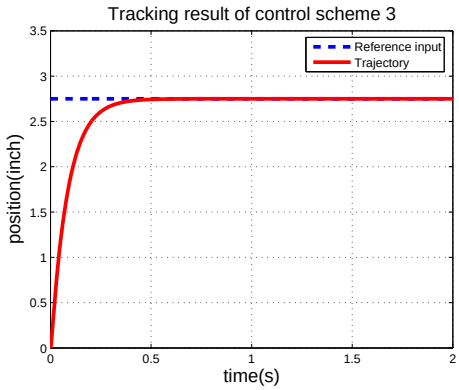

(c)Position tracking with rise time 0.55s

Figure 4.11: Position tracking plots with the damper attached for $x = 2.75(t)$

4.6.2.3 Results With Weight Attached

With purpose of testing the performance of each scheme under various external loads, several weights, namely 50 g, 500 g, are added to the carriage as the external load independently. The simulated position tracking results with a 50 g weight installed for the three step functions are shown in Fig. 4.12. All three algorithms achieve the desired accuracy 0.1 mm with the 50 g weight loaded. The rise time is 0.36 s, 0.27 s and 0.34 s with regards to step function $x = 0.25(t)$, is 0.51 s, 0.37 s and 0.49 s with respect to step function $x = 1.5(t)$, is 0.55 s, 0.41 s and 0.45 s for step function $x = 1.75(t)$. Comparing with the results in which no damper attached, we can observe that the performances of Scheme 2 is better than those of Scheme 1 and 3.

The simulated position tracking results with a 500 g weight installed for the three step functions are shown in Fig. 4.13. All three algorithms achieve the desired accuracy 0.1 mm with the 500 g weight attached. The rise time is 0.37 s, 0.29 s and 0.35 s with regards to step function $x = 0.25(t)$, is 0.54 s, 0.39 s and 0.50 s with respect to step function $x = 1.5(t)$, is 0.56 s, 0.43 s and 0.57 s for step function $x = 2.75(t)$. Comparing with the results in which no damper attached, we can observe that the performances of Scheme 2 is better than those of Scheme 1 and 3.

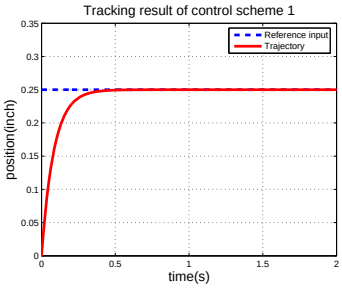

Rise time 0.36s

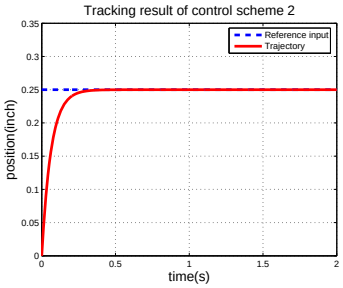

Rise time 0.27s

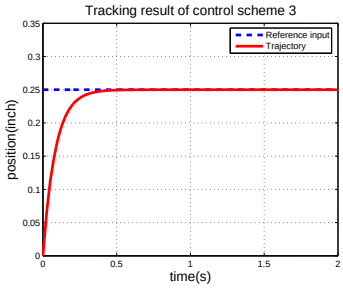

Rise time 0.34s

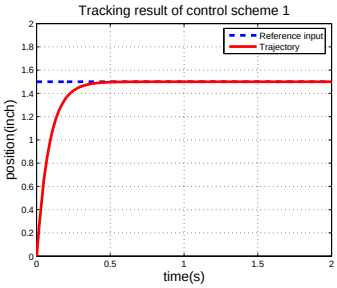

Rise time 0.51s

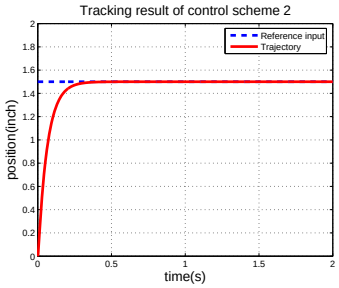

Rise time 0.37s

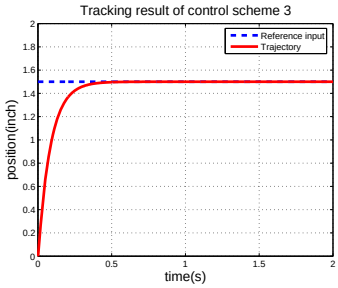

Rise time 0.49s

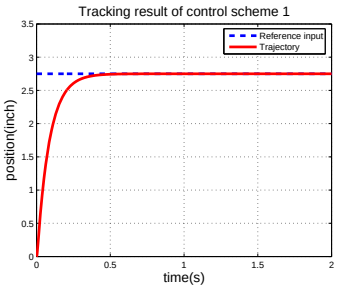

Rise time 0.55s

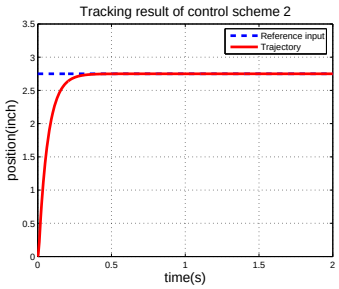

Rise time 0.41s

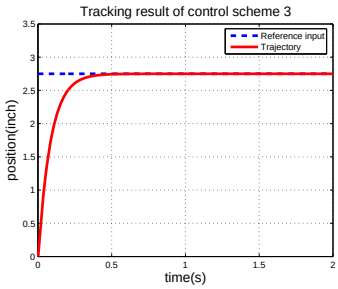

Rise time 0.45s

Figure 4.12: Position tracking plots with the 50 g weight installed

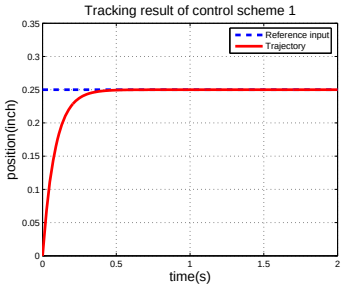

Rise time 0.37s

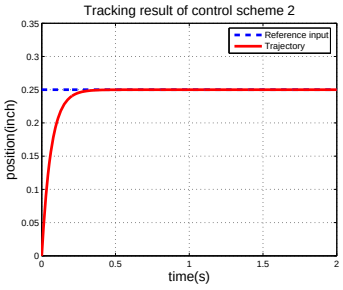

Rise time 0.29s

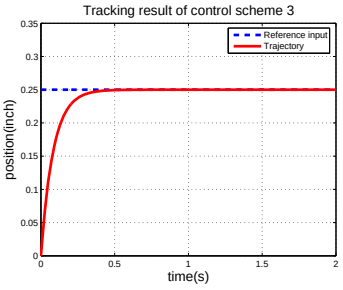

Rise time 0.35s

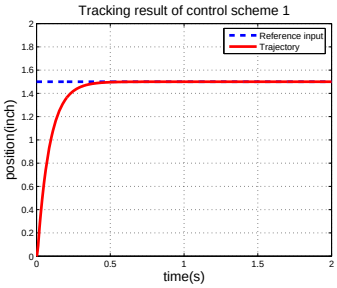

Rise time 0.54s

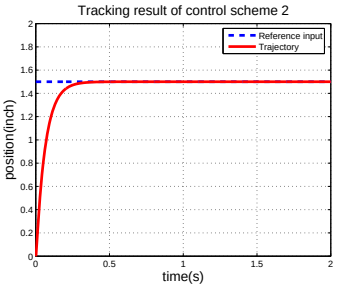

Rise time 0.39s

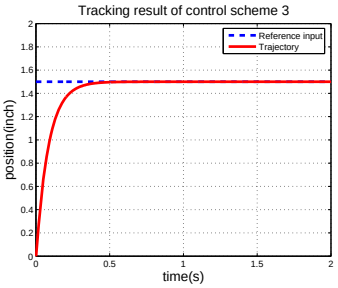

Rise time 0.50s

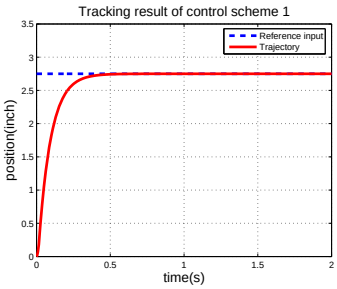

Rise time 0.56s

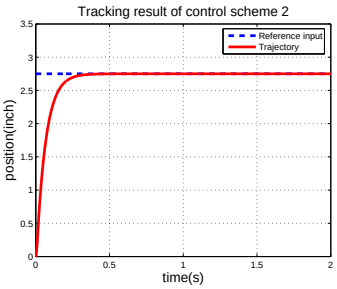

Rise time 0.43s

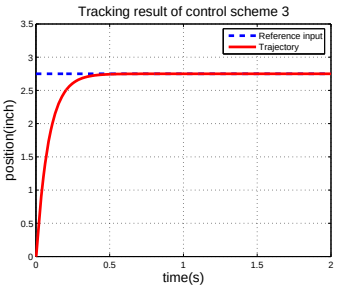

Rise time 0.57s

Figure 4.13: Position tracking plots with the 500 g weight installed

4.6.2.4 Results With Static Friction

In the previous simulation model, the static friction μ_s is assumed to be the same as the coulomb friction μ_c and hence is not included in the model. In fact, the static friction is larger than coulomb friction. In order to test the influence of static friction, μ_s is included in the model once the system stops. μ_s is measured with load cell and optical encoder. The load cell records the force of the moment before the cylinder moves with manual push. The measured static friction is 0.9 N. The simulated position tracking results of Scheme 1 with no load installed for $x = 0.25(t)$ and the sliding surface function are shown in Fig. 4.14. We can observe that the rise time was 0.04 s slower than that of the model without static friction.

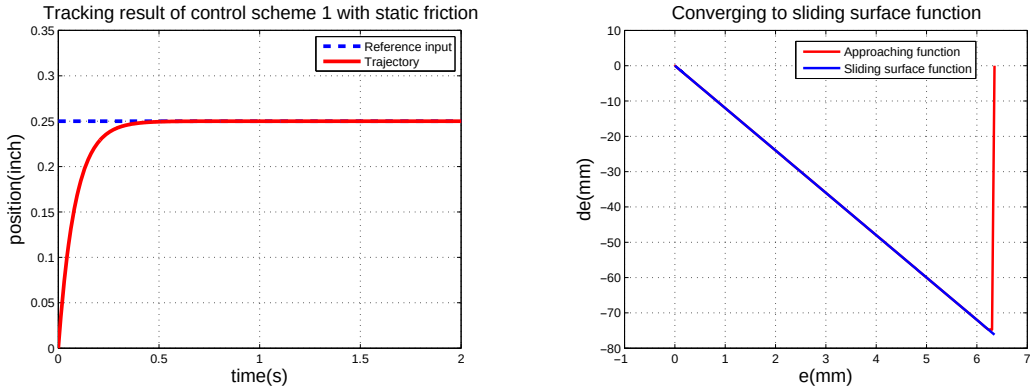

(a)Position tracking with rise time 0.38s (b)Approaching function $\dot{S}_1$

Figure 4.14: Matlab simulation of position tracking plot and sliding surface plot of Scheme 1 for step function $x = 0.25(t)$

4.6.3 Step Function Robustness Tests Simulation Results

4.6.3.1 Viscous Friction Simulation Tests

In order to test the the robustness of the system regarding the uncertainty in measured viscous friction coefficient, we update the viscous coefficient in the state space system model to the new one μ_{v2} while leaving the viscous coefficient in the control loop unchanged, namely μ_v. The simulated position tracking results for step function $x = 1.5(t)$ are shown in Fig. 4.15.

All three algorithms achieve the desired accuracy 0.1 mm with the inaccurate damping ratio. The rise time is 0.54 s, 0.38 s and 0.50 s concerning step function $x = 1.5(t)$. Comparing with the results in which the exact damping ratio is acquired, the rise times increase 0.03 s, 0 s and -0.01 s. It is observed that the performance of Scheme 2 is barely affected by such inaccuracy and hence Scheme 2 is considered a superior option.

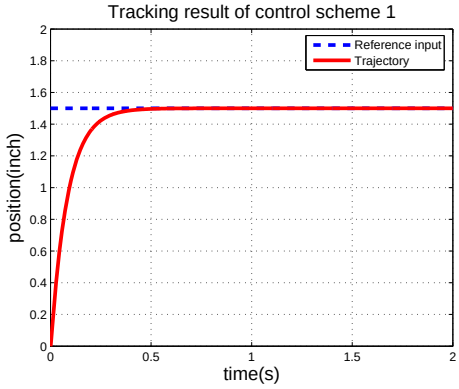

(a)Position tracking with rise time 0.54s

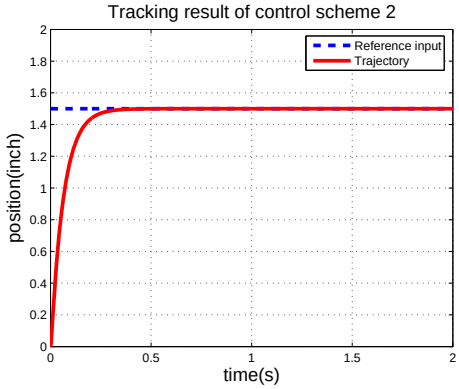

(b)Position tracking with rise time 0.38s

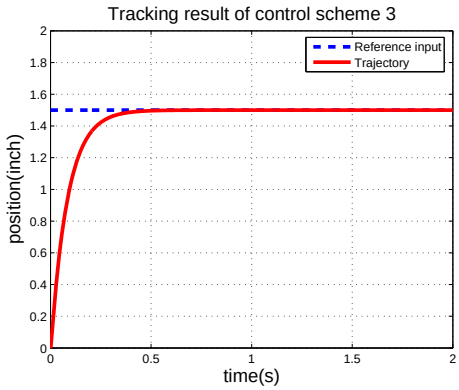

(c)Position tracking with rise time 0.50s

Figure 4.15: Robustness tests of viscous friction for $x = 1.5(t)$

4.6.3.2 External Load Simulation Tests

Since the pneumatic cylinder is intended for various interventional applications, the robustness with regards to external load uncertainties plays a crucial role in control algorithm performance evaluation. Similar to the viscous friction tests, the mass in the state space system model is updated to 0.768 kg while the mass in the control loop is kept at 0.268 kg. The simulated position tracking results for step function $x = 0.25(t)$ are shown in Fig. 4.16 and those for $x = 1.5(t)$ are shown in Fig. 4.17. Figure 4.18 presented the tracking results for $x = 2.75(t)$.

All three algorithms achieve the desired accuracy 0.1 mm with the inaccurate external loads. The rise times are 0.35 s, 0.31 s and 0.34 s with regards to step function $x = 0.25(t)$, are 0.49 s, 0.40 s and 0.51 s with respect to step function $x = 1.5(t)$, are 0.54 s, 0.45 s and 0.56 s for step function $x = 2.75(t)$. Overshoots are observed in Scheme 1 and one case in Scheme 3. Comparing to the results in which the masses of the system are precise, the rise times increase -0.02 s, 0.02 s and -0.01 s for $x = 0.25(t)$, -0.05 s, 0.01 s and 0.01 s for $x = 1.5(t)$, -0.02 s, 0.02 s and -0.01s for $x = 2.75(t)$. Considering the overshoot and the rise time, Scheme 2 is selected as the best among the three.

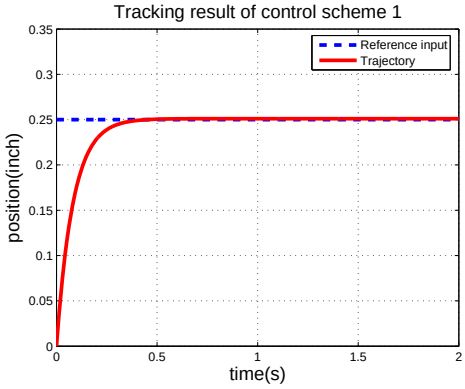

(a)Rise time 0.35s with 0.028mm overshoot

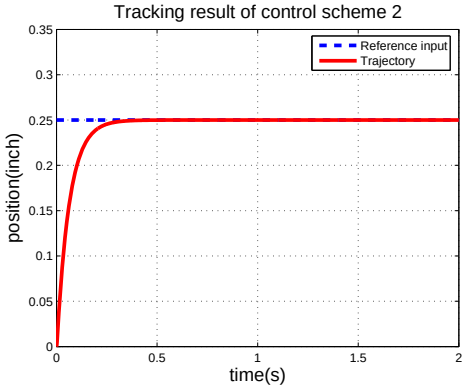

(b)Rise time 0.31s with no overshoot

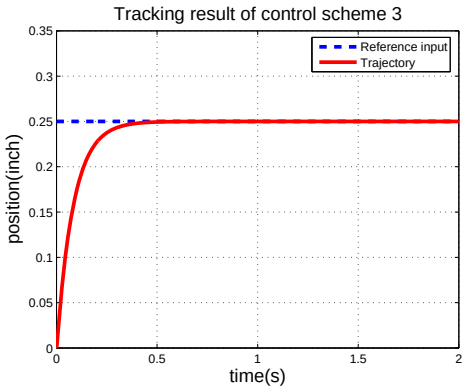

(c)Rise time 0.34s with 0.028mm overshoot

Figure 4.16: Robustness tests of external load for $x = 0.25(t)$

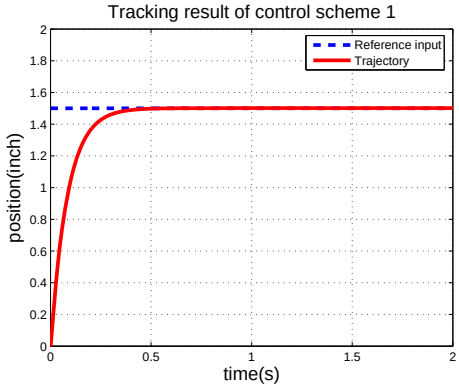

(a)Rise time 0.49s with 0.0254mm overshoot

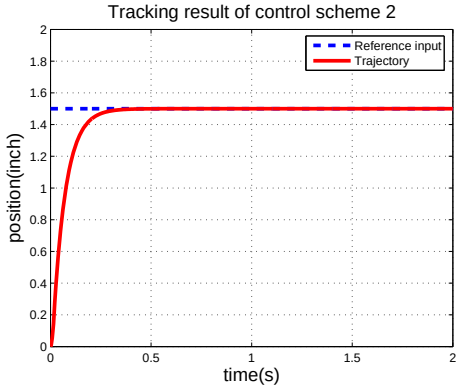

(b)Rise time 0.40s with no overshoot

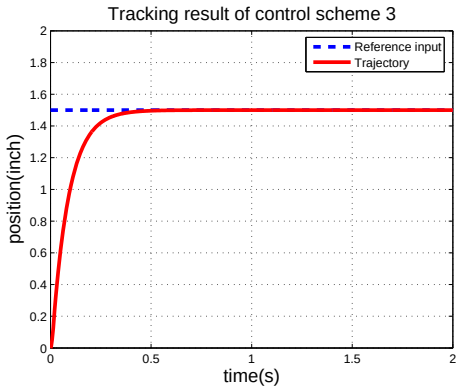

(c)Rise time 0.51s with no overshoot

Figure 4.17: Robustness tests of external load for $x = 1.5(t)$

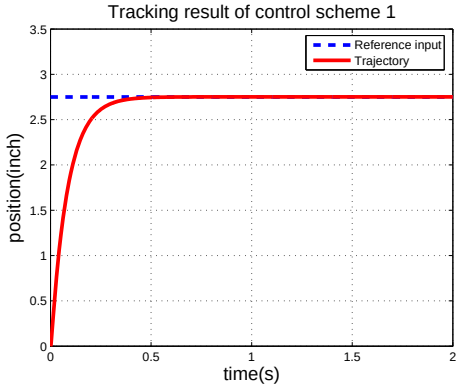

(a)Rise time 0.54s with 0.0254mm overshoot

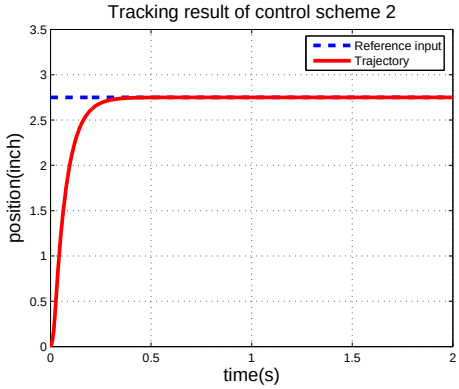

(b)Rise time 0.45s with no overshoot

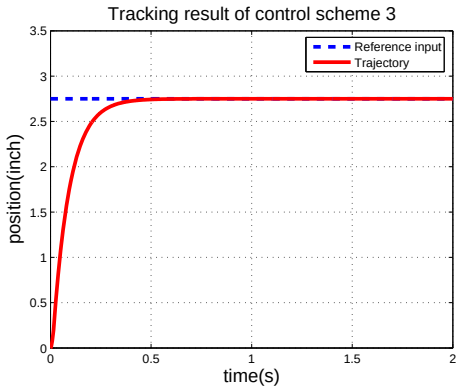

(c)Rise time 0.56s with no overshoot

Figure 4.18: Robustness tests of external load for $x = 2.75(t)$

4.6.4 Sine Function Simulation Results

In addition to set point moves, dynamic trajectory tracking have been simulated in the thesis. The sine wave function $x = 25.4\sin(0.1\pi t) + 29.21$ (mm) is employed as the tracking model. The pneumatic cylinder is commanded to follow its track utilizing the three schemes with the identical parameters listed in Tab. 4.1. The position tracking simulation results are shown in Fig. 4.19. Since the system model presumes that the cylinder always moves and makes no stop, the results presented in Fig. 4.19 are smooth trajectories instead of stair-case like motions in the real world.

All three algorithms achieve RMS of the tracking accuracy of 0.1 mm. The rise times are 0.47 s, 0.35 s, and 0.44 s. However, the results are not as accurate as the set point movements for that the dead band, where the actuation force is no longer sufficient to overcome the static friction and move the cylinder, has more effect on tracking sine wave than static set point position. The sine wave function, while being tracked at 1K Hz, can be regarded as a series of closely scattered set points. Due to the small distance between each point, the control force is limited, which brings the approaching sliding function to enter the dead band frequently. Dead band jeopardize the tracking accuracy. So switching function band width needs to be tune down to ensure satisfactory SSE. However, the narrow band width also bring forth the overshoot or chattering. Thus the real shape of movement should be jigsaw-like.

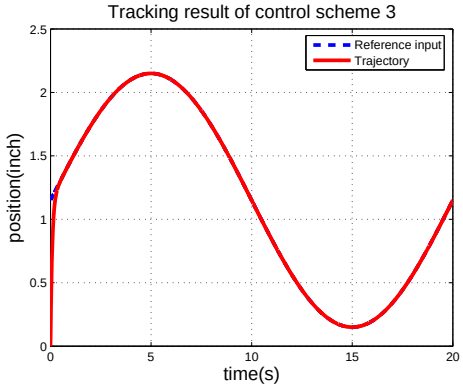

(a)Position tracking with rise time 0.47s

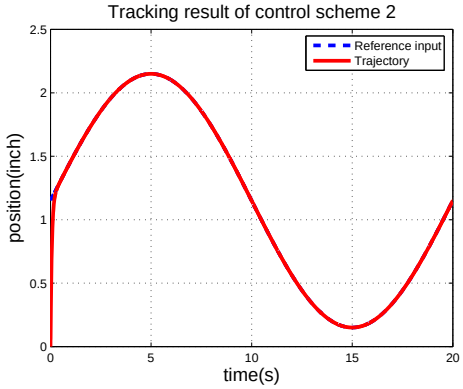

(b)Position tracking with rise time 0.35s

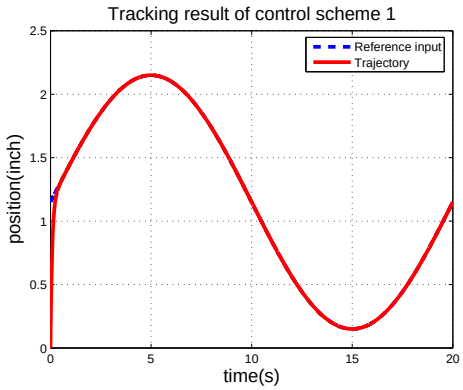

(c)Position tracking with rise time 0.44s

Figure 4.19: Matlab simulation of tracking sine wave function $x = sin(0.1\pi t) + 1.15$ inch

Chapter 5

IMPLEMENTATION IN REAL SYSTEM AND TEST RESULTS

5.1 Implementation in Real System

Discrete time sliding mode control was implemented in control servo board in c language. There were two ways to design the control program, one being running the control loop immediately one after another while recording the time each loop started, the other one being running the control loop at a certain rate, ensuring a constant time interval between each loop. The bowler system framework offered a function, "getms()", to acquire the system time in integer milliseconds form. While the each control loop iteration took less than 1 ms to finish, the calculation based on the "getms()" function would not be accurate and hence compromise the control

precision. Thus the other route was taken. The control function was called in a loop running at 1K Hz. It was done in this way because it could assure that the time interval between each sampling time was precisely 1 ms. In each loop, the position data was read from optical encoder at first. Then the PIC32 calculated the error between the set position and the current position. Subsequently, the sliding surface function S, equivalent control force u_{eq} and switching control force u_{sw} were computed according to the parameters listed in Tab. 4.1. The combined control force u was converted to the control voltage signals, which were converted to the corresponding current signals and then sent to the piezoelectric valves. During each iteration, the position data and other sensor data were sent to the PC via USB and serial ports connection in synchronous mode. Then the data points collected in PC were analyzed by Matlab.

5.2 Real System Test Results

5.2.1 Step Function Test Results

5.2.1.1 Results With No Load Attached

As for Scheme 1, the position tracking results and pressure data of the pneumatic cylinder concerning the three step functions, $x = 0.25(t)$, $x = 1.5(t)$, $x = 2.75(t)$, as well as the sliding surface converge trajectory are presented Fig. 5.1. Similarly, Figure 5.2 shows the the position tracking results, pressure data and the sliding surface converge trajectory concerning the three step functions for Scheme 2. Scheme 3 performance is shown in Fig. 5.3. The evaluation criteria is the steady state position (SS) of the cylinder and the rise time. The measured pressure is the pressure of the chamber in which the piston is actuated. The results are shown in Table 5.1, Table 5.2 and Table 5.3.

	Scheme 1	Scheme 2	Scheme 3
SS (inch)	0.248	0.251	0.2505
Rise time (s)	0.25	0.32	0.19

Table 5.1: Tracking function $x = 0.25(t)$

All three schemes achieved the 0.1 mm (0.004") accuracy requirement. In terms

	Scheme 1	Scheme 2	Scheme 3
SS (inch)	1.497	1.5	1.502
Rise time (s)	0.5	0.38	0.23

Table 5.2: Tracking function $x = 1.5(t)$

	Scheme 1	Scheme 2	Scheme 3
SS (inch)	2.749	2.753	2.753
Rise time (s)	0.43	0.30	0.52

Table 5.3: Tracking function $x = 2.75(t)$

of precision, Scheme 2 is the best among the three. However, the response of Scheme 3 is the fastest. It is also important to note that all the tracking trajectories contains no overshoot, which is requested for safety concerns. This very requirement calls for careful chosen control parameters. Especially when moving over a long distance, overshoot becomes more likely for long time acceleration and high pressure actuation. The precision issue is more likely to show up in small travel range for that the actuation force is kept relatively low. Thus to ensure satisfactory SS, the switching band width d should be selected as small as possible without inducing overshoots.

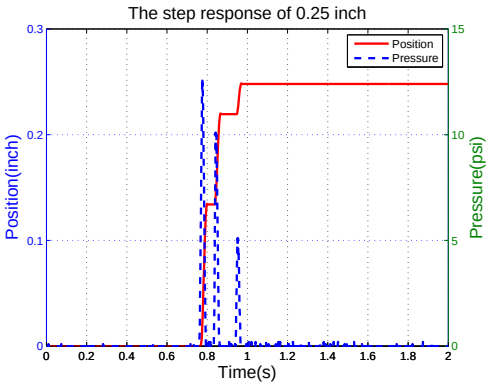

(a)Position tracking with SS 0.248”

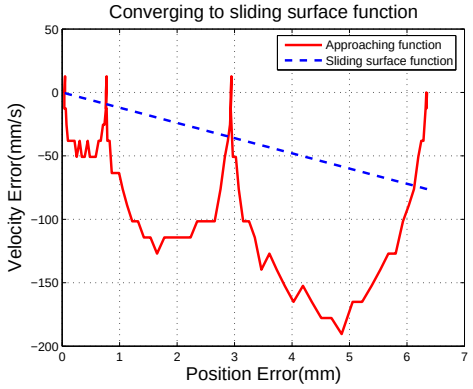

(b) Converging to sliding surface function s=0

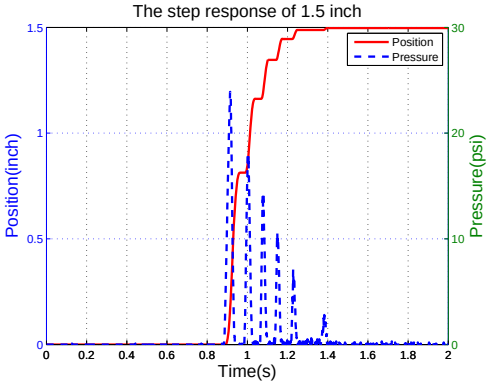

(c)Position tracking with SS 1.497”

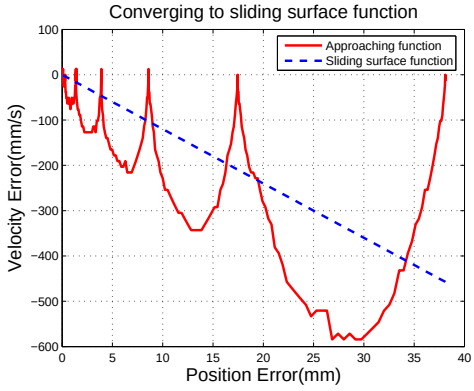

(d) Converging to sliding surface function s=0

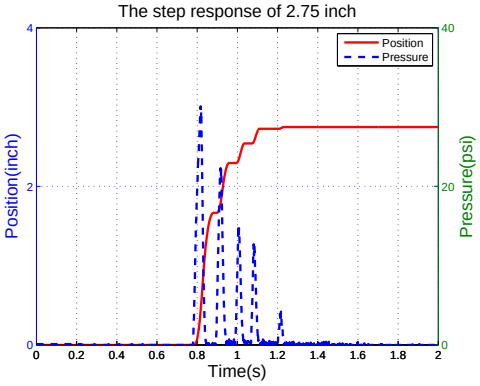

(e)Position tracking with SS 2.749”

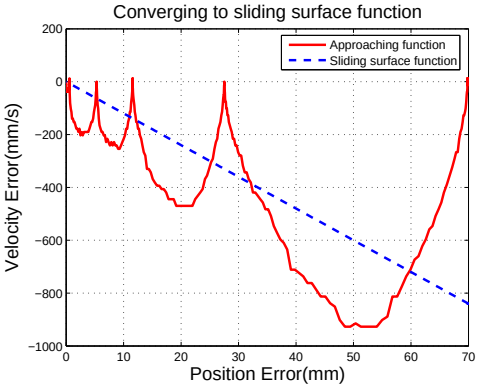

(f) Converging to sliding surface function s=0

Figure 5.1: Step response and pressure of the pneumatic cylinder without load and sliding surface converge trajectory for scheme 1

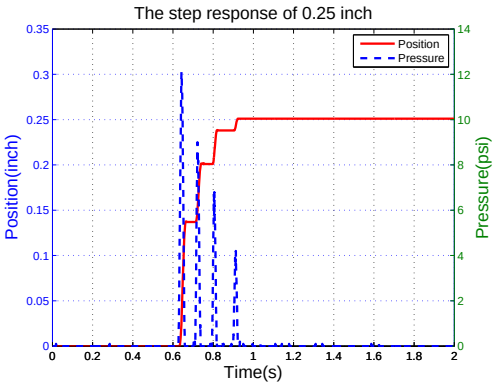

(a)Position tracking with SS 0.251”

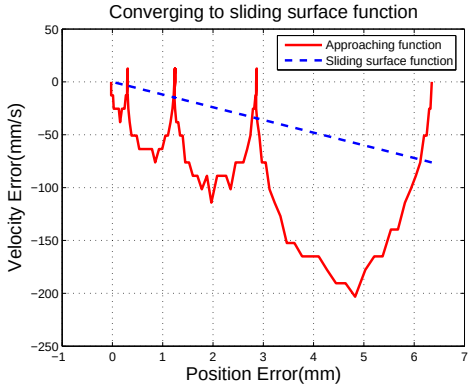

(b) Converging to sliding surface function s=0

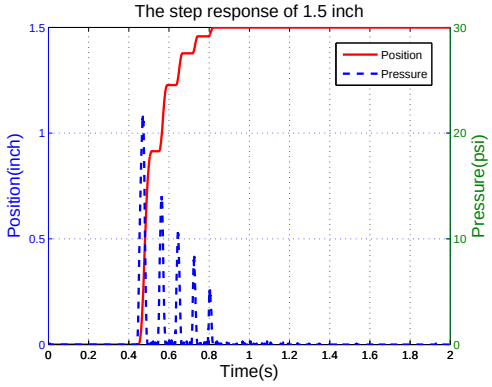

(c)Position tracking with SS 1.5”

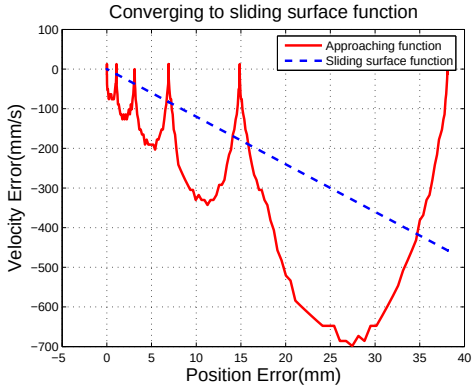

(d) Converging to sliding surface function s=0

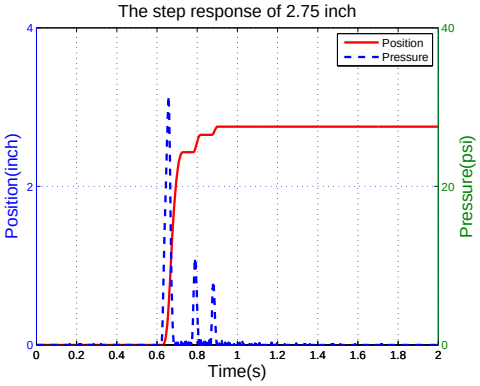

(e)Position tracking with SS 2.753”

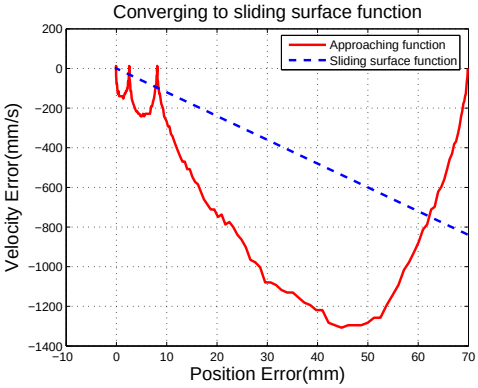

(f) Converging to sliding surface function s=0

Figure 5.2: Step response of and pressure the pneumatic cylinder without load and sliding surface converge trajectory for scheme 2

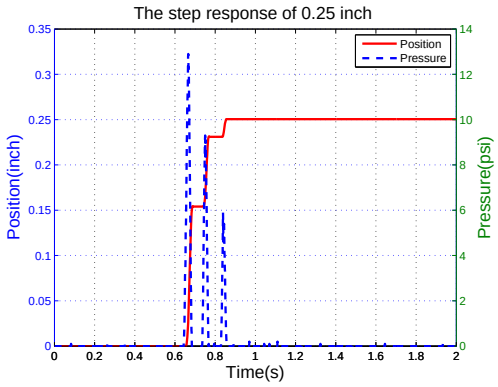

(a)Position tracking with SS 0.2505”

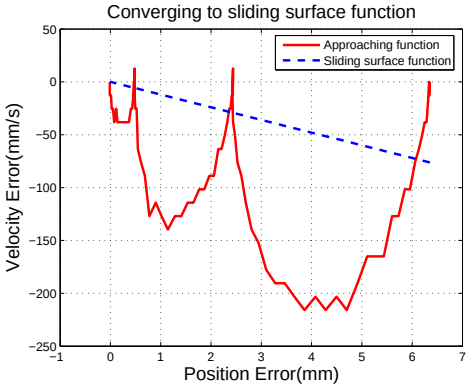

(b) Converging to sliding surface function s=0

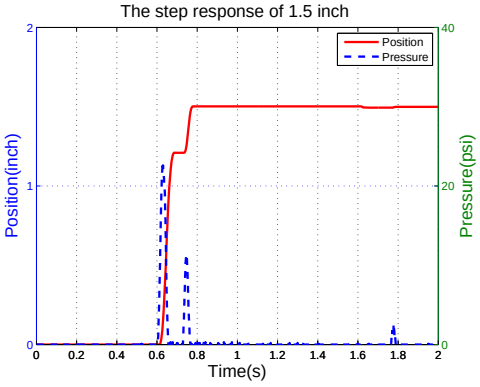

(c)Position tracking with SS 1.502”

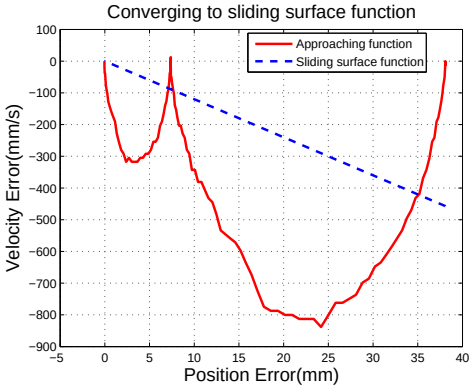

(d) Converging to sliding surface function s=0

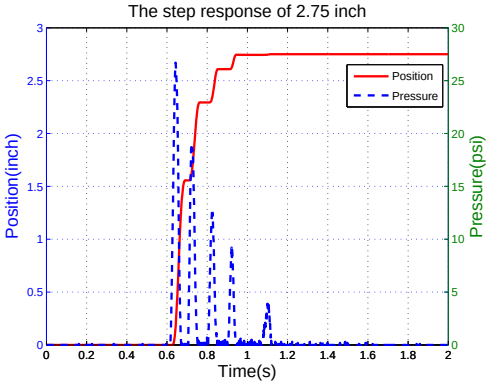

(e)Position tracking with SS 2.753”

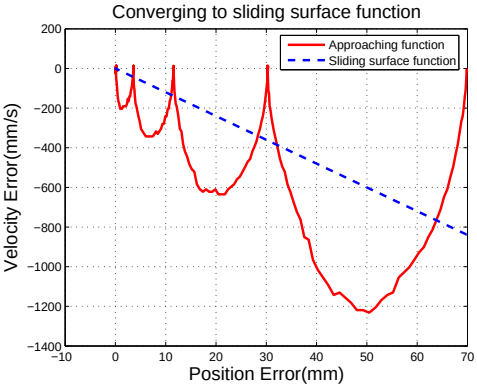

(f) Converging to sliding surface function s=0

Figure 5.3: Step response and pressure of the pneumatic cylinder without load and sliding surface converge trajectory for scheme 3

5.2.1.2 Results With Damper Attached

In real world applications for interventional procedure, the pneumatic cylinder are to be connect to external load with various damping ratio. Hence it is required that the system can still maintain its performance under such condition. In purpose of test the system performance, assuming that the external viscous friction coefficient was already known, a damper with identified damping ratio was attached in parallel with the pneumatic cylinder. Step response and pressure of the pneumatic cylinder are shown in Fig. 5.4, Fig. 5.5 and Fig. 5.6 for each scheme. The results are shown in Table 5.4, Table 5.5 and Table 5.6.

	Scheme 1	Scheme 2	Scheme 3
SS (inch)	0.2475	0.247	0.247
Rise time (s)	0.61	0.31	0.58

Table 5.4: Tracking function $x = 0.25(t)$

All three schemes achieved the 0.1 mm (0.004") accuracy requirement. In terms of precision, Scheme 2 shows the lowest SSE among the three. And the response of Scheme 2 is the swiftest. Comparing to the results in which no damper is added, we can observe that the precision decreased 0.0005", 0 and 0.02" for Scheme 1 and 0.002", 0.003" and -0.002" for Scheme 2 and 0.0025", 0.002" and 0 for Scheme 3.

	Scheme 1	Scheme 2	Scheme 3
SS (inch)	1.497	1.497	1.496
Rise time (s)	0.38	0.37	0.39

Table 5.5: Tracking function $x = 1.5(t)$

	Scheme 1	Scheme 2	Scheme 3
SS (inch)	2.747	2.751	2.753
Rise time (s)	0.53	0.39	0.27

Table 5.6: Tracking function $x = 2.75(t)$

Scheme 1 is better than the other two in terms of maintaining accuracy.

Adding damper to the system was considered beneficial to the performance in [58] because the internal coulomb friction and viscous friction coefficient were kept low. Although a smooth motion could be achieved under such configuration, overshoot and chattering were more likely to appear. Hence the damper could provide extra viscous coefficient to the system model and minimize the unwanted system behaviors. As for the system presented in this thesis, the internal friction was tuned to a relatively high level intentionally to satisfy performance requirements. Hence the addition of a damper to the current system would bring down the accuracy instead of increase it.

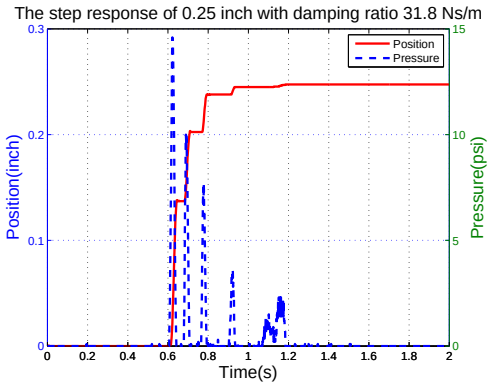

(a)Position tracking with SS 0.2475”

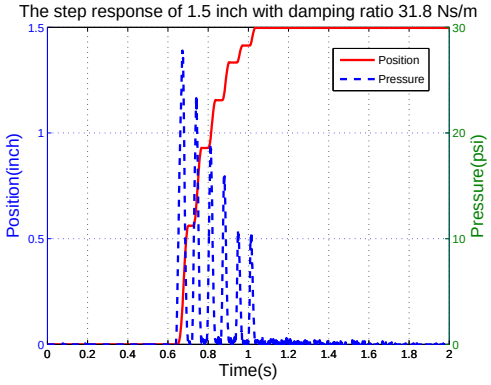

(b)Position tracking with SS 1.497”

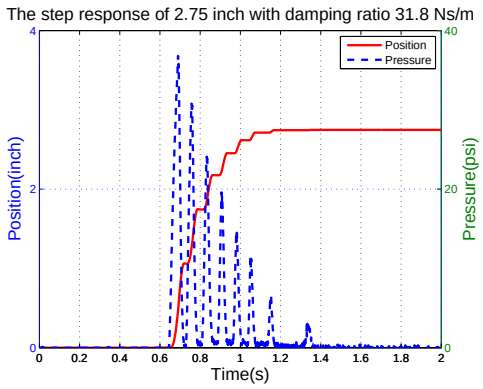

(c)Position tracking with SS 2.747”

Figure 5.4: Step response and pressure of the pneumatic cylinder with damper of damping ratio 31.8Ns/m for scheme 1

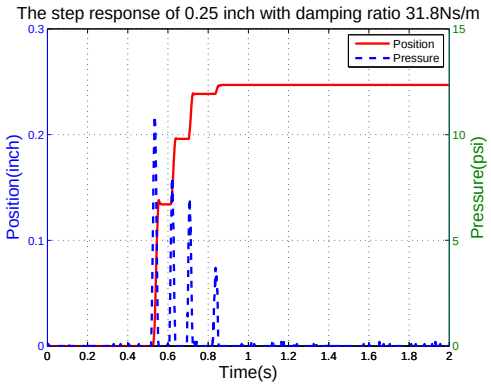

(a)Position tracking with SS 0.247”

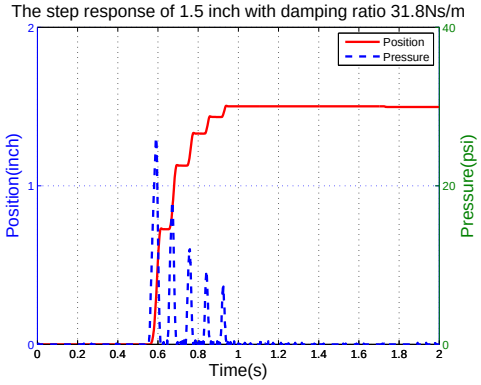

(b)Position tracking with SS 1.497”

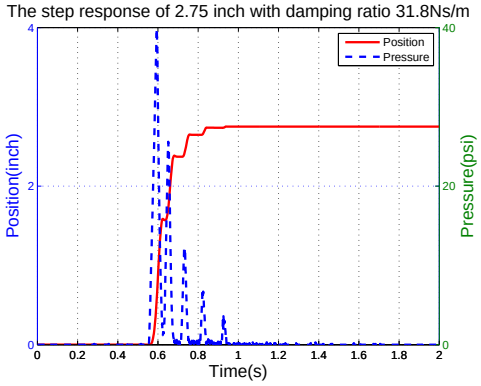

(c)Position tracking with SS 2.751”

Figure 5.5: Step response of the pneumatic cylinder with damper of damping ratio 31.8Ns/m for scheme 2

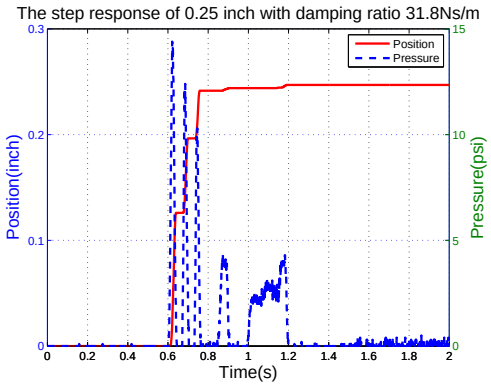

(a)Position tracking with SS 0.247”

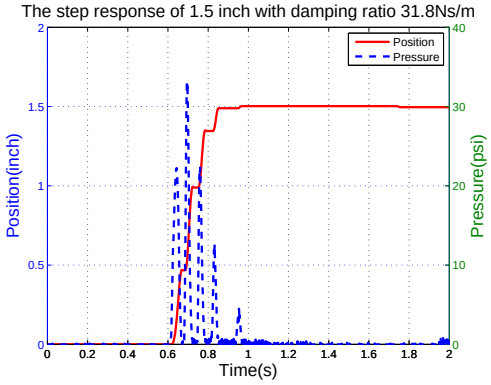

(b)Position tracking with SS 1.496”

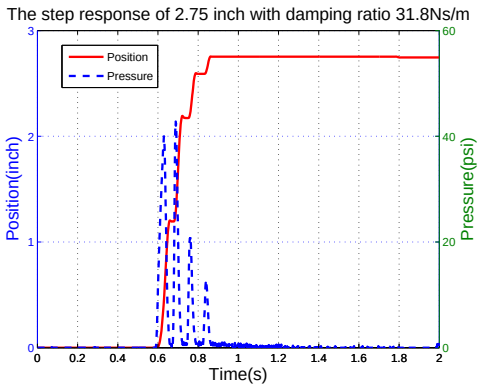

(c)Position tracking with SS 2.753”

Figure 5.6: Step response of the pneumatic cylinder with damper of damping ratio 31.8Ns/m for scheme 3

5.2.1.3 Results With Weight Attached

Similar to the purpose of the adding the damper, the system performance should be evaluated with various external loads. Hence four kinds of weight, namely 50 g, 200 g, 500 g and 1 kg, were employed in the test. We assumed that the mass of external load was known. The performance of Scheme 1 was shown in Fig. 5.7, Fig. 5.8, Fig. 5.9 and Fig. 5.10. The performance of Scheme 2 was shown in Fig. 5.11, Fig. 5.12, Fig. 5.13 and Fig. 5.14. The performance of Scheme 2 was shown in Fig. 5.15, Fig. 5.16, Fig. 5.17 and Fig. 5.18. Each option was tested by tracking step function $x = 0.25(t)$, $x = 2.75(t)$. These two were selected for that the overshoot was more likely shown with large travel range and the low precision was apt to appear in close range motion. Once the performance of the two functions were satisfactory, the performance of the entire travel range was guaranteed. Noted that the parameter k_3 was tuned down to 100, d_3 was tuned up to 0.015 to avoid large shoot that could damage the system.

The SSs for Scheme 1 were 0.25", 2.7465", 0.2515", 2.749", 0.251", 2.751", 0.2385" and 2.74". The SSs for Scheme 2 were 0.2485", 2.747", 0.25", 2.751", 0.251", 2.752", 0.2385" and 2.747". The SSs for Scheme 3 were 0.2495", 2.747", 0.247", 2.75", 0.248", 2.751", 0.2475" and 2.756". The rise times for Scheme 1 were 0.27 s, 0.34 s, 0.13 s, 0.33 s, 0.16 s, 0.38 s, 0.58 s and 1.06 s. The rise times for Scheme 2 were 0.13 s, 0.23 s, 0.7 s, 0.29 s, 0.20 s, 0.45 s, 0.50 s and 1.45 s. The rise times for Scheme 3 were 0.25 s, 0.41 s, 0.63 s, 0.40 s, 0.22 s, 0.87 s, 0.27 s and 0.65 s. Scheme 1 is preferred to the

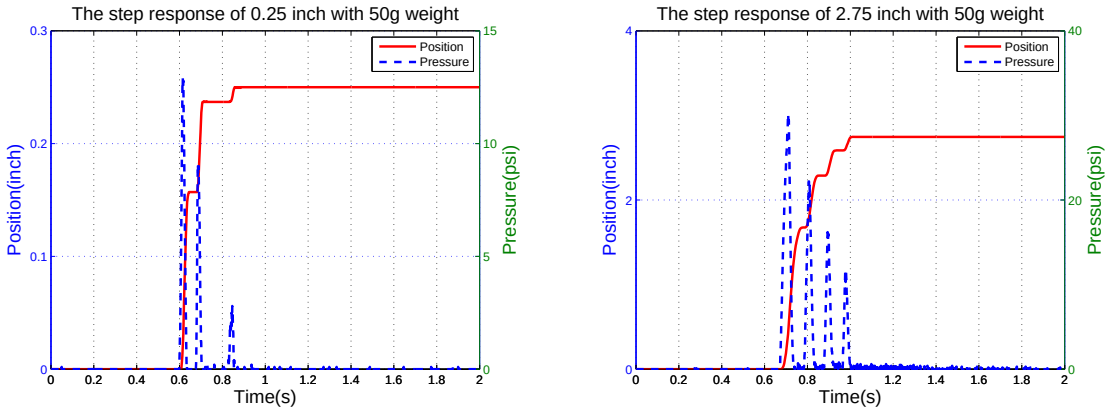

(a)SS 0.25” (b)SS 2.7465”

Figure 5.7: Step response of the pneumatic cylinder with weight 50g for scheme 1

other two for that no overshoot is observed during the test.

The performances of external weight 1 kg added for all three schemes did not meet the requirements, some of which were overshooting and some of which showed SSEs of larger than 0.1 mm. In order to avoid large overshoot, the parameters of the control algorithms were tuned. The rest of the performances were satisfactory. The reason for such poor performances with 1 kg weight is because that the weight placed on the carriage increases the coulomb friction u_c and viscous friction coefficient u_v and hence lead to an inaccurate model such that the SMC can no longer tolerate. We also noted that the influence of weight on rise time is more significant if weight mass is over 500 g.

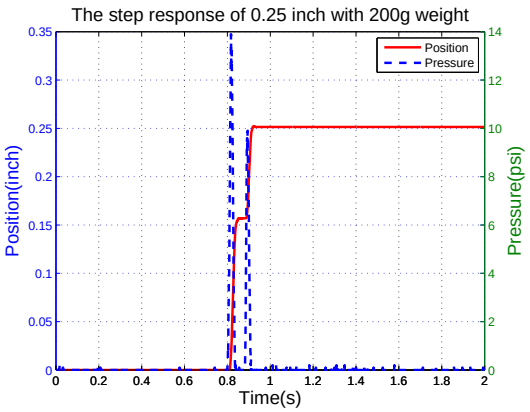

(a)SS 0.2515”

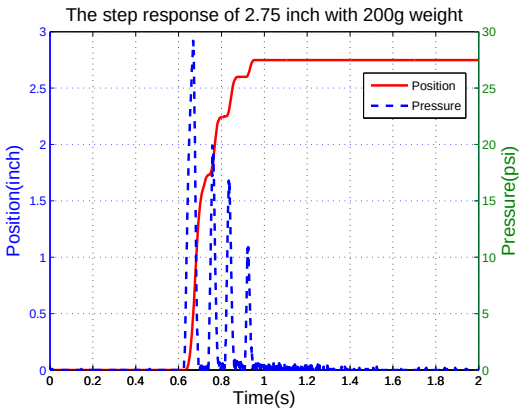

(b)SS 2.749”

Figure 5.8: Step response of the pneumatic cylinder with weight 200g for scheme 1

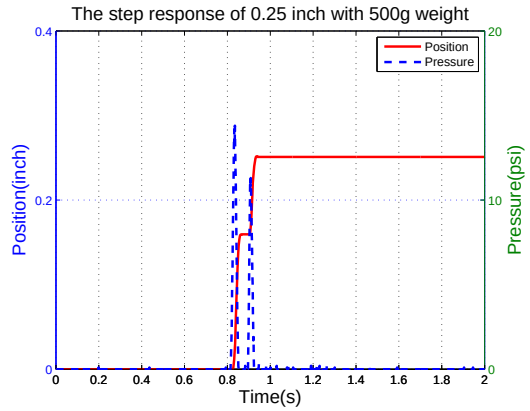

(a)SS 0.251”

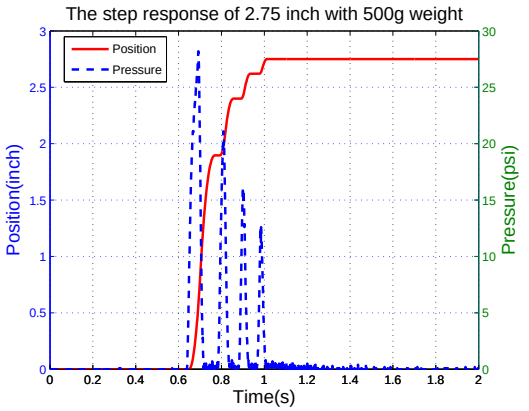

(b)SS 2.751”

Figure 5.9: Step response of the pneumatic cylinder with weight 500g for scheme 1

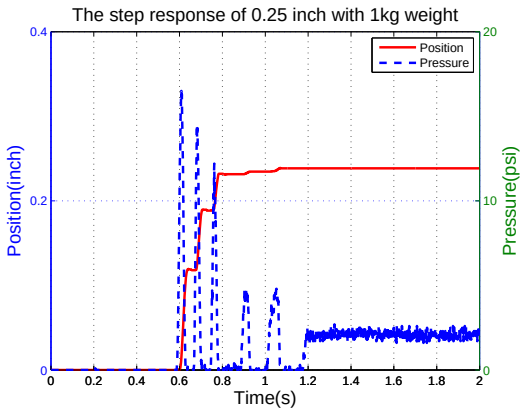

(a)SS 0.2385”

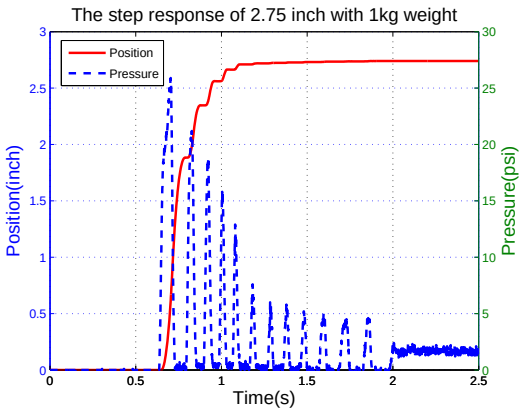

(b)SS 2.74”

Figure 5.10: Step response of the pneumatic cylinder with weight 1kg for scheme 1

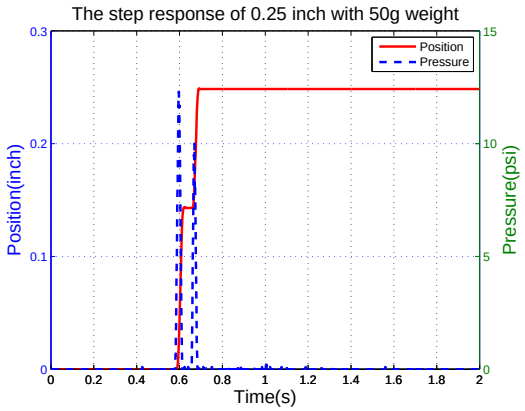

(a)SS 0.2485”

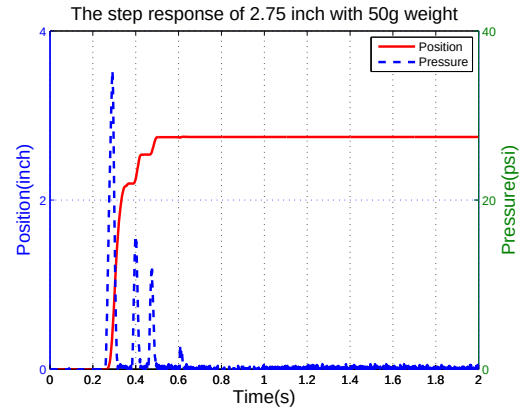

(b)SS 2.747”

Figure 5.11: Step response of the pneumatic cylinder with weight 50g for scheme 2

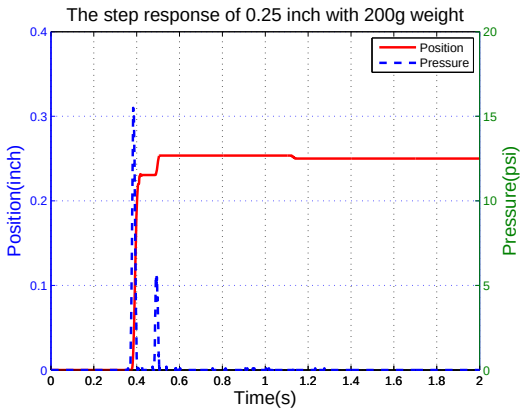

(a)SS 0.25”

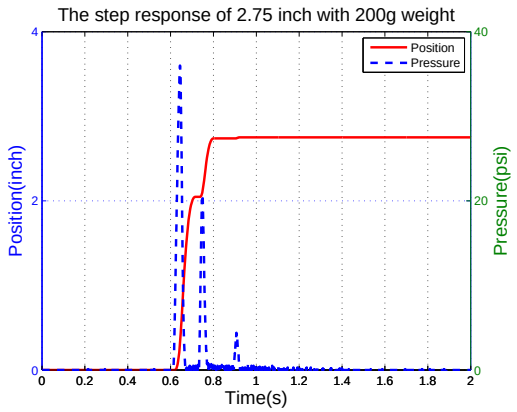

(b)SS 2.751”

Figure 5.12: Step response of the pneumatic cylinder with weight 200g for scheme 2

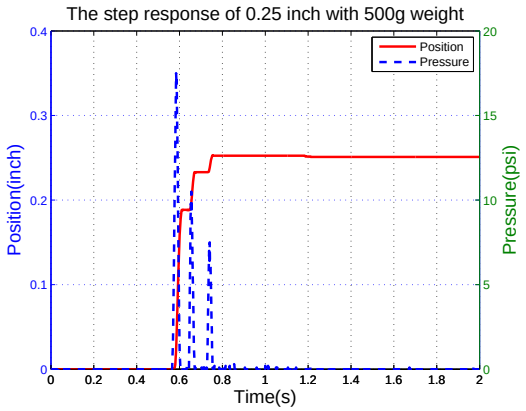

(a)SS 0.251”

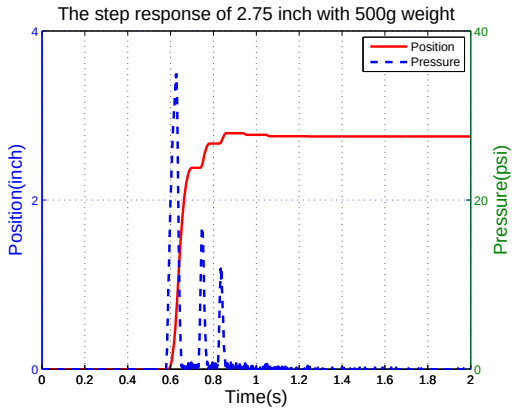

(b)SS 2.752”

Figure 5.13: Step response of the pneumatic cylinder with weight 500g for scheme 2

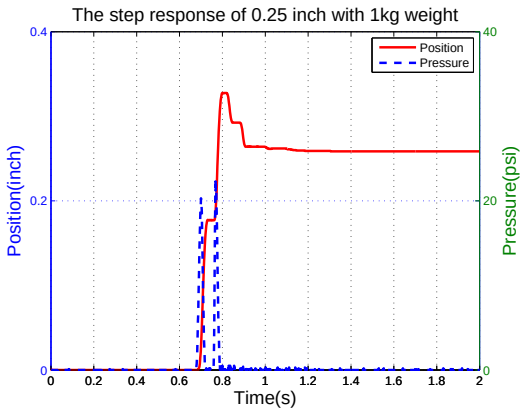

(a)SS 0.2385”

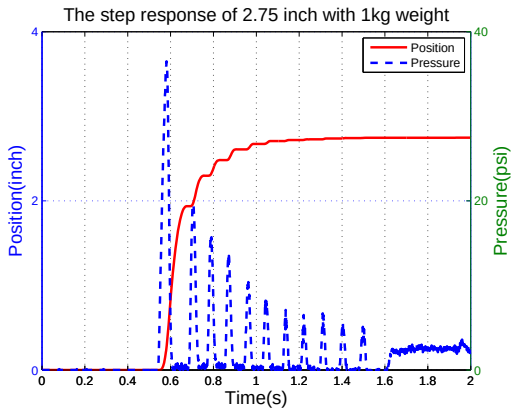

(b)SS 2.747”

Figure 5.14: Step response of the pneumatic cylinder with weight 1kg for scheme 2

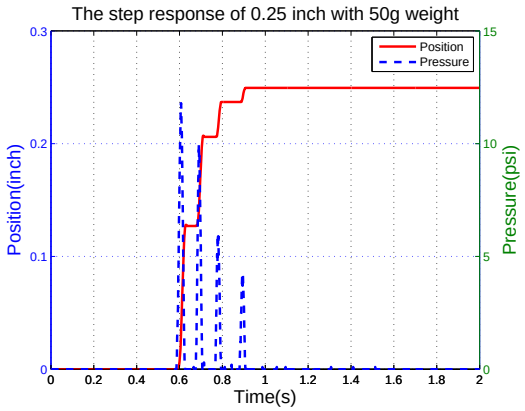

(a)SS 0.2495”

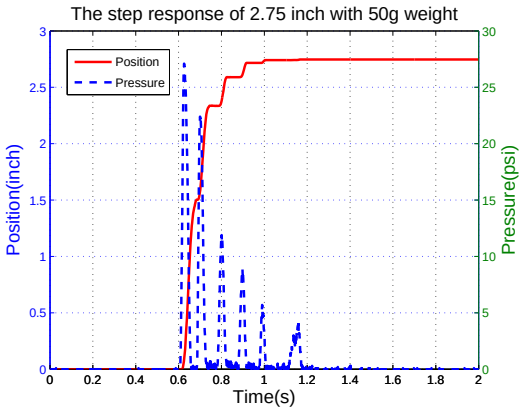

(b)SS 2.747”

Figure 5.15: Step response of the pneumatic cylinder with weight 50g for scheme 3

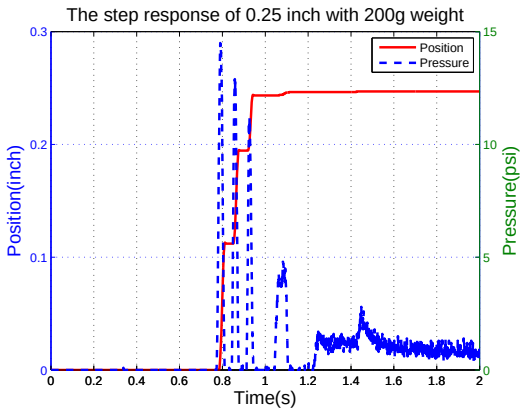

(a)SS 0.247”

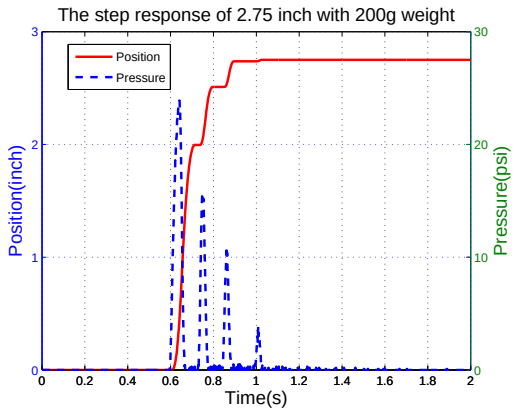

(b)SS 2.75”

Figure 5.16: Step response of the pneumatic cylinder with weight 200g for scheme 3

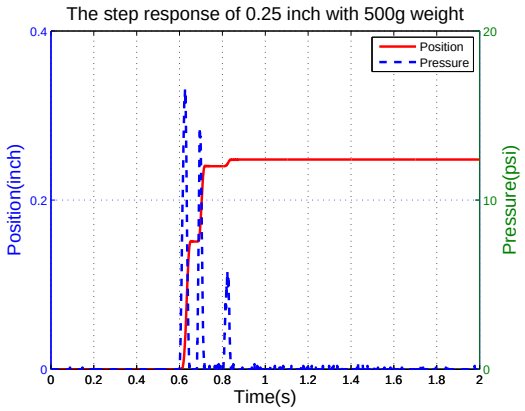

(a)SS 0.248”

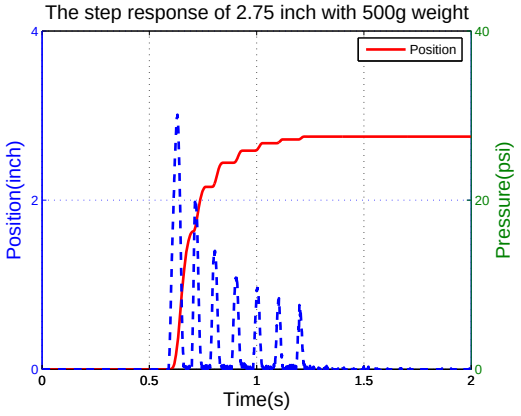

(b)SS 2.751”

Figure 5.17: Step response of the pneumatic cylinder with weight 500g for scheme 3

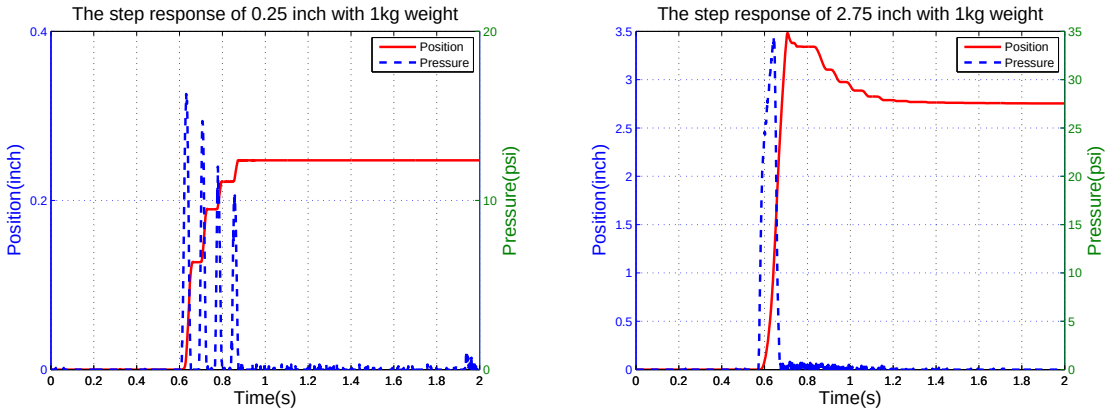

(a)SS 0.2475” (b)SS 2.756”

Figure 5.18: Step response of the pneumatic cylinder with weight 1kg for scheme 3

5.2.2 Step Function Robustness Tests

5.2.2.1 Viscous Friction Robustness Tests

The viscous friction coefficient of the external load is not always known or accurate. Thus testing the the robustness of the system regarding the uncertainty in estimated or measured viscous friction coefficient is necessary. We connected the damper to cylinder while leaving the viscous coefficient in the control loop unchanged, namely μ_v. All three step functions, $x = 0.25(t)$, $x = 1.5(t)$, $x = 2.75(t)$, were selected as the tracking trajectories. The position tracking results for Scheme 1 are shown in Fig. 5.19. Figure 5.20 and Fig. 5.21 show the position tracking trajectories for Scheme 2 and Scheme 3 respectively. The results are shown in Table 5.7, Table 5.8 and Table 5.9.

	Scheme 1	Scheme 2	Scheme 3
SS (inch)	0.2465	0.248	0.2465
Rise time (s)	0.18	0.24	0.48

Table 5.7: Tracking function $x = 0.25(t)$

The tracking result of $x = 1.5(t)$ showed overshoot of 0.012" for scheme 3. We can observe that the response of Scheme 3 is faster than the other two. Comparing the result with the ones in which the external damping ratio is known, the SSs decrease

	Scheme 1	Scheme 2	Scheme 3
SS (inch)	1.496	1.498	1.5
Rise time (s)	0.6	0.35	0.3

Table 5.8: Tracking function $x = 1.5(t)$

	Scheme 1	Scheme 2	Scheme 3
SS (inch)	2.745	2.748	2.751
Rise time (s)	0.72	0.39	0.36

Table 5.9: Tracking function $x = 2.75(t)$

0.001”, 0.001” and 0.002” for Scheme 1 and -0.001”, -0.001”, 0.001” for Scheme 2 and 0.0005”, -0.004” and -0.002” for Scheme 3. Hence we can conclude that Scheme 3 is more robust than the other two concerning viscous friction coefficient uncertainty.

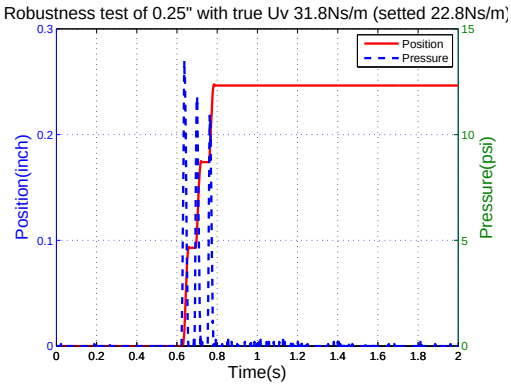

(a)

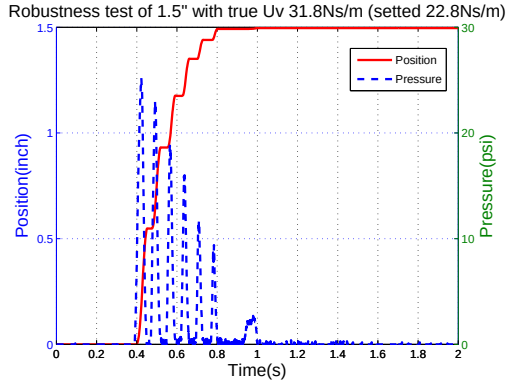

(b)

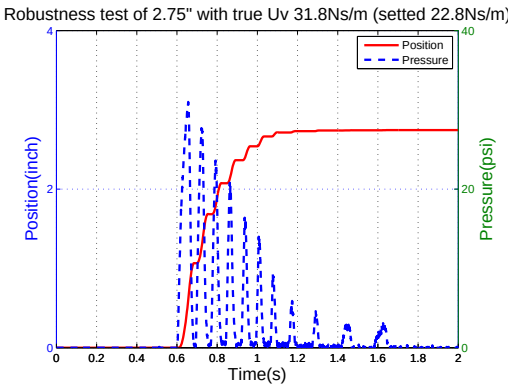

(c)

Figure 5.19: Robustness test of step response with viscous friction coefficient 31.8Ns/m (22.8Ns/m in control loop) for scheme 1

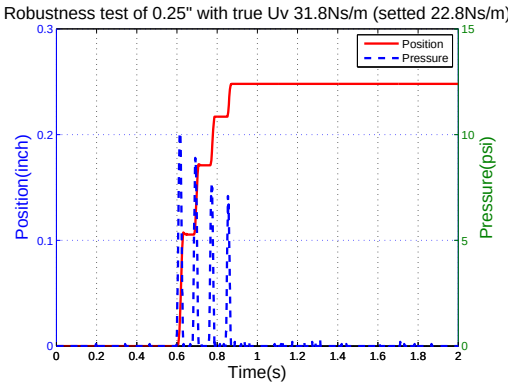

(a)

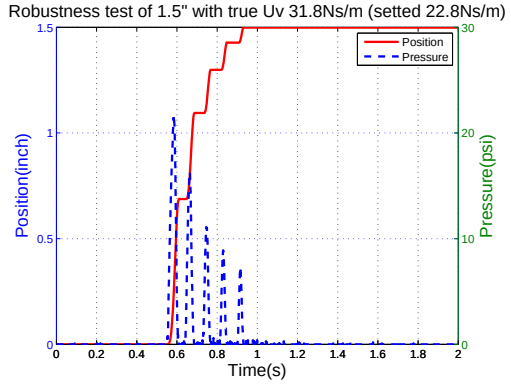

(b)

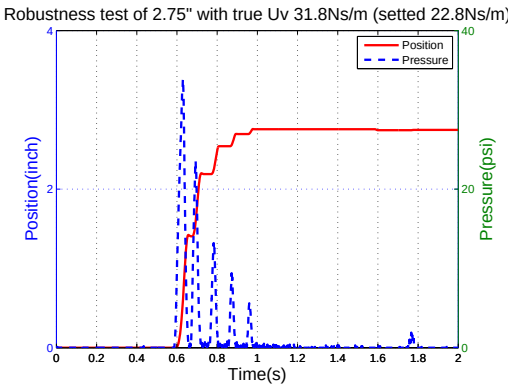

(c)

Figure 5.20: Robustness test of step response with viscous friction coefficient 31.8Ns/m (22.8Ns/m in control loop) for scheme 2

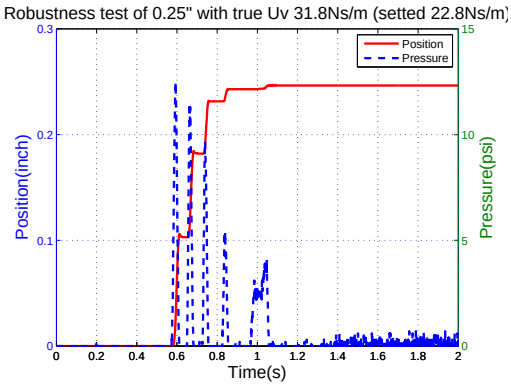

(a)

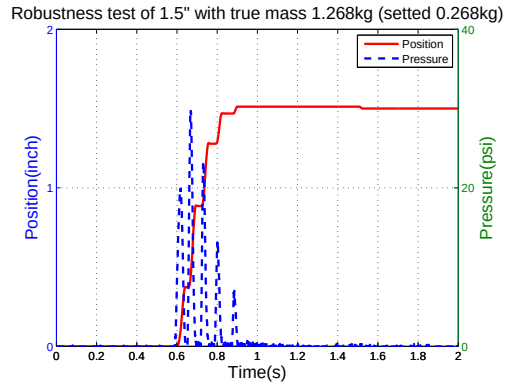

(b)

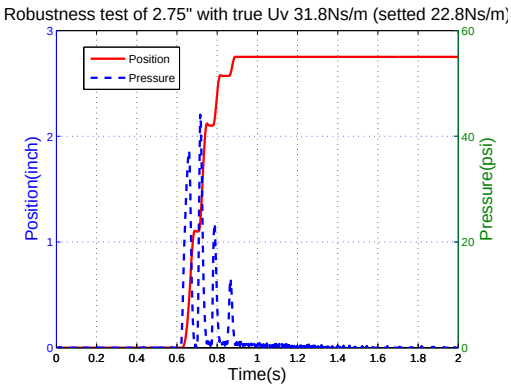

(c)

Figure 5.21: Robustness test of step response with viscous friction coefficient 31.8Ns/m (22.8Ns/m in control loop) for scheme 3

5.2.2.2 External Load Robustness Tests

Similar to the viscous friction robustness tests, our knowledge of mass of the external load is sometimes inaccurate. One of the three weights, namely 0.1 kg, 0.5 kg, 1 kg, was added onto the carriage while the mass in the control loop is kept at 0.268 kg. Step function $x = 1.5(t)$ was selected as the tracking function. The position tracking trajectories for Scheme 1 are shown in Fig. 5.22 and those for Scheme 2 are shown in Fig. 5.23. Figure 5.24 presented the tracking trajectories for Scheme 3. The results are shown in Table 5.10, Table 5.11 and Table 5.12.

	Scheme 1	Scheme 2	Scheme 3
SS (inch)	1.499	1.497	1.502
Rise time (s)	0.72	0.21	0.25

Table 5.10: Tracking function $x = 1.5(t)$ with load 0.1 kg

	Scheme 1	Scheme 2	Scheme 3
SS (inch)	1.502	1.502	1.497
Rise time (s)	1.35	0.75	0.51

Table 5.11: Tracking function $x = 1.5(t)$ with load 0.5 kg

	Scheme 1	Scheme 2	Scheme 3
SS (inch)	1.494	1.5	1.494
Rise time (s)	0.54	0.38	0.53

Table 5.12: Tracking function $x = 1.5(t)$ with load 1 kg

Only Scheme 3 showed no overshoot for all three load masses. Also we can observe that the response of Scheme 3 is the fastest among all three schemes. Therefore we come to the conclusion that Scheme 3 is more robust than the other two schemes in terms of external load mass uncertainty.

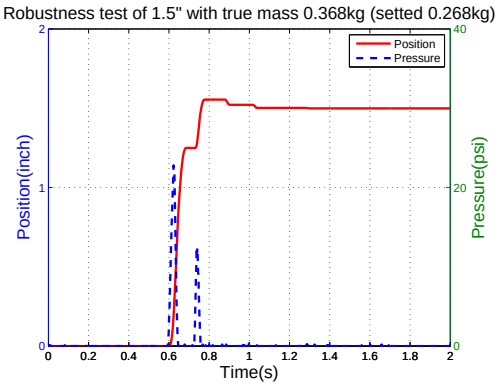

(a)SS 1.499” with 0.054” overshoot

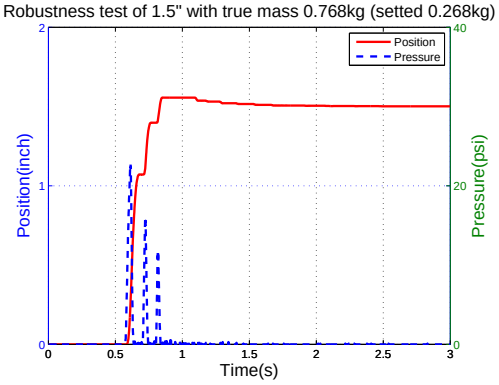

(b)SS 1.502” with 0.056” overshoot

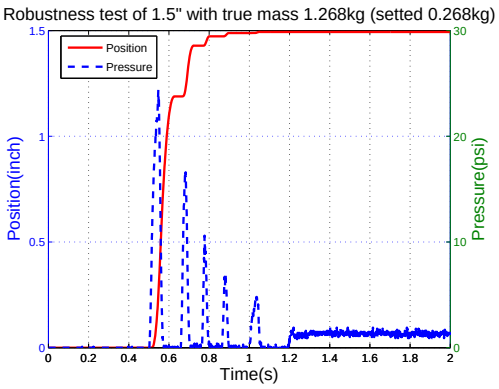

(c)SS 1.494” with no overshoot

Figure 5.22: Robustness tests of external load for Scheme 1

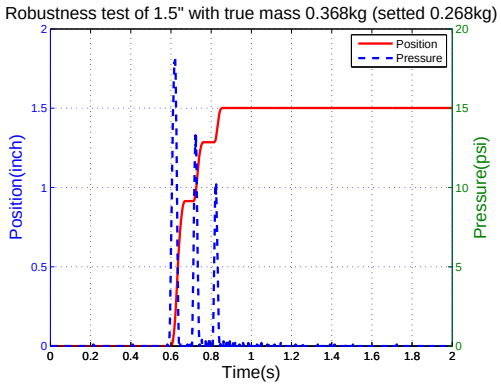

(a)SS 1.502” with no overshoot

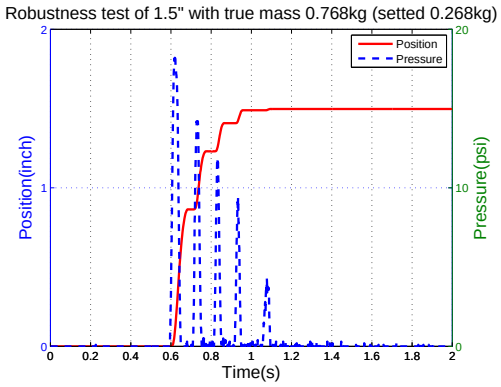

(b)SS 1.497” with no overshoot

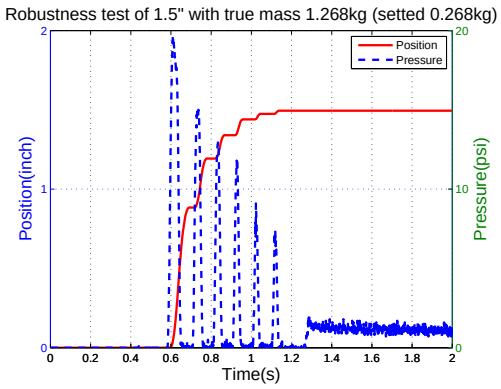

(c)SS 1.494” with no overshoot

Figure 5.24: Robustness tests of external load for Scheme 3

5.2.3 Sine Function Tracking Results

Dynamic trajectory tracking is also of importance in control algorithm evaluation since that such motion is require of brachytherapy. The sine wave function $x = 25.4\sin(0.1\pi t) + 29.21$ (mm) or $x = sin(0.1\pi t) + 1.15$ (inch) is selected as the tracking model. Parameters listed in Tab. 4.1 is suitable for static point-to-point motion. However, the dynamic performance with those parameters were not satisfactory. Thus control parameters were re-tuned for a better tracking performance. The re-tuned parameters are shown in Tab. 5.13. The position tracking trajectories are shown in Fig. 5.25, Fig. 5.26 and Fig. 5.27 . The results are shown in Table 5.14.

λ_1	8.5	k_1	29	d_1	0.013
λ_2	16	k_2	112	d_2	0.01
λ_3	12	k_3	95	d_3	0.01
a	0.1	ζ	75		

Table 5.13: The re-tuned parameters of SMCr for tracking sine function

The reason why the motion trajectory presented resembles a jig-saw shape is discuss in the pervious Chapter. Judged by RMS and rise time, Scheme 2 outperformed the other two, indicating better dynamic tracking capability.

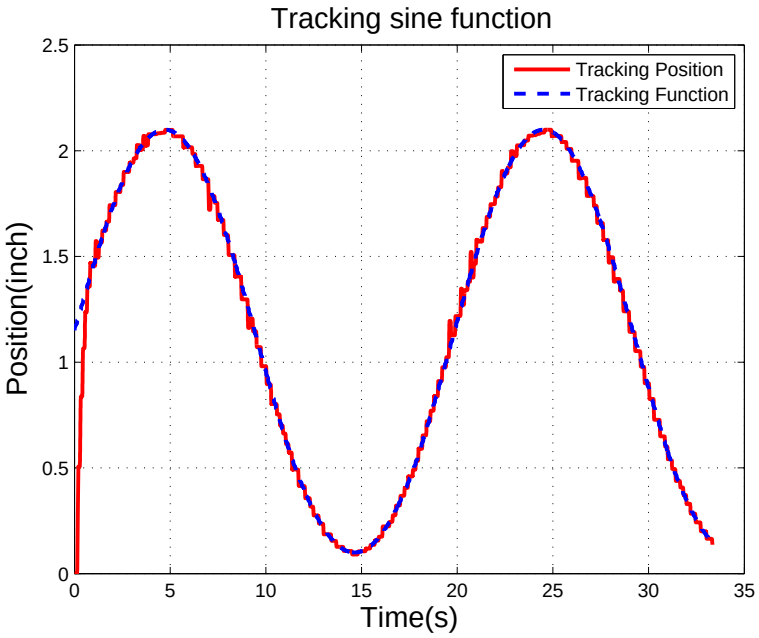

Figure 5.25: Tracking sine wave function $x = sin(0.1\pi t) + 1.15$ inch for Scheme 1

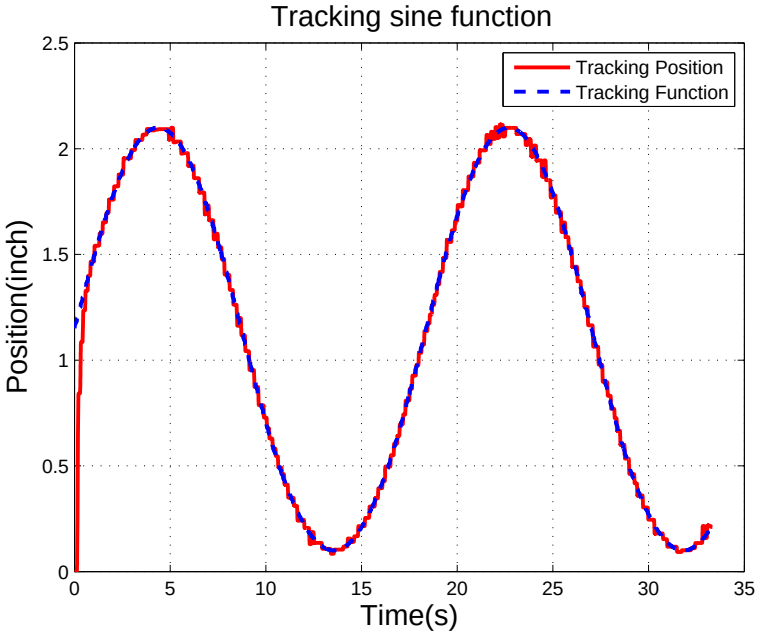

Figure 5.26: Tracking sine wave function $x = sin(0.1\pi t) + 1.15$ inch for Scheme 2

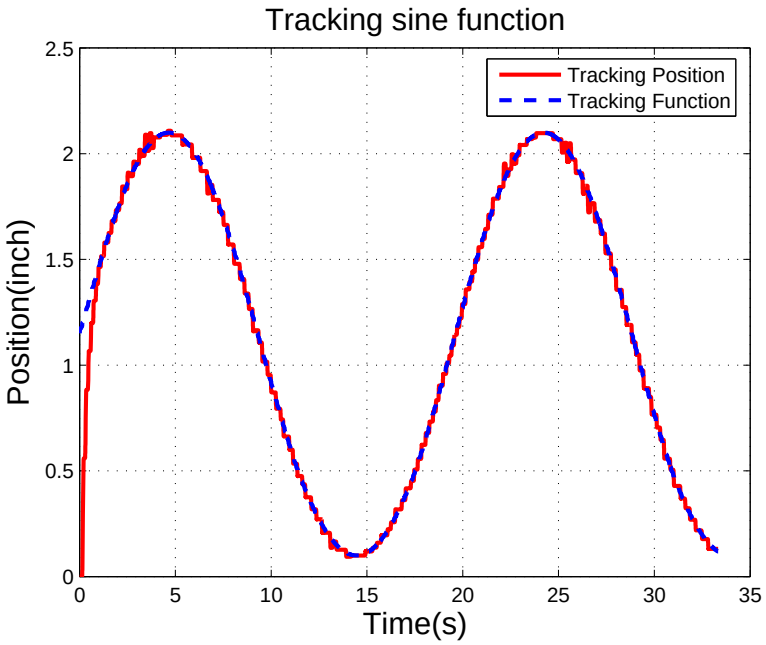

Figure 5.27: Tracking sine wave function $x = sin(0.1\pi t) + 1.15$ inch for Scheme 3

	Scheme 1	Scheme 2	Scheme 3
RMS (mm)	0.38	0.334	0.356
Rise time (s)	0.5	0.4	0.8

Table 5.14: Tracking function $x = sin(0.1\pi t) + 1.15$ inch

5.3 Discussion

Tuning parameters of SMCr is crucial in determining system performance. Thus understanding of the effect of each parameter is important. As for Scheme 1, there are three parameters, λ_1 , k_1 and d_1. Basically, λ_1 affects the approaching speed when the approaching function enters the switching band zone, where the switching control signal rapidly reduce to a small amount. Tuning up λ_1 will increase the equivalent control signal, even in the switching band zone. Thus pushing the approaching slide function to converge towards the sliding surface faster. However, too fast speed will bring the approaching function to travel across the sliding surface instead of converging, introducing overshoot and chattering. On the other hand, tuning down λ_1 will increase system response time and reduce chattering. k_1 is the parameter which mostly determines magnitude of the control signal outside the switching band. Among the three schemes proposed in this thesis, the same saturation function is employed as the switching function. The magnitude of sat() is 1 when outside the switching band. Thus the value of switching control signal is constant beyond the band. As long as the error between the desired position and current position is not large, switching control signal is larger than equivalent control signal and hence k_1 determine the tracking speed of the system. d_1 determines the switching band width. It is directly affecting the SSE of the system tracking. Within the switching band, the control signal quickly decreases to such an extent that the coulomb friction and viscous friction finally slow down the system to a stop. Thus we want the point where

it stops to be as close to our desired position as possible. Naturally, tuning down d_1 will increase the tracking accuracy. However, too small a band width will not be able to provide a sufficient distance for approaching function to converge to the sliding surface, inducing overshoot and chattering. For long distance travel, the system will be accelerated to a certain speed when d_1 should be large to provide ample space for the state to converge. Another way of dealing with large travel range is to increase the coulomb friction and viscous friction. Despite of fast response and smooth motion , it it often observed that a well-lubricated system is hard to control precisely. One often has to trade between response speed, accuracy and smoothness of motion. As for Scheme 2, λ_2, k_2 and d_2 works similarly as the corresponding parameters in Scheme 1. a works as an boost when the system starts far away from the sliding surface function and hence increasing response speed. One should keep a small because it is an exponential function. As for Scheme 3, λ_3, k_3 and d_3 are analogous to λ_1 , k_1 and d_1. Comparing Fig. 5.18 and Fig. 5.24 (c), we can observe that smaller k_3 and larger d_3 in Fig. 5.18 decrease the tracking accuracy. ζ is used to increase the converge speed when the approaching sliding function enters the switching band zone.

The difference between Matlab simulation results and the real test results lies in two parts: one being the system modeling and the other being identified system parameter. As we discussed in the previous chapter, the system model for simulation is the same for both dynamic and static. In such case, the dead-band effect induced by static friction is not obvious. However, the physical test results shows otherwise.

The system parameter identified assumes the parameters are homogeneous through out the entire travel range. The real test demonstrates that the friction where the piston is close to the back cap is larger than that where the piston is close to the front cap. Also the friction for each travel may be different due to the wear of rubber sealing ring. It is also observed that the friction is different between moving forward and moving backward. Still the simulation presented a quantitative way of comparing the performance among the three control schemes.

Finally, we can come to an conclusion for the control algorithms evaluation. Scheme 2 is the most accurate control scheme with fastest response. However, the scheme is "vulnerable" to uncertainty and error of the system model. Sometimes large overshoot and chattering may occur when estimated external load is too inaccurate for the scheme to compensate. Also the computation complexity of Scheme 2 is the most substantial one among the three. Scheme 3 is the most robust algorithm to the system modeling and external load uncertainty. The accuracy and the response speed is better than Scheme 1. Scheme 1 is the most fundamental sliding mode control algorithm. The computation load of Scheme 1 is the least among the three. By careful modeling and tuning, one can still attain a satisfactory performance via Scheme 1.

Chapter 6

DEVELOPMENT OF MRI-COMPATIBLE PNEUMATIC CYLINDER LOCK DEVICE

6.1 Motivation and Goals

The pneumatic cylinder should be rigidly fixed once attained the desired position for safety concerns. Thus a lock device is required to hold the cylinder brass rod in position and to prevent any movements of the rod brought by disturbances.

Due to the utilization of metallic components, traditional lock devices are not

desirable for this application. Pneumatic actuation is preferred as the braking power for its intrinsic MRI-compatibility and convenient accessibility in MRI room. A MRI-compatible pneumatic lock device was developed by Fischer [58]. The compactness of the device facilitates easy integration with the MRI-compatible pneumatic cylinder. However, additional unwanted friction is introduced to the system since that the brake surface contacts the cylinder rod even no braking is applied. The MRI-compatible pneumatic cylinder lock device presented here has several significant advantages over the previously developed device.

6.2 Lock Design

Several adopted design requirements are listed below:

1. The lock device must be MRI-compatible. Since the device is to be placed close to the scanner bore, non-metallic material is preferred.

2. The device should be independently controlled by an on-off switch valve so that the device is able to act as a stand-alone component with respect to the two-piezoelectric-valves-controlled pneumatic cylinder.

3. No friction should be added to the cylinder brass rod once unlocked.

4. The components should be designed such that they can be rapidly fabricated via laser cutter, rapid prototyping machine and so on.

5. The material and the off-the-shelf product employed in the device should be low-cost.

6. The lock device can function without any tendency to deviate the cylinder brass rod.

7. The mechanism design should be kept simple unless necessary.

8. The device can be compliant to cylinder brass rods with various diameters.

6.2.1 Mechanism Design

In order to utilize the compress air supply as the braking power, pneumatic actuation is chosen as the actuation technique. The goal is to control one or multiple

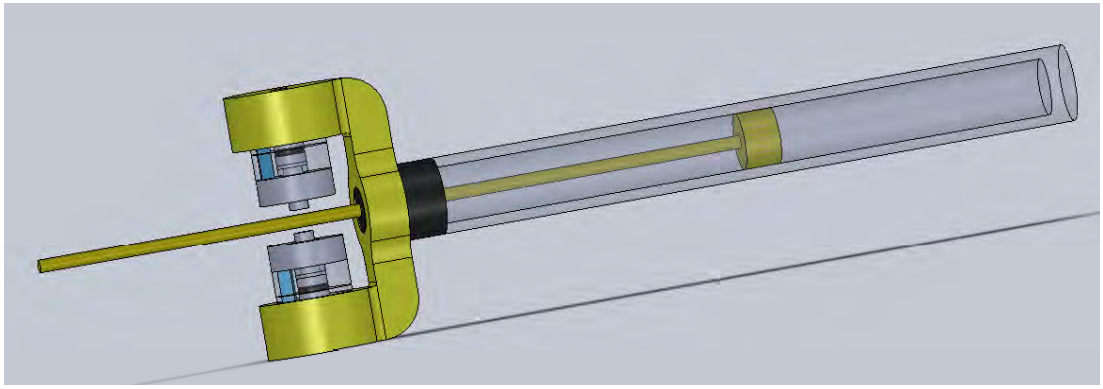

Figure 6.1: The mechanical structure of the MRI-compatible pneumatic cylinder lock device

pneumatic actuators with one independently controlled on-off switch or one piezoelectric pressure regulating valve. The braking force should be applied perpendicular to the cylinder brass rod so as to avoid any additional friction when unlocked and to ensure small travel range so as to maintain compactness of the device. In order to avoid deviation of the cylinder brass rod, braking force should be applied from two opposite directions to the same point position simultaneously. There are several routes to attain this goal, such as gear transmission, timing belt transmission and so on. However, such design will not keep the compactness and will increase the complexity in fabrication. Thus I choose two identical pneumatic cylinders placing face to face, controlled by one piezoelectric valve. And the brass rod is positioned in between the pneumatic cylinders. The 3D model of the MRI-compatible pneumatic cylinder lock device is shown in Fig. 6.1.

The pneumatic cylinder employed in the lock device is designed to provide direct

braking force to the brass rod. Since the direction of the pneumatic cylinder movement is perpendicular to the direction of the brass rod movement, small travel range of the pneumatic cylinder can be achieved without inducing friction and hence the size of the pneumatic cylinder can be made compact. The pneumatic cylinder is actuated by the compressed air via air inlet on the back cap of the actuator. A seal ring is fixed between two pistons. An equivalent spring is placed next to the front cap in the front chamber such that the piston is pushed backwards when no longer actuated. Several holes are cut through the front cap so as to keep the pressure of the front chamber the same as that of the outside. The hole for the rod of the pneumatic cylinder on the front cap is cut such that the size of the hole closely match the diameter of the rod. Thus the rod is held in position from any lateral movements. The front surface of the rod is filed to match the surface of the brass rod. In order to satisfy the rigidity requirement, the thickness of the fixture which holds the two pneumatic cylinders is above 5 mm and fillets are employed to decrease stress concentration. The 3D model of the pneumatic actuator of the lock device is shown in Fig. 6.2.

6.2.2 Material Selection and Fabrication

In order to ensure the MRI-compatibility, all the components of the device are made of non-metallic materials. Two identical acrylic rings are laser cut from a 6.35 mm acrylic sheet. Also the front cap is laser cut from the 6.35 mm acrylic sheet. The back cap and the two pistons are laser cut from a 3.15 mm acrylic sheet. A

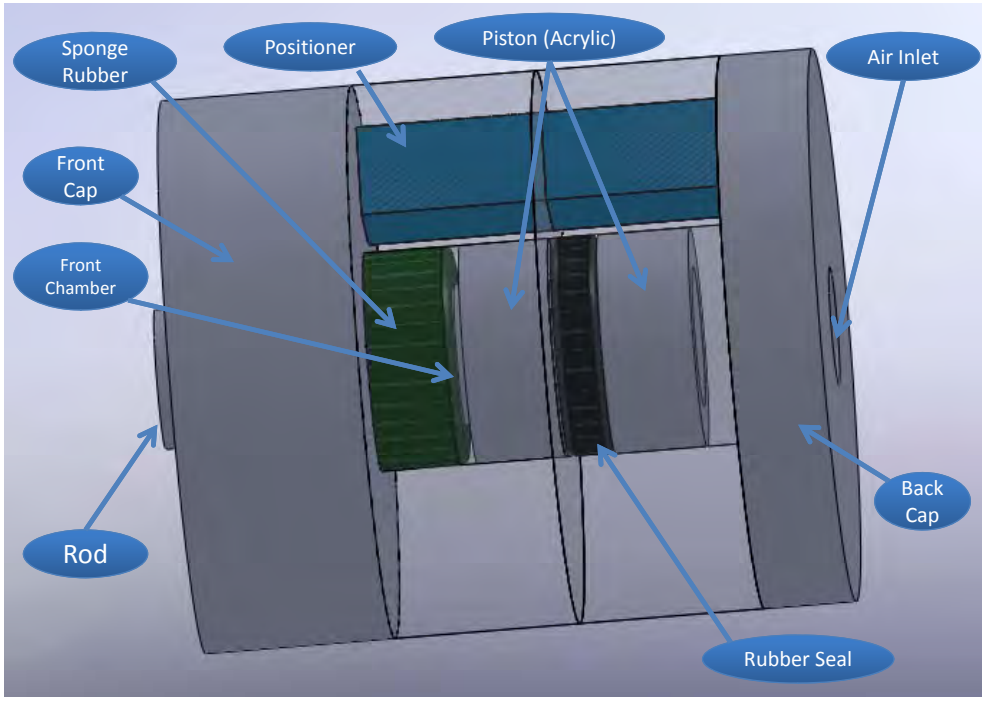

Figure 6.2: The mechanical structure of the pneumatic actuator of the lock device

rubber ring is selected as the sealing ring. The rod is hand cut from a ϕ4.8 mm acrylic rod. A sponge rubber ring is selected as the equivalent spring for excellent resilience, simplicity and low-cost and is laser cut from a 4.8 mm thick natural gum foam rubber sheet. The fixture to hold the two pneumatic cylinders is made of ABS and is fabricated via rapid prototyping machine.

6.2.3 Assembly

Firstly, the two acrylic rings are placed next to each other and the positioner is inserted into the positioning hole on the two ring to ensure they are concentric. Then

all three components are glued as the housing of the pneumatic cylinder. Next step is to glue the back cap to one side of the housing. Then the rod is inserted in one acrylic piston such that the two surfaces of the rod and the piston are aligned in the same plane. The rubber sealing ring is inserted next to the piston and then the other acrylic piston is inserted next to rubber ring. The two pistons are glued to fix the rubber ring in position. Then we can place the rod with piston inside the chamber. Next step is to insert the sponge rubber ring and the front cap to the rod. Then the sponge rubber ring is glued to the front cap. Now that the sponge rubber ring is fixed, the front cap can be glued to the housing. Two pneumatic cylinders are to be made in this way. Furthermore, we can glue the two actuators to the fixture. Finally, the lock device can be attached to the pneumatic cylinder by threaded into the front cap of the pneumatic cylinder.

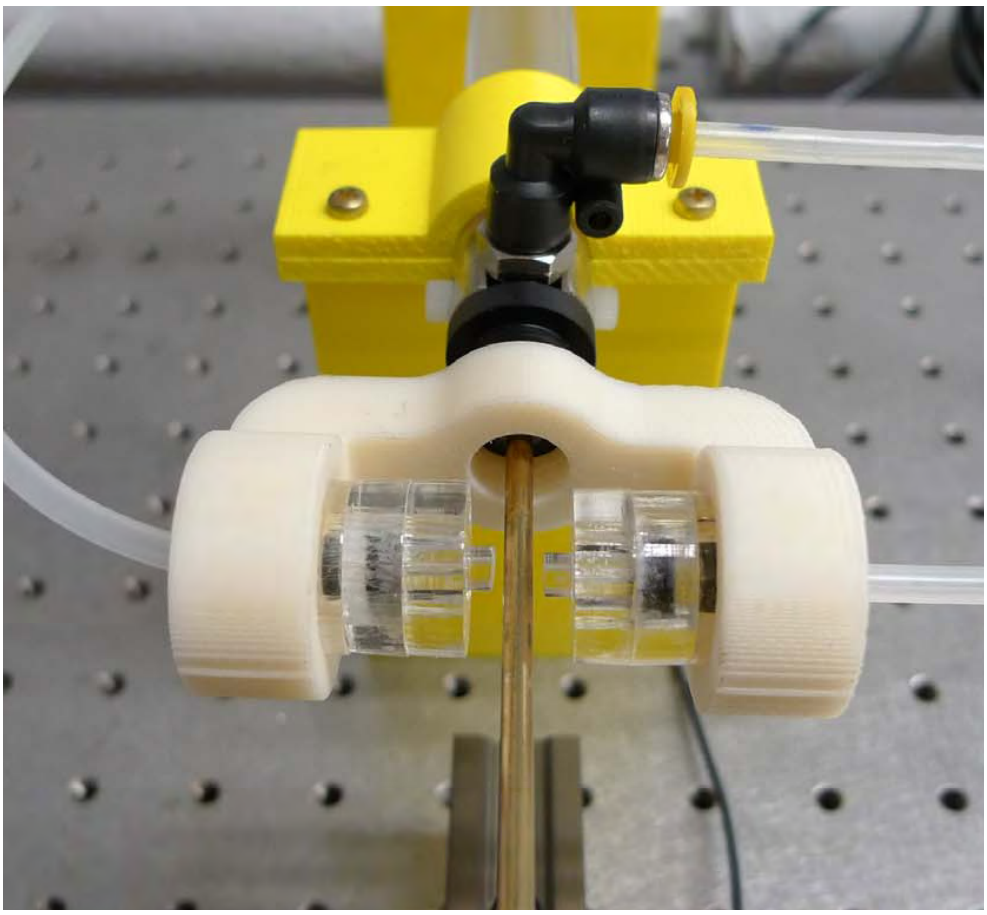

Figure 6.3: The lock device attached to the pneumatic cylinder

6.3 Test Result

Figure 6.3 shows the locked device integrated with the pneumatic cylinder. It was observed that the position of the brass rod stayed still the moment the two actuators of the lock device touched the brass rod and the external force did not move the brass rod once locked.

Chapter 7

CONCLUSION AND FUTURE WORK

7.1 Conclusion

This thesis presents the development of a MRI-compatible pneumatic actuation test system regulated by piezoelectric valve for image guided robotic intervention. The pneumatic actuation test system consists of PC, custom servo board driver, piezoelectric valves, sensors and pneumatic cylinder. This system was proposed to evaluate the pneumatic control algorithm performance in terms of accuracy, response time and robustness of external load uncertainty. The mathematical modeling of the pressure regulating valve with time delay and the pneumatic cylinder are presented. Three different sliding mode control (SMC) schemes are proposed to compare the system

performance. Simulation results are presented to evaluate the control algorithm and to tune the control scheme parameters. Practical tests show that the how that the system performance attained the goal. For safety concerns, a novel MRI-compatible locking device for the pneumatic cylinder was developed to fix the rod once it stops at the desired position.

Chapter 1 introduces some background on image-guided surgery, MRI-compatible interventional systems, MRI-compatible actuation techniques and literature review on pneumatic control techniques and sliding mode control techniques.

Chapter 2 provides the development of the pneumatic actuation test system. The goal of the system is introduced at first. Then the system architecture is presented with detail information on the mechanical and controller design, pneumatic cylinder, load components and air supply.

Chapter 3 presents the modeling of the pneumatic actuation test system. Background on some of the previous mathematic models are demonstrated. The complexity of the previous models is mainly induced by the indirect access to pressure of the cylinder chambers. Then a simpler model is introduced for the pneumatic actuation test system with the utilization of the piezoelectric pressure regulated valves. The modeling of the valves is presented with consideration of dead time.

Chapter 4 introduces the mathematical description of the three SMC control schemes. The tuning parameters of the three control schemes are presented as well. Also the Matlab simulation results of the three SMC control schemes employed on the

pneumatic actuation test system are represented. Two types of tracking functions, step function and sine wave function, are proposed for evaluation. The results are compared in several aspects, such as tracking position accuracy, response time and so on. Various loading condition is applied to compare the robustness of each schemes.

Chapter 5 demonstrates the physical test of the pneumatic cylinder with identical parameters as presented in Matlab simulations. Comparision of the test results are presented. The reason of the difference is discussed and possible explanation is proposed. The effect of each control parameter is discussed and a conclusion of control algorithm evaluation is presented.

Chapter 6 presents the development of the MRI-compatible pneumatic cylinder lock. The mechanical design and material selection is presented . Preliminary test shows that the lock achieves the design goal.

7.2 Future Work

One of the issues I encountered is the system modeling of frictions. The inhomogeneity of coulomb friction and static friction as well as time varying viscous friction coefficient bring forth challenges to accurate system performance simulations. One remedy would be changing the carriage to a more rigid one and re-fabricate the adaptor between the load cell and carriage plate. In this way, the alignment issue can be solved and hence increase the homogeneity of the friction.

Another problem is that the piezoelectric model is based on the instantaneous system state, suggesting a prior knowledge of the reference input function so as to ensure performance; this might not be very exact. The future goal is to rewrite the model in discrete time, requiring knowledge of only the past and present state.

While the static point-to-point issues are basically solved with less than 0.1 mm SSE, the SSE of dynamic trajectory tracking is still not satisfying. One possible solution is to tune up the system friction and the equivalent control signal. Also the accuracy around the top and the bottom of the sine wave motion should be increased by tuning down the switching band width.

The pneumatic cylinder will be employed on the MRI-compatible XYZ stage as the linear actuator and evaluate the actuation performance. Once the performance is satisfying, this MRI-compatible pneumatic cylinder could be utilized in many other applications under MRI environment. Currently costs of the "off-the-shelf" piezoelectric motors are rather high, close to 1000 dollars. On the other hand, the pneumatic

cylinder is a low-cost solution. It could be a major competitor to piezoelectric motor the controllability and robustness issues are solved with SMC.

References

[1] K. Cleary and T. M. Peters, "Image-guided interventions: Technology review and clinical applications," *Annual Review of Biomedical Engineering*, vol. 12, no. 1, pp. 119–142, 2010.

[2] V. Horsley and R. H. Clarke, "The structure and functions of the cerebellum examined by a new method," *Brain*, vol. 31, no. 1, pp. 45–124, 1908.

[3] T. Guo, K. W. Finnis, A. G. Parrent, and T. M. Peters, "Visualization and navigation system development and application for stereotactic deep-brain neurosurgeries," *Computer Aided Surgery*, vol. 11, no. 5, pp. 231–239, 2006.

[4] G. Cole, J. Pilitsis, and G. S. Fischer, "Design of a robotic system for mri-guided deep brain stimulation electrode placement," in *Proc. IEEE Int. Conf. Robotics and Automation ICRA '09*, pp. 4450–4456, 2009.

[5] Y. Wang, G. A. Cole, H. Su, J. G. Pilitsis, and G. S. Fischer, "Mri compatibility evaluation of a piezoelectric actuator system for a neural interventional robot,"

in *Proc. Annual Int. Conf. of the IEEE Engineering in Medicine and Biology Society EMBC 2009*, pp. 6072–6075, 2009.

[6] G. Cole, K. Harrington, H. Su, A. Camilo, J. Pilitsis, and G. Fischer, "Closed-Loop Actuated Surgical System Utilizing Real-Time In-Situ MRI Guidance," in *12th International Symposium on Experimental Robotics - ISER 2010*, New Delhi and Agra, India, Dec 2010.

[7] H. A. Paul, W. L. Bargar, B. Mittlestadt, B. Musits, R. H. Taylor, P. Kazanzides, J. Zuhars, B. Williamson, and W. Hanson, "Development of a surgical robot for cementless total hip arthroplasty." *Clin Orthop Relat Res*, no. 285, pp. 57–66, Dec 1992.

[8] C. Rickers, M. Jerosch-Herold, X. Hu, N. Murthy, X. Wang, H. Kong, R. T. Seethamraju, J. Weil, and N. M. Wilke, "Magnetic resonance image-guided transcatheter closure of atrial septal defects." *Circulation*, vol. 107, no. 1, pp. 132–138, Jan 2003.

[9] S. Xu, G. Fichtinger, R. H. Taylor, and K. R. Cleary, "3d motion tracking of pulmonary lesions using ct fluoroscopy images for robotically assisted lung biopsy," *Medical Imaging 2004: Visualization, Image-Guided Procedures, and Display*, vol. 5367, no. 1, pp. 394–402, 2004.

[10] G. S. Fischer, I. Iordachita, C. Csoma, J. Tokuda, P. W. Mewes, C. M. Tempany, N. Hata, and G. Fichtinger, "Pneumatically operated mri-compatible needle

placement robot for prostate interventions," in *Proc. IEEE Int. Conf. Robotics and Automation ICRA 2008*, pp. 2489–2495, 2008.

[11] F. A. Jolesz, "Interventional and intraoperative mri: a general overview of the field." *J Magn Reson Imaging*, vol. 8, no. 1, pp. 3–7, 1998.

[12] H. Elhawary, Z. T. H. Tse, A. Hamed, M. Rea, B. L. Davies, and M. U. Lamperth, "The case for mr-compatible robotics: a review of the state of the art." *Int J Med Robot*, vol. 4, no. 2, pp. 105–113, Jun 2008.

[13] N. Yu and R. Riener, "Review on mr-compatible robotic systems," in *Proc. First IEEE/RAS-EMBS Int. Conf. Biomedical Robotics and Biomechatronics BioRob 2006*, pp. 661–665, 2006.

[14] K. Masamune, E. Kobayashi, Y. Masutani, M. Suzuki, T. Dohi, H. Iseki, and K. Takakura, "Development of an mri-compatible needle insertion manipulator for stereotactic neurosurgery." *J Image Guid Surg*, vol. 1, no. 4, pp. 242–248, 1995.

[15] R. W. Briggs, I. Dy-Liacco, M. P. Malcolm, H. Lee, K. K. Peck, K. S. Gopinath, N. C. Himes, D. A. Soltysik, P. Browne, and R. Tran-Son-Tay, "A pneumatic vibrotactile stimulation device for fmri." *Magn Reson Med*, vol. 51, no. 3, pp. 640–643, Mar 2004.

[16] K. Chinzei, N. Hata, F. A. Jolesz, and R. Kikinis, "Surgical assist robot for the

active navigation in the intraoperative mri: hardware design issues," in *Proc. IEEE/RSJ Int. Conf. Intelligent Robots and Systems (IROS 2000)*, vol. 1, pp. 727–732, 2000.

[17] B. T. Larson, A. G. Erdman, N. V. Tsekos, E. Yacoub, P. V. Tsekos, and I. G. Koutlas, "Design of an mri-compatible robotic stereotactic device for minimally invasive interventions in the breast." *J Biomech Eng*, vol. 126, no. 4, pp. 458–465, Aug 2004.

[18] A. Khanicheh, D. Mintzopoulos, B. Weinberg, A. A. Tzika, and C. Mavroidis, "Mr-chirod v.2: A fmri compatible mechatronic hand rehabilitation device," in *Proc. IEEE 10th Int. Conf. Rehabilitation Robotics ICORR 2007*, pp. 883–889, 2007.

[19] N. V. Tsekos, A. Ozcan, and E. Christoforou, "A prototype manipulator for magnetic resonance-guided interventions inside standard cylindrical magnetic resonance imaging scanners." *J Biomech Eng*, vol. 127, no. 6, pp. 972–980, Nov 2005.

[20] G. S. Fischer, I. Iordachita, C. Csoma, J. Tokuda, S. P. DiMaio, C. M. Tempany, N. Hata, and G. Fichtinger, "Mri-compatible pneumatic robot for transperineal prostate needle placement," vol. 13, no. 3, pp. 295–305, 2008.

[21] H. Su and G. Fischer, "A 3-axis optical force/torque sensor for prostate needle placement in magnetic resonance imaging environments," in *2nd Annual*

IEEE International Conference on Technologies for Practical Robot Applications. Boston, MA, USA: IEEE, 2009.

[22] H. Su, W. Shang, G. Cole, K. Harrington, and F. S. Gregory, "Haptic System Design for MRI-Guided Needle Based Prostate Brachytherapy," in *IEEE Haptics Symposium 2010*. Boston, MA, USA: IEEE, 2010.

[23] H. Su, H. Huang, and J. Mills, "Force Sensing and Control of Robot-Assisted Cell Injection," in *Advances in Robotics and Virtual Reality*, T. Gulrez and A. Hassanien, Eds. Springer-Verlag, 2011.

[24] H. Su, G. Cole, C. Tempany, N. Hata, and G. Fischer, "High-field MRI Compatible Steerable Needle Driver Robot for Percutaneous Prostate Intervention," in *Proceedings of MMVR18 (Medicine Meets Virtual Reality)*, Newport Beach, California, USA, February 2011.

[25] H. Su, G. Cole, and G. Fischer, "Active Needle Steering for Percutaneous Prostate Intervention in High-field MRI," in *2010 Robotics: Science and Systems Conference, Workshop on Enabling Technologies for Image-Guided Robotic Interventional Procedures*, Zaragoza, Spain, Aug 2010.

[26] H. Su, M. Zervas, G. Cole, C. Furlong, and G. Fischer, "Real-time mri-guided needle placement robot with integrated fiber optic force sensing," *IEEE ICRA 2011 International Conference on Robotics and Automation*, 2011.

[27] A. Krieger, R. C. Susil, C. Menard, J. A. Coleman, G. Fichtinger, E. Atalar, and L. L. Whitcomb, "Design of a novel mri compatible manipulator for image guided prostate interventions," vol. 52, no. 2, pp. 306–313, 2005.

[28] A.-C. Zappe, T. Maucher, K. Meier, and C. Scheiber, "Evaluation of a pneumatically driven tactile stimulator device for vision substitution during fmri studies." *Magn Reson Med*, vol. 51, no. 4, pp. 828–834, Apr 2004.

[29] R. Moser, R. Gassert, E. Burdet, L. Sache, H. R. Woodtli, J. Erni, W. Maeder, and H. Bleuler, "An mr compatible robot technology," in *Proc. IEEE Int. Conf. Robotics and Automation ICRA '03*, vol. 1, pp. 670–675, 2003.

[30] E. Hempel, H. Fischer, L. Gumb, T. Hhn, H. Krause, U. Voges, H. Breitwieser, B. Gutmann, J. Durke, M. Bock, and A. Melzer, "An mri-compatible surgical robot for precise radiological interventions." *Comput Aided Surg*, vol. 8, no. 4, pp. 180–191, 2003.

[31] M. Flueckiger, M. Bullo, D. Chapuis, R. Gassert, and Y. Perriard, "fmri compatible haptic interface actuated with traveling wave ultrasonic motor," in *Proc. Fourtieth IAS Annual Meeting Industry Applications Conf. Conf. Record of the 2005*, vol. 3, pp. 2075–2082, 2005.

[32] A. Khanicheh, A. Muto, C. Triantafyllou, B. Weinberg, L. Astrakas, A. Tzika, and C. Mavroidis, "Mr compatible erf driven hand rehabilitation device," in *Proc. 9th Int. Conf. Rehabilitation Robotics ICORR 2005*, pp. 7–12, 2005.

[33] J. Vogan, A. Wingert, J.-S. Plante, S. Dubowsky, M. Hafez, D. Kacher, and F. Jolesz, "Manipulation in mri devices using electrostrictive polymer actuators: with an application to reconfigurable imaging coils," in *Proc. IEEE Int. Conf. Robotics and Automation ICRA '04*, vol. 3, pp. 2498–2504, 2004.

[34] G. S. Fischer, A. Krieger, I. Iordachita, C. Csoma, L. L. Whitcomb, and F. Gabor, "Mri compatibility of robot actuation techniques–a comparative study." *Med Image Comput Comput Assist Interv*, vol. 11, no. Pt 2, pp. 509–517, 2008.

[35] Y. Wang, M. Shazeeb, C. Sotak, and S. G. Fischer, "Optimization of piezoelectric motors to enhance mr compatiblity for interventional devices," in *17th Scientific Meeting and Exhibition of the International Society of Magnetic Resonance in Medicine*, 2009.

[36] F. Carpi, A. Khanicheh, C. Mavroidis, and D. De Rossi, "Mri compatibility of silicone-made contractile dielectric elastomer actuators," in *Mechatronics, IEEE/ASME Transactions on*, vol. 13, no. 3, pp. 370–374–, 2008.

[37] S. K. Charles, H. I. Krebs, B. T. Volpe, D. Lynch, and N. Hogan, "Wrist rehabilitation following stroke: initial clinical results," in *Proc. 9th Int. Conf. Rehabilitation Robotics ICORR 2005*, pp. 13–16, 2005.

[38] D. Stoianovici, A. Patriciu, D. Petrisor, D. Mazilu, and L. Kavoussi, "A new type of motor: pneumatic step motor," in *IEEE/ASME Transactions on Mechatronics*, vol. 12, no. 1, pp. 98–106–, 2007.

[39] A. Melzer, B. Gutmann, T. Remmele, R. Wolf, A. Lukoscheck, M. Bock, H. Bardenheuer, and H. Fischer, "Innomotion for percutaneous image-guided interventions," vol. 27, no. 3, pp. 66–73, 2008.

[40] J. E. Bobrow and F. Jabbari, "Adaptive pneumatic force actuation and position control," *Journal of Dynamic Systems, Measurement, and Control*, vol. 113, no. 2, pp. 267–272, 1991.

[41] B. W. McDonell and J. E. Bobrow, "Adaptive tracking control of an air powered robot actuator," *Journal of Dynamic Systems, Measurement, and Control*, vol. 115, no. 3, pp. 427–433, 1993.

[42] M.-C. Shih and M.-A. Ma, "Position control of a pneumatic cylinder using fuzzy pwm control method," *Mechatronics*, vol. 8, no. 3, pp. 241 – 253, 1998.

[43] S. Chillari, S. Guccione, and G. Muscato, "An experimental comparison between several pneumatic position control methods," in *Proc. 40th IEEE Conf. Decision and Control*, vol. 2, pp. 1168–1173, 2001.

[44] A. K. Paul, J. E. Mishra, and M. G. Radke, "Reduced order sliding mode control for pneumatic actuator," vol. 2, no. 3, pp. 271–276, 1994.

[45] J. Pu and R. H. Weston, "A new generation of pneumatic servos for industrial robots," *Robotica*, vol. 7, no. 01, pp. 17–24, 1989.

[46] A. Messina, N. I. Giannoccaro, and A. Gentile, "Experimenting and modelling

the dynamics of pneumatic actuators controlled by the pulse width modulation (pwm) technique," *Mechatronics*, vol. 15, no. 7, pp. 859–881, Sep. 2005.

[47] A. K. Paul, J. K. Mishra, and M. G. Radke, "Reduced order sliding mode control for pneumatic actuator," in *IEEE Transactions on Control Systems Technology*, vol. 2, no. Compendex, pp. 271–276–, 1994.

[48] T. Acarman, C. Hatipoglu, and U. Ozguner, "A robust nonlinear controller design for a pneumatic actuator," in *American Control Conference, 2001. Proceedings of the 2001*, vol. 6, pp. 4490–4495 vol.6–, 2001.

[49] P. Korondi and J. Gyeviki, "Robust position control for a pneumatic cylinder," in *Power Electronics and Motion Control Conference, 2006. EPE-PEMC 2006. 12th International*, pp. 513–518–, 2006.

[50] A. J. Koshkouei, K. J. Burnham, and A. S. I. Zinober, "Dynamic sliding mode control design," in *Control Theory and Applications, IEE Proceedings* -, vol. 152, no. 4, pp. 392–396–, 2005.

[51] T. Nguyen, J. Leavitt, F. Jabbari, and J. E. Bobrow, "Accurate sliding-mode control of pneumatic systems using low-cost solenoid valves," in *Mechatronics, IEEE/ASME Transactions on*, vol. 12, no. 2, pp. 216–219–, 2007.

[52] N. Shu and G. M. Bone, "Experimental comparison of two pneumatic servo

position control algorithms," in *Mechatronics and Automation, 2005 IEEE International Conference*, vol. 1, pp. 37–42 Vol. 1–, 2005.

[53] G. M. Bone and N. Shu, "Experimental comparison of position tracking control algorithms for pneumatic cylinder actuators," in *Mechatronics, IEEE/ASME Transactions on*, vol. 12, no. 5, pp. 557–561–, 2007.

[54] Q. Xu and Y. Li, "Global sliding mode-based tracking control of a piezo-driven xy micropositioning stage with unmodeled hysteresis," in *Intelligent Robots and Systems, 2009. IROS 2009. IEEE/RSJ International Conference on*, pp. 755–760–, 2009.

[55] N. Gulati and E. J. Barth, "A globally stable, load-independent pressure observer for the servo control of pneumatic actuators," in *Mechatronics, IEEE/ASME Transactions on*, vol. 14, no. 3, pp. 295–306–, 2009.

[56] O. Camacho and C. A. Smith, "Sliding mode control: an approach to regulate nonlinear chemical processes," in *ISA Transactions*, vol. 39, no. 2, pp. 205–218–, 2000.

[57] J. T. Hing, A. D. Brooks, and J. P. Desai, "Reality-based needle insertion simulation for haptic feedback in prostate brachytherapy," in *Proc. IEEE Int. Conf. Robotics and Automation ICRA 2006*, pp. 619–624, 2006.

[58] G. Fischer, "Enabling technologies for mri guided interventional procedures," Ph.D. dissertation, Johns Hopkins University, Baltimore, 2008.

[59] J. Wang, D. J. D. Wang, P. R. Moore, and J. Pu, "Modelling study, analysis and robust servo control of pneumatic cylinder actuator systems," *IEE Proceedings -Control Theory and Applications*, vol. 148, no. 1, pp. 35–42, 2001.

[60] E. Richer and Y. Hurmuzlu, "A high performance pneumatic force actuator system: Part i—nonlinear mathematical model," *Journal of Dynamic Systems, Measurement, and Control*, vol. 122, no. 3, pp. 416–425, 2000.

[61] J. M. Tressler, T. Clement, H. Kazerooni, and A. Lim, "Dynamic behavior of pneumatic systems for lower extremity extenders," in *Proc. IEEE Int. Conf. Robotics and Automation ICRA '02*, vol. 3, pp. 3248–3253, 2002.

[62] Y.-C. Tsai and A.-C. Huang, "Multiple-surface sliding controller design for pneumatic servo systems," *Mechatronics*, vol. 18, no. 9, pp. 506 – 512, 2008.

[63] J. Kun, Z. Jinggang, and C. Zhimei, "A new approach for the sliding mode control based on fuzzy reaching law," in *Intelligent Control and Automation, 2002. Proceedings of the 4th World Congress on*, vol. 1, pp. 656–660 vol.1–, 2002.

Vita

Yi Wang was born on Nov. 17, 1985 in Huabei Oilfield, Hebei, China. He received the B.E. degree in Mechanical Engineering from Harbin Institute of Technology in 2008, and enrolled in the Mechanical Engineering graduate program at Worcester Polytechnic Institute (WPI) in 2008. Since 2008, he has been a graduate research assistant with Automation and Interventional Medicine (AIM) Robotics Research Laboratory in WPI. His research interests focus on development of MRI-compatible robotic systems, robotic mechanism design, MRI-compatible actuation techniques, pneumatic control techniques, and design of smart material actuator.